AN EXPERIMENTAL STUDY ON THE DYNAMICS OF WAVE BLOCKING AND BREAKING ON OPPOSING CURRENTS

by

ARUN CHAWLA
AND
JAMES T. KIRBY

THIS RESEARCH WAS SUPPORTED BY NOAA,
OFFICE OF SEA GRANT, DEPARTMENT OF COMMERCE,
GRANT NO. NA56RG0147

RESEARCH REPORT NO. CACR-00-02
MARCH, 2000

CENTER FOR APPLIED COASTAL RESEARCH
OCEAN ENGINEERING LABORATORY
UNIVERSITY OF DELAWARE
NEWARK, DE 19716

TABLE OF CONTENTS

Chapter

LIST OF FIGURES

LIST OF TABLES

ABSTRACT

A detailed experimental study has been carried out in a laboratory to study the strong wave-current interactions that are observed at the mouth of river inlets. The aim of this work was twofold. Firstly, to study the dynamics of wave blocking under different wave climates and, secondly, to develop empirical formulae that quantify energy dissipation due to current-limited wave breaking. These formulae can then be used in numerical models simulating wave-current interactions.

The experiments were conducted in a 30 m long recirculating flume. A channel with a varying width was placed in the middle part of the flume to simulate an inlet. The experiments were designed such that wave blocking occurred close to the narrow part of the channel where the currents were maximum. All the experiments were conducted in a constant water depth of 0.5 m. The experiments were broadly divided into 3 parts: the monochromatic wave tests, the narrow-banded spectral tests, and the random wave tests.

The monochromatic tests were further subdivided into two subgroups : the wave reflection tests and the wave breaking tests. The wave reflection tests were small amplitude tests in which the waves were reflected from the blocking point with very little breaking. The measured amplitude envelope for the smallest amplitudes was an Airy function and confirmed the linear theory predictions. In the breaking wave tests there was very little to no reflection and all the blocking was accompanied by wave breaking. The blocking phenomenon was found to depend strongly on non-linearity. An empirical dissipation formula based on a modified bore model approach was developed and tested with the data.

The narrow-banded spectral tests were also divided into two subgroups : the wave group tests and the wave packet tests. The aim was to see if a moving blocking point could generate long waves upstream of the blocking region. In the wave group tests, the individual components of the spectra were blocked separately at their respective blocking points. No long wave motion was observed in any of the tests.

A weakly non-linear narrow-banded amplitude envelope numerical model has been developed for a varying channel. The model accounts for wave blocking by allowing the phase to be complex. The model uses a linear dispersion relation. Comparisons with data show that though the model can handle wave blocking, it is unable to predict the correct blocking position as that depends strongly on amplitude dispersion effects. Also, the model blocks the waves at the carrier frequency of the modulating wave train, whereas observations have shown that the actual blocking occurs at the separate blocking points of the respective spectral components.

Finally, random wave tests were also conducted to compliment the monochromatic wave tests. The random wave tests consisted of TMA spectra of varying energy and peak frequency. The tests varied from most of the spectrum getting blocked, to very little blocking. Using an empirical probability of breaking based on the data, a bulk dissipation formula for energy loss due to current-limited breaking in random waves has been proposed and tested with the data using both a bulk wave action conservation model and a spectral model. The energy dissipation formula is based on a wave slope formulation, and other formulae based on a wave slope formulation also compared well with the data.

Chapter 1

INTRODUCTION

Wave-current interactions occur in nature over a varying set of physical scales starting from the development of large freak waves on the Agulhas current that severely damaged an oil tanker (Mallory, 1974) down to the small scale interactions between capillary waves and internal waves. These interactions are also not just limited to the modification of waves by underlying currents and a good example of the development of currents by waves is the generation of rip currents and long shore currents by waves breaking on a beach. Thus, the study of wave-current interactions has been a topic of active research among scientists for quite some time now and a good overall picture of the different aspects of this interaction can be found in the review papers by Peregrine (1976), Jonsson (1990) and Thomas and Klopman (1997).

A particular area of interest in this subject is the interaction between short scale gravity waves and strong large scale tidal currents. In these cases the time and length scales over which the current varies is much larger than the wave period or wave length. Similar to the case of waves in slowly varying depth, the waves are assumed to locally satisfy the kinematic properties of plane waves on uniform currents. Consider a two-dimensional wave moving on a depth uniform current $\mathbf{U}$ (see Figure 1.1). Then in a frame of reference moving with the component of the current in the direction of the waves, the equations and solutions for water wave motion are identical to the case of no current. If ω is the wave frequency in a

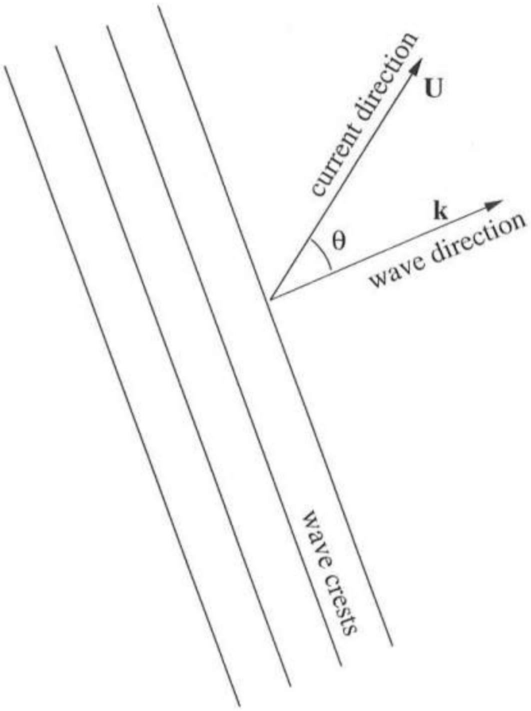

Figure 1.1: Schematic diagram showing the wave and current direction

stationary reference frame and σ is the wave frequency in a reference frame moving with the current, then the phase speed of the wave in the two reference frames can be related by

$$\frac{\omega}{|\mathbf{k}|} = \frac{\sigma}{|\mathbf{k}|} + |\mathbf{U}| \cos\theta$$

or

$$\omega - \mathbf{k} \cdot \mathbf{U} = \sigma \tag{1.1}$$

where **k** is the wave number and remains unchanged in the two reference frames. The expression for σ depends on the wave theory used. Eqn. (1.1), together with an expression for σ gives the Doppler-shifted dispersion relation for waves moving on uniform currents.

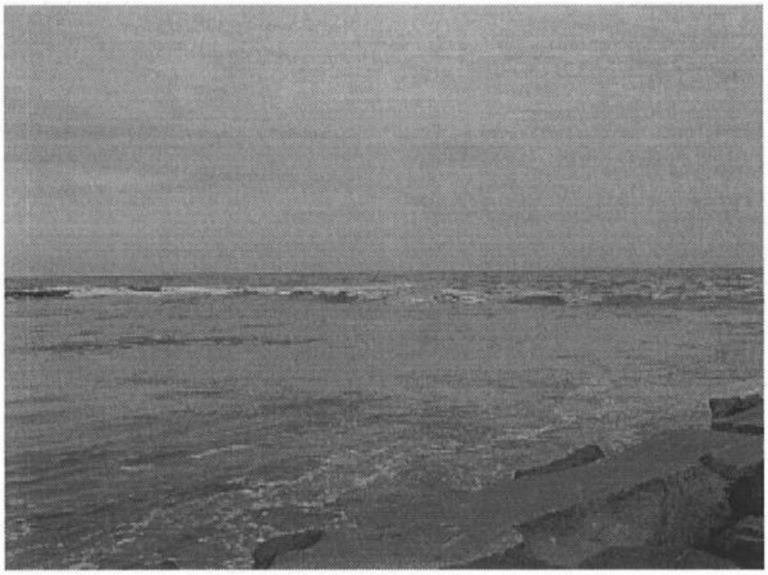

Figure 1.2: Wave Blocking at Indian River Inlet, Delaware USA

1.1 Kinematics of wave blocking

Wave blocking is the phenomenon by which propagating waves are stopped by strong opposing currents. As waves propagate into an opposing current, their group velocity $(\frac{\partial \omega}{\partial k})$ reduces, leading to the waves shoaling on the current. If the current is strong enough then this group velocity could go to zero causing the waves to get blocked. This is fairly common at the entrances of tidal inlets where tidal currents can become very strong. One such example of wave blocking is shown in Figure 1.2, where the view is looking seaward from the southern inlet breakwater. The photograph has been taken three hours after high tide, and thus there is a strong current propagating out of the inlet. This strong current blocks waves that are trying to propagate into the inlet. Due to the sharp increase in wave steepness prior to blocking, the wave environment tends to become very rough, as can be seen in Figure 1.3. This causes a considerable navigational hazard, and boats have been known to capsize trying to transit or navigate inlets under such circumstances.

Figure 1.3: Wave field close to the blocking point

For waves to get blocked their group velocity has to go to zero. Thus, differentiating the dispersion relation (1.1) with respect to k and setting the group velocity to zero we get

$$\frac{\partial \sigma}{\partial k} = -U \tag{1.2}$$

where

$$U \equiv |\mathbf{U}| \cos \theta$$

Eqn. (1.2) is the kinematic condition that has to be satisfied for waves to get blocked. From the equation it is obvious that wave blocking can only occur if the currents are opposing the waves ($\theta > 90°$).

A better understanding of the blocking process can be obtained from the graphical solution of (1.1) using linear wave theory.

$$\sigma = \sqrt{gk \tanh kh}$$

The dispersion solution is given by the intersection of the curve $\sigma = \omega - kU$ with the curve $\sigma = \sqrt{gk \tanh kh}$ in Figure 1.4. We shall limit our analysis to a 1-dimensional flow field in which the current is moving opposite to the waves ($\theta = 180°$). The solution point **A** corresponds to a wave moving in the absence of a current. In the presence of an opposing current the solution moves to point **B** which corresponds to a wave with a larger wave number k (shorter wave length). The group velocity of the wave is given by the difference of the slope of the curve and the straight line. As the wave propagates into regions of stronger current, the wave number keeps increasing and the group velocity decreases till at point **D** the group velocity goes to zero. This corresponds to the blocking point, and no solution for the wave exists for stronger currents. For any arbitrary current smaller than the blocking current there is also a second solution given by point **C**, which has no corresponding solution in still water. The waves corresponding to this solution have very short wave lengths and their group velocity is negative. Thus, even though the waves are moving against the current their energy is washed down by the current. As the waves are pushed further and further into weaker currents, their wave lengths keep decreasing. At the blocking point the two solutions **B** and **C** coalesce to give a single solution at **D**.

From Figure 1.4 it is also clear that if ω decreases then the slope of the straight line at **D** becomes greater. Thus, longer waves require stronger blocking currents. To study the effects of the wave amplitude on the blocking point consider a 3^{rd} order Stokes theory in deep water

$$\sigma = \sqrt{gk\left[1 + (ka)^2\right]}$$

which leads to

$$\frac{\partial \sigma}{\partial k} = \sqrt{\frac{g}{k}}\left[\frac{1 + 3(ka)^2}{\sqrt{1 + (ka)^2}}\right] \tag{1.3}$$

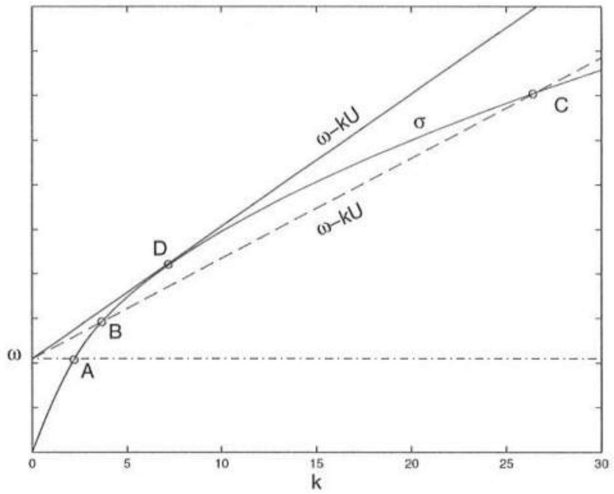

Figure 1.4: Graphical solution of the dispersion relation ('Dash Dot line' U = 0; 'Dash line' U < blocking current; 'Solid line' U = blocking current)

From (1.3) and (1.2) we see that larger waves require a stronger blocking current. A graphical comparison of the linear dispersion relation with the Stokes dispersion relation is shown in Figure 1.5. The linear and non-linear blocking points are denoted by **D** and $\mathbf{D_n}$ respectively. The required blocking current is given by the slope of the straight line, which is greater for the non-linear case.

Wave-current interactions can significantly alter the wave lengths and ignoring this effect can lead to considerable errors. One such case has been highlighted by Jonsson *et al.* (1970), who have quantified the errors in surface wave calculations from bottom mounted pressure measurements.

1.2 Dynamics of wave blocking

The blocking effect of strong opposing currents have been known for a long time. Evans (1955) conducted experimental studies on hydraulic breakwaters for stopping waves. However the dynamics of wave-current interaction became much clearer with the development of the concept of radiation stress by Longuet-Higgins

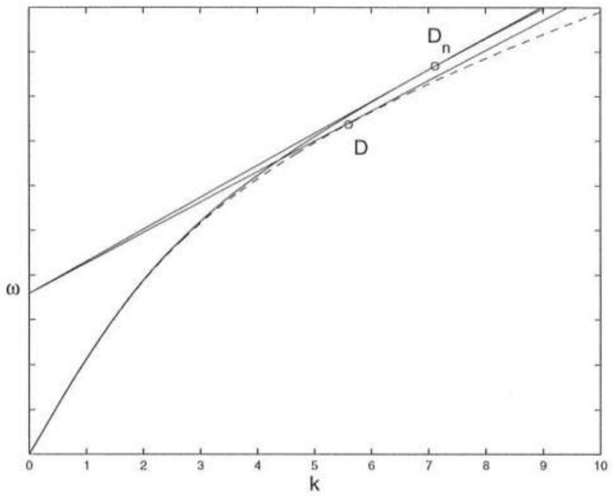

Figure 1.5: Graphical representation of wave blocking using linear dispersion relation ('Dashed' line) and Stokes dispersion relation ('Solid line'); T = 1.75 s, h = 0.50 m, a = 0.04 m. $\mathbf{D}$ and $\mathbf{D_n}$ correspond to the linear and non-linear blocking points respectively.

and Stewart(1960,1961). By averaging over the oscillatory wave motion they showed that radiation stress, which is defined as the excess momentum flux due to waves, is responsible for the transfer of energy between waves and currents in the energy equation. The governing equation in one dimension for a depth uniform current is given by

$$\frac{\partial E}{\partial t} + \frac{\partial}{\partial x}\Big(c_g E\Big) + S_{xx}\frac{\partial U}{\partial x} = 0 \tag{1.4}$$

where E is the wave energy and can be written in terms of the wave amplitude a

$$E \equiv \frac{1}{2}\rho g a^2$$

S_{xx} is the radiation stress and, using linear wave theory, can be written as

$$S_{xx} = \rho \int_{-h}^{0} \overline{u^2} dz + \int_{-h}^{0} \overline{p} dz$$

u and p are the horizontal velocity and pressure distributions due to the wave motion.

Alternatively, using the concept of averaged Lagrangian (Whitham, 1965), Bretherton and Garrett (1969) showed that in a moving medium it is the wave action that is conserved and not the wave energy. The wave action is defined as the ratio of the wave energy density E and the intrinsic frequency σ, and the governing equation is given by

$$\frac{\partial}{\partial t}\left(\frac{E}{\sigma}\right) + \frac{\partial}{\partial x}\left(\frac{c_g E}{\sigma}\right) = 0 \tag{1.5}$$

They also showed that for surface gravity waves (1.4) and (1.5) are the same equation.

Considering steady wave motion, eqn. (1.5) predicts that waves shoal as they propagate into regions of stronger currents and at the blocking point the energy goes to infinity. For this reason it was believed that waves break before they reach the blocking point (e.g. Phillips, 1966). However, the difficulty with using either the radiation stress theory or the wave action conservation principle close to the blocking region is that they are based on ray theory, which lead to singularities at caustics such as the blocking point.

Using a perturbation stream function and conducting a local analysis in the neighborhood of the blocking point, Peregrine (1976) showed that the waves at the blocking point have a large but finite steepness and are not singular. If the initial steepness is small enough that there is no wave breaking anywhere in the domain then the waves are reflected at the blocking point with a different wave number and the amplitude envelope through the blocking region is given by an Airy function. The reflected wave is denoted by point **C** in Figure 1.4, and as these waves are swept back into weaker currents they continue to increase in steepness. Smith (1975), using the uniform expansion of Ludwig (1966), developed a uniform asymptotic solution for the wave amplitude through the blocking region. He showed that the wave action flux for the incident and reflected wave are equal and opposite. Between the regions of no blocking to complete reflection due to blocking there lies a transition region when the current is strong enough only to cause partial wave reflection. A linear analysis of partial wave reflection with the help of Schrödinger equations was carried out by Stiassnie and Dagan (1979). The results of complete transmission and complete reflection were recovered as limiting cases of their more general approach.

Recently, Shyu and Phillips (1990) extended the work of Smith (1975) to include capillary effects and blocking on finite amplitude long waves. As reflected waves become smaller capillary effects become more important. The inclusion of capillary effects leads to the identification of a second reflection point where the reflected waves are reflected once again back in the direction of the incident waves. The second reflection is accompanied by a further increase in the wave number, beyond which viscous dissipation effects become important and the wave motion is damped out. The physics of this multiple reflection have been outlined in Trulsen and Mei (1993). If the two blocking points are sufficiently far apart then the theory of Shyu and Phillips (1990) can be used to analyze the multiple reflection. Trulsen and Mei (1993), using a boundary layer method, developed an alternative theory for the multiple reflections without any limit on the separation distance between the two reflection points and extended the work to the limit when the two reflection points coalesce. The phenomenon of double reflection and corresponding attenuation of wave amplitude due to viscous effects have been observed in the short wave experiments of Badulin *et al.* (1983).

In recent years direct modeling of wave blocking has been done with the help of fully non-linear Boussinesq models (Chen *et al.*, 1998). The advantage of using Boussinesq models is that they are non-linear and can be used to study amplitude dispersion and energy transfer effects in the dynamics of wave blocking. The disadvantage is that for short waves the dispersive properties are not very well predicted, with the deviation increasing with increasing wave number. If wave blocking occurs before the waves become short enough for these deviations to be prominent then the models work very well (Chen *et al.*, 1998). But if wave blocking is expected to occur in the region where the waves are very short then the deviations in the dispersion relation will lead to significant errors in the predictions of wave blocking.

1.3 Motivation for current study

Most of the theoretical analysis on wave blocking has been limited to the linear wave limit. But the sharp steepening of waves just prior to the blocking point makes this approximation valid only for very small waves, which is not the case at river inlet entrances where the waves are steep and tend to break at or before the blocking point (see Figure 1.3). Due to the complexity of the wave field, an experimental study is required to shed light on the dynamics of wave blocking and steepness limited wave breaking. Unfortunately there are very few experimental studies on this subject. Lai *et al.* (1989) conducted experimental studies with both monochromatic and random waves on strong opposing currents. They studied the kinematics of the strong interaction up to the blocking point but did not show any results about the dynamics of the interaction. Sakai and Saeki (1984) conducted wave breaking tests for monochromatic waves in the presence of both a sloping bottom and an opposing current, and the corresponding studies for irregular waves were conducted by Sakai *et al.* (1986). There is however still very limited understanding of how the wave energy is dissipated due to current limited breaking. Ris and Holthuijsen (1996) simulated current-induced breaking and blocking with the help of a third-generation wind-wave spectral model, and compared their results with the data of Lai *et al.* (1989). The dynamics of the process were poorly predeicted.

To develop a better understanding of the dynamics involved in the interactions between waves and strong currents, a series of experiments have been conducted in the recirculating flume at the Center for Applied Coastal Research. The main objectives were:

1. To study the amplitude envelope of monochromatic waves through the blocking region for varying conditions from transmission to complete reflection when there is no wave breaking.
2. To study the evolution of large monochromatic waves through the blocking region in the presence of wave breaking.
3. To study the effects of a moving blocking point by conducting tests on wave groups and wave packets.
4. To develop empirical formulae that quantify energy dissipation due to current limited wave breaking in deep water, for both monochromatic and random waves. These formulae can then be used with numerical models of Ris and Holthuijsen (1996) and Chen *et al.* (1998) to study the dynamics of strong wave-current interactions (e.g. waves breaking on rip currents).

1.4 Thesis outline

The thesis outline is as follows.

In Chapter 2, the experimental facility has been described. First the experimental setup is explained in detail with the help of a schematic diagram of the plan view. Then there is an explaination of the coordinate system and the measuring instruments used for collecting data. Finally, a detailed description of the generated current profile has been given.

In Chapter 3, details about the monochromatic experiments and corresponding analysis are given. The experiments are in two parts. The first part consisting of very small amplitude tests where the waves are reflected from the blocking point with very little to no breaking. Comparisons of the measured wave envelope are made with linear theory. In the second part large amplitude tests are considered where the waves break without being reflected at the blocking point. An energy dissipation formula is developed to simulate current limited wave breaking and comparisons are made to the data with the help of a simple model based on the wave action conservation principle. A heirarchial pattern is observed in waves on blocking currents. Predictions of the blocking point are made with both the linear and non-linear dispersion relation and checked with the data.

In Chapter 4, details about the experimental studies on narrow banded spectra are given. Experiments were conducted with wave groups (generated by a bichromatic spectrum) and wave packets (generated by a Gaussian spectrum).

In Chapter 5, a third order weakly non-linear model is developed for the envelope of narrow-banded waves propagating against strong varying currents. The model is width integrated to account for a varying channel. The phase is complex so that the waves decay beyond the blocking point. The model uses a second order iterative finite difference scheme. A breaking model based on the empirical dissipation function developed in Chapter 3 is used. The numerical model is compared with the experimental observations presented in Chapters 3 and 4.

In Chapter 6, experimental studies on random waves are presented. Based on the experimental data a bulk dissipation model is developed to simulate energy dissipation due to current limited wave breaking. The breaking model is tested using two separate numerical models both of which are width integrated and based on the wave action conservation principle. The empirical dissipation model is based on a slope formulation and comparisons are made with existing models that are also based on a wave slope formulation. The parametric values used to calibrate the dissipation model are compared with the parametric values for the monochromatic dissipation model.

Finally, in Chapter 7 the conclusions are presented.

Chapter 2

EXPERIMENTAL FACILITY

2.1 Introduction

The experiments were conducted in the Center for Applied Coastal Research at the University of Delaware. The aim was to simulate the conditions experienced in inlets during the periods when there are fast tidal currents propagating out of the inlet. Tidal currents are turbulent and, compared to gravity waves, vary over much longer time scales. Thus, in our experiments we generate turbulent currents with a constant mean velocity. Since we wish to isolate the phenomenon of wave blocking from other effects associated with inlet geometries (such as refraction on the ebb jet), the experiments have been conducted in one dimension only. Further details about the experiments can be found in Chawla and Kirby (1999a).

2.2 Experimental Setup

The experiments were conducted in a 30 m long flume in the Center for Applied Coastal Research at the University of Delaware. A recirculating system was built on an already existing flume. All plumbing was done using PVC pipes. A schematic plan view of the setup is shown in Figure 2.1. Currents are generated with the help of a pump which draws out water from behind the wave paddle and puts it back into the flume at the other end. The width of the flume is 0.6 m and all the experiments are conducted in a water depth of 0.5 m. The wave periods range from $1.2 - 1.6$ sec, and the kh values range from $1.35 - 2.4$. Thus, the experiments have been conducted in a range from deep to intermediate water depths.

2.2.1 Perforated wavemaker

A perforated "piston-type" wave paddle is used to generate waves in the tank. This allows us to draw out the water from behind the wavemaker, and the vertical profile of the current in front of the wave paddle remains unchanged. A schematic view of the wave paddle is shown in Figure 2.2. The wave paddle is made of 1/8 in. thick stainless steel plate. Approximately 30% of the paddle surface area is perforated. The wavemaker is able to generate sinusoidal waves but due to energy leaking through the perforations the wave heights are much smaller when compared to a linear wavemaker theory for a solid plate (see Figure 2.3). A perforated wavemaker theory using a quadratic loss formulation to account for energy loss through the wave paddle has been developed for such a wavemaker by Chawla and Kirby (1999c), but has not yet been extended to include the case of non-zero mean flow through the paddle.

2.2.2 Recirculating pump and flow meter

The currents in the system are generated with the help of a 30 HP Weinman pump that pumps water at a rate of 1500 gpm under a head of 60 ft. Head loss calculations for the entire setup were done for the design current to determine the pump specifications. The pump has an 8 in. diameter suction pipe and a 6 in. diameter discharge pipe. In order to provide sufficient head and prevent cavitation, the suction end of the pump is connected to the bottom of the flume. Due to the limited space under the flume a fiberglass manifold box has been used to connect the pump to the flume (see Figure 2.4).

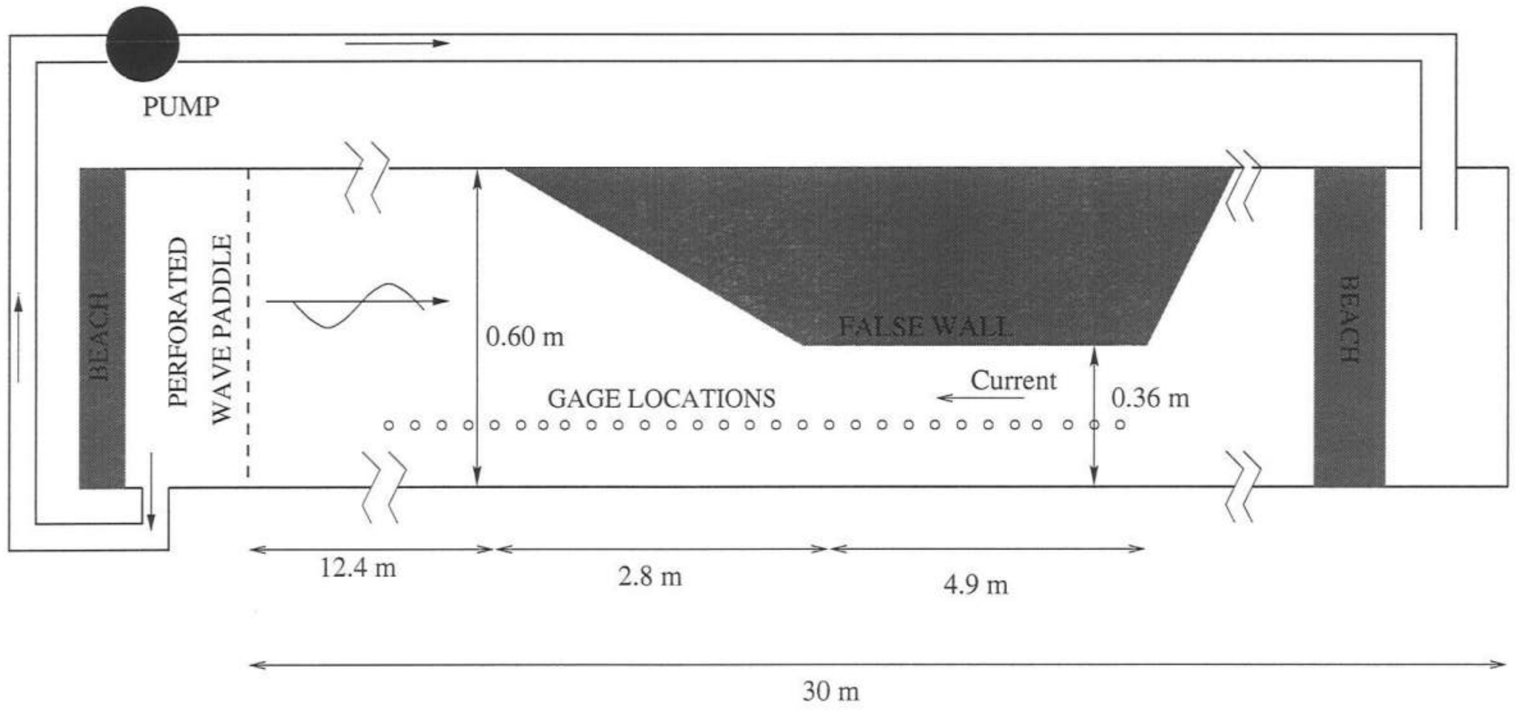

Figure 2.1: Schematic plan view of the experimental setup

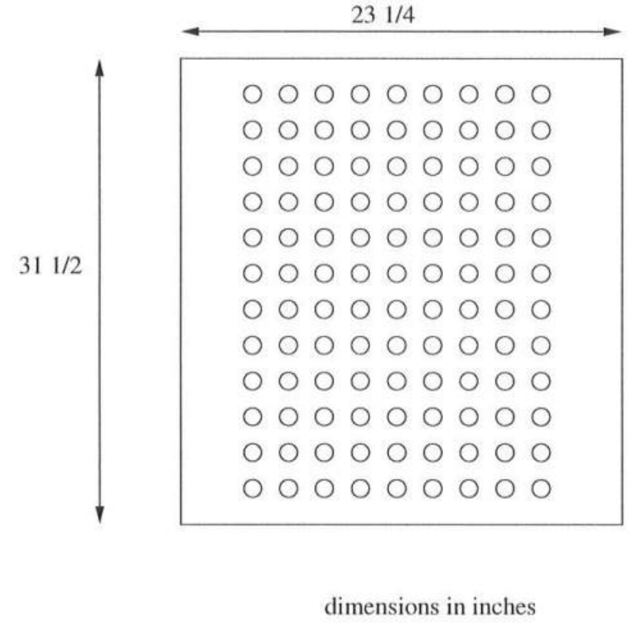

Figure 2.2: Schematic view of the perforated wave paddle

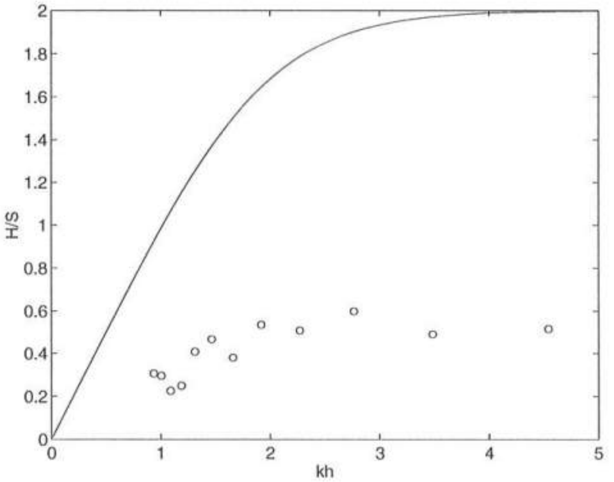

Figure 2.3: Wave height to stroke ratio comparisons;'Solid line' linear wavemaker theory for a solid plate;'circles' data from the perforated wavemaker

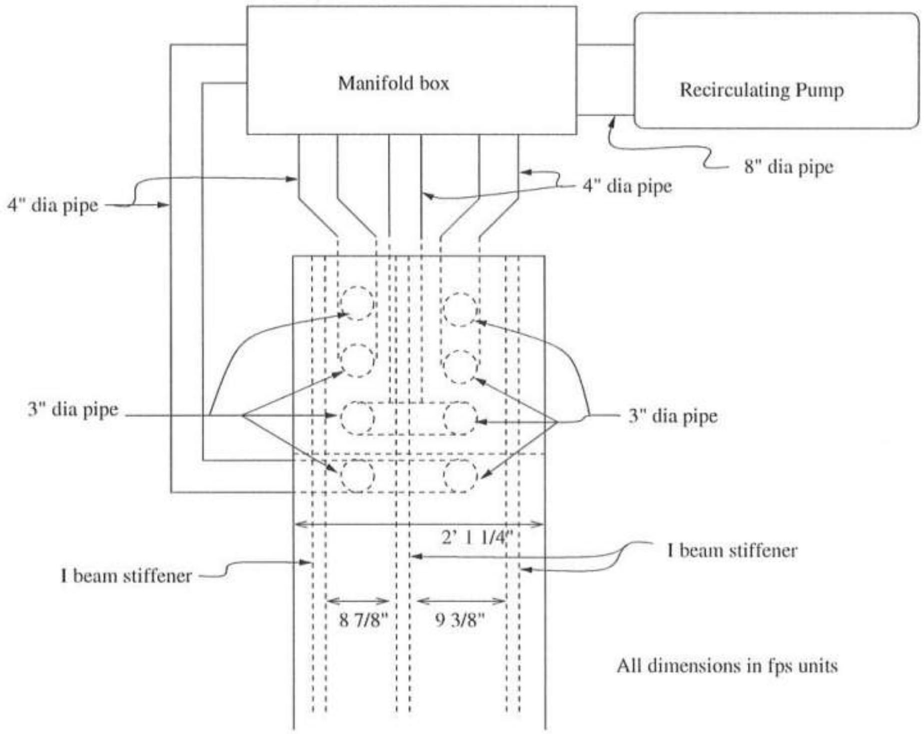

Figure 2.4: Schematic plan view showing the connection between the pump to the flume

The discharge pipe from the pump is a 6 in. diameter pipe that runs along the length of the flume and puts the water back into the flume at the far end. A Hayward 6 in. gate valve controls the flow rate. The opening and closing of the gate valve is controlled with the help of an electric actuator that is mounted on top of the valve. The default signal to the actuator is to open the valve fully. This prevents any accidental closing of the valve during operation. The flow rate is measured with the help of an Omega digital flow meter that consists of a paddle wheel sensor inserted into the discharge pipe and an instrumentation box that consists of an analog board and a relay board. The flow meter provides the time series of the instantaneous flow rate which is then recorded with the help of the data acquisition system. The calibration of the sensor is linear and is accurate to within 1%.

2.2.3 Inlet design and flow straightener

A channel with a varying width has been constructed and placed in the flume approximately 12 m from the wavemaker (see Figure 2.1), with the aim of simulating a river inlet. The channel has been constructed with epoxy coated marine grade plywood which provides a smooth finish and reduces frictional losses. The width of the narrow part of the channel is 0.36 m, and it has been designed such that the current in this region is strong enough to block waves with periods up to 1.3 s in 0.50 m of water depth. The channel expands slowly with an angle of 5° to the width of the flume to prevent flow separation in the expansion. Thus, the additional complexity of wave focusing on a laterally spreading jet is avoided. A flow straightener has also been placed in the flume close to the point where the water is discharged back into the flume. The flow straightener consists of a number of 1 ft. long pieces of 1 in diameter PVC pipes stacked in a close-packed array. Its purpose is to eliminate all the large scale eddies that are generated during the discharge of water into the flume.

2.3 Coordinate system

The origin is placed at the beginning of the narrow part of the inlet with the $x-$ coordinate axis pointing down the length of the flume and positive in the direction of the waves. Thus, the inlet begins at $x = -2.8$ m, and the narrow part of the inlet extends from $x = 0$ till $x = 4.8$ m. Due to symmetry the side wall of the flume becomes the center line of the inlet. The $y-$ coordinate axis points positive towards the false wall with $y = 0$ at the centerline (right wall of the tank). The $z-$ coordinate axis points positive upwards with $z = 0$ at the still water level.

2.4 Data Collection

Two different types of instruments have been used for collecting data. The fluid velocities have been measured with the help of a SONTEK acoustic Doppler velocimeter (ADV), and time history of the water surface is obtained with the help of capacitance wave gages.

The ADV consisted of a 10 MHz 2D probe which measured the horizontal velocities combined with a data acquisition software on a PC. The maximum velocity range of the ADV is ±2.5 m/s, and the maximum sampling frequency is 25 Hz. The probes are accurate to within ±1 cm/s. The advantage of using the ADV is that it is factory calibrated and sturdy enough that it does not require any further calibration. The probe has problems in making measurements if the velocities are too small or if the water is very clear. The software calculates an ADV correlation coefficient which is a data quality parameter obtained from the velocity calculations. The correlation is expressed as a percentage with a perfect correlation of 100% indicating reliable low noise measurements. The usable range for reliable data is 70 to 100%. In our experiments the current velocities were strong enough to give around 90% correlation. The limitation of the ADV is that its maximum sampling rate is only 25 Hz which means that the upper limit to which data can be resolved is 12.5 Hz. Thus, turbulence measurements cannot be made for the higher frequencies. Nevertheless, it gives very good estimates of the rms turbulence intensities and mean velocity profiles (see Chawla and Kirby (1999a) for detailed plots).

Capacitance wave gages have been used in the experiments to measure the time history of the water surface. The surface gage measurements extend from outside the inlet to the end of the narrow part of the inlet and are shown in Figure 2.1. The gages are calibrated so as to be able to convert the measured time series from volts to centimeters. All the gages are sturdy in the sense that the calibration curves are linear with very little drift. A typical calibration curve for 4 gages is shown in Figure 2.5. Changes in water temperatures affect the calibration curves slightly and calibration must be done at least once a day. In our experiments, calibration of the gages was done every time the gages were moved so as to ensure the proper functioning of the gages. Thus, typically calibration of the gages was done 3 to 4 times a day. Both the calibration and collection of data from the gages is done with the help of a Concurrent 7200 data acquisition computer system. The computer system contains 80 A/D channels which converts the analog signals from the wave gages into digital signals. Unlike the ADV, there is no limit to the rate at which data can be sampled by the gages. A higher sampling rate is preferred because it gives finer spectral resolution; however, for a fixed length of time of a data record, a higher sampling rate means that more data points have to be sampled. Thus, for the random wave tests where the data had to be recorded for long lengths of time a sampling frequency of 50 was used, while for the monochromatic wave tests and narrow-banded spectral tests the sampling frequency was close to 100 Hz. The sampling frequency for the periodic tests varied with the wave period, and was chosen such that the data record contained an integer number of waves.

The Concurrent 7200 computer system is also used to run the wavemaker. It

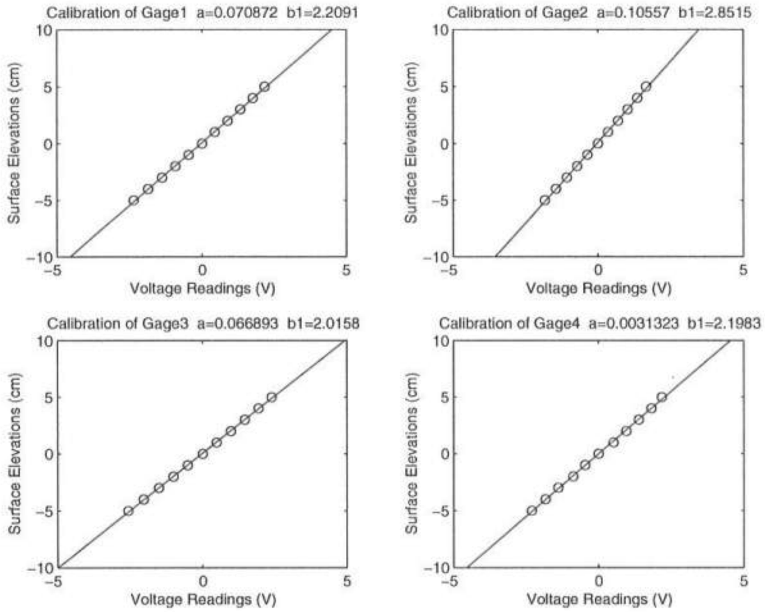

Figure 2.5: Calibration plots for capacitance gages (cm = b1*V + a)

has 4 D/A boards, and one of the boards is connected to the wavemaker. The sampling frequency for moving the wavemaker was around 4000 Hz for our experiments, eliminating the need for analog filtering of the command signal.

2.5 Current profiles

One of the primary assumptions in our study has been that the currents are depth uniform with no cross channel variations. To test whether such an assumption is valid for the currents generated in the flume, a detailed measurement of the current vertical profile was done at various locations along and across the flume through the varying channel. At each position the horizontal velocity in the x direction has been measured as a time series with the help of the ADV. Data sampling has been done at 25 Hz for 330 s. Figure 2.6 shows the vertical velocity profile at 5 different locations along the channel. U refers to the mean current defined by

$$U \equiv < u(t) >$$

The mean current has a slight shear due to the bottom boundary layer. The variations over depth are small, specially close to the narrow part of the inlet where wave blocking occurs. Thus, the current is assumed to be uniform in the channel cross section and given by

$$U \equiv -\frac{Q}{bh} \tag{2.1}$$

where b is the width of the channel, h the water depth, and Q is the measured volume flux. Boundary layer effects have been ignored in (2.1), leading to lower predicted mean currents. To account for this the value of Q was artificially increased from 0.089 to 0.095 m^3/s (see Figure 2.7).

One of our major concerns in designing the channel was to prevent flow separation from the side walls. To check for flow separation, cross channel velocity profile measurements were made both for the case of large breaking waves on a current ($H \approx 0.12$ m, T = 1.2 s) and also for the case of the flow alone. Figures 2.8 and 2.9 show the cross channel vertical velocity profiles at two different horizontal locations in the channel. Though there is some amount of cross channel variation in the flow, the velocity profiles do not indicate that the flow is separating in the varying channel, even in the presence of large breaking waves.

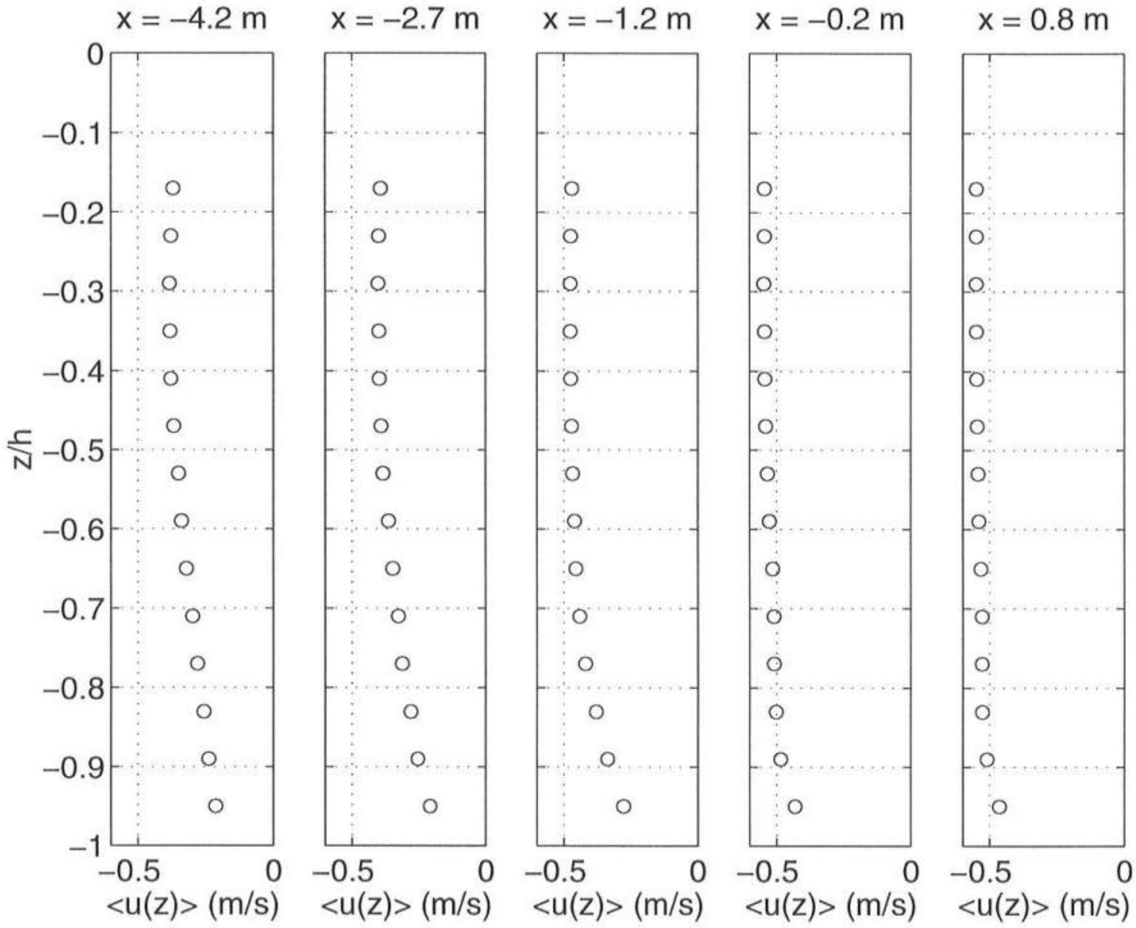

Figure 2.6: Vertical mean current profiles at 5 different locations in the channel.

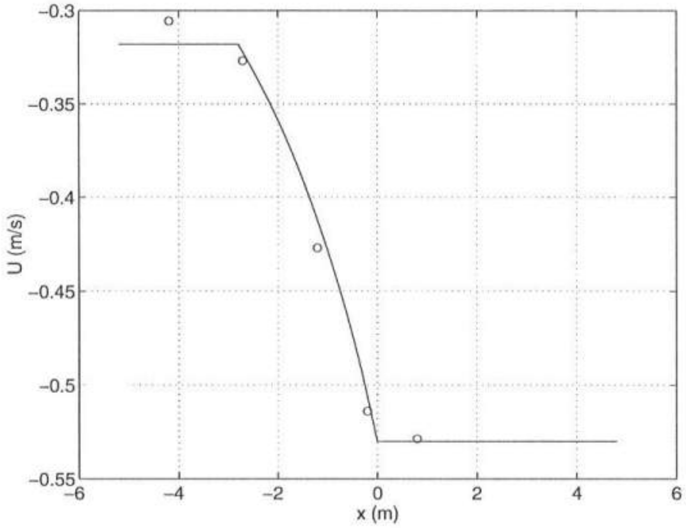

Figure 2.7: Average current as a function of x. '−' Q/bh; '○' data

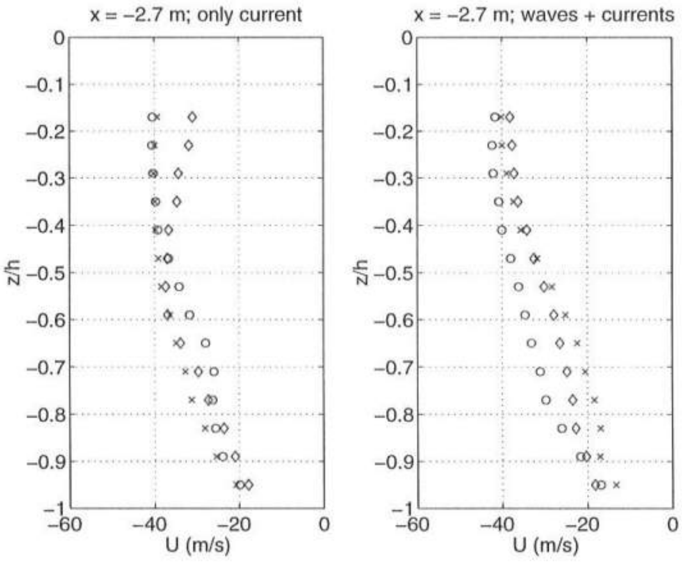

Figure 2.8: Mean velocity profiles at $x = -2.7$m;'○' $y/b = 0.25$,'×' $y/b = 0.5$,'◇' $y/b = 0.75$

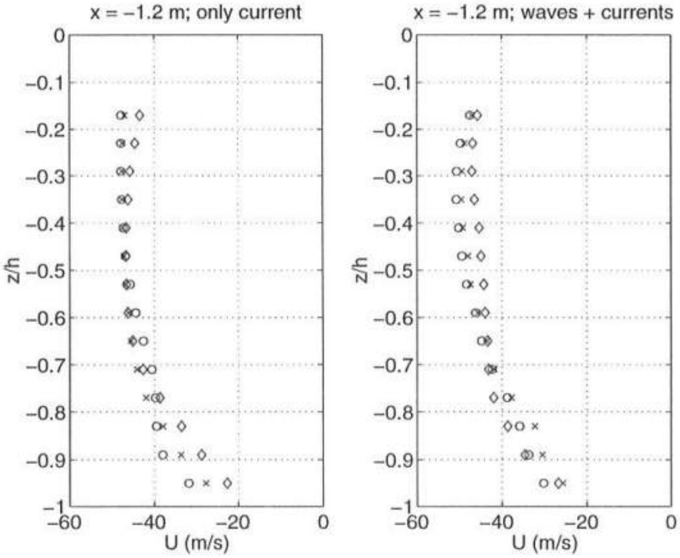

Figure 2.9: Mean velocity profiles at $x = -1.2$m;'$\circ$' $y/b = 0.28$,'$\times$' $y/b = 0.5$,'$\diamond$' $y/b = 0.72$

Chapter 3

EXPERIMENTS ON MONOCHROMATIC WAVES

3.1 Introduction

Experiments on monochromatic waves were divided into two parts: the small amplitude tests in which waves are reflected from the blocking point without any breaking and the large amplitude tests where the waves break at or before the blocking point and wave reflection is suppressed. In both cases a range of wave heights for different wave periods have been considered. The aim is to study the evolution of the amplitude envelope through the blocking region and quantify the effects of a varying wave height and period as well as the energy decay due to steepness limited wave breaking. A version of this presentation also appears in Chawla and Kirby (1998).

3.2 Small amplitude tests - wave reflection

Wave reflection from the blocking point occurs only when the incident wave is small enough such that there is no wave breaking at or before the blocking point. Since wave energy cannot propagate beyond the blocking point, and no energy is lost due to wave breaking, the waves get reflected back. The reflected waves are peculiar in the sense that their phase speed is still moving against the current, but their group velocity moves with the current. In other words the wave energy is washed down stream by the currents. As the waves propagate further away from the blocking region, they continue to get shorter and shorter. Close to the blocking point, the incident and reflected waves superimpose to form the typical nodes and antinodes patterns in the amplitude envelope.

There are several references in the literature on the evolution of the amplitude envelope through the blocking region for the linear limit. A review on the subject is given in Chapter 1. According to linear theory the amplitude envelope through the blocking point is an Airy function, and is given by (Trulsen and Mei, 1993)

$$a(x) = b_0 Ai\big(-\alpha^{2/3}(x - x_{bp})\big) \tag{3.1}$$

where b_0 is a constant related to the incident amplitude, x_{bp} is the location of the blocking point and α is given by

$$\alpha = \sqrt{\left(\frac{-2\dfrac{\partial U}{\partial x}k\sigma}{3U^2}\right)_{x=x_{bp}}}$$

3.3 Experimental tests

To study this phenomenon of wave reflection a total of 15 test cases were run. The tests were divided into three groups. Each group consisted of 5 test cases having a constant wave period and increasing wave heights. The incident wave heights were gradually increased to study the effects of nonlinearity on the shape of the amplitude envelope. Wave blocking occurred close to the narrowest part of the channel ($x = 0$). To capture the variation in the amplitude shape close to the blocking region, 43 gage measurements were made between $x = -1.5$ m and $x = 0.8$ m. At each gage location the time series was recorded for 256 wave periods. The initial conditions were obtained from the first gage at $x = -4.6$ m, and is tabulated in Table 3.1.

Table 3.1: Parameters for monochromatic wave reflection tests determined at $x = -4.6$ m

Test No.	T (s)	H (m)	Sampling freq (Hz)
1	1.2	0.012	83.333
2	1.2	0.013	83.333
3	1.2	0.014	83.333
4	1.2	0.015	83.333
5	1.2	0.016	83.333
6	1.2	0.013	83.333
7	1.3	0.015	76.923
8	1.3	0.018	76.923
9	1.3	0.021	76.923
10	1.3	0.024	76.923
11	1.3	0.015	76.923
12	1.3	0.020	76.923
13	1.4	0.025	71.429
14	1.4	0.032	71.429
15	1.4	0.038	71.429

3.4 Comparisons with linear theory

Wave height distributions for all the 15 test cases are shown in Figure 3.1. The change in the shape of the amplitude envelope, with increasing wave amplitude, is clearly visible when we move from Test 1 to 5. The waves change from being reflected at the blocking point to breaking at the blocking point with little or no blocking as is evident from the lack of nodal and antinodal points in Test 5. Tests 6 to 10 are similar. In the case of Test 11, according to linear theory, no blocking should occur. But partial wave reflection still occurs because the required blocking current is close to the maximum current (Stiassnie and Dagan, 1979). With increasing amplitude, the required blocking current moves further away from the maximum current, and no wave reflection pattern is observed.

The comparison between the Airy solution (3.1) and the amplitude envelope

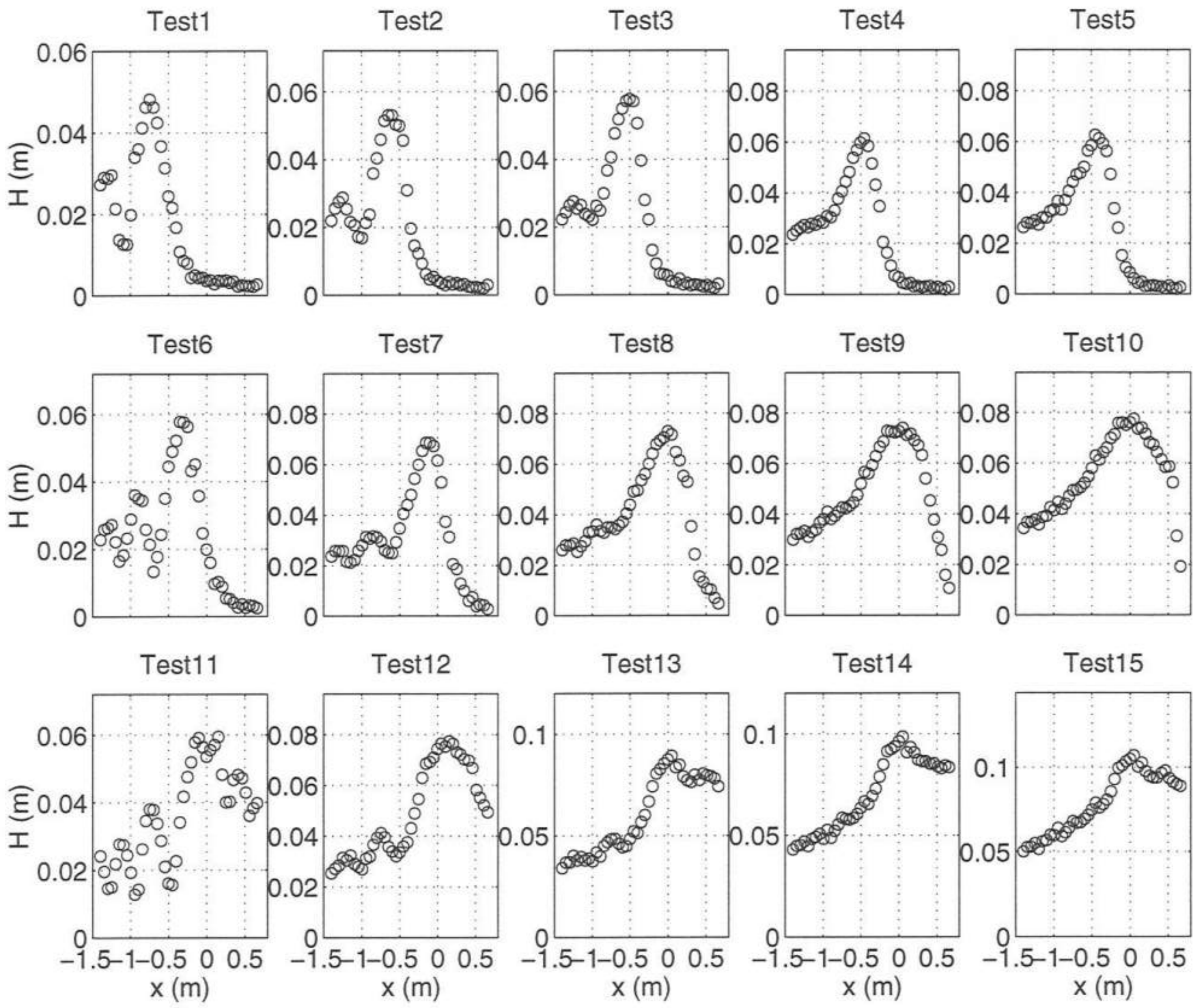

Figure 3.1: Wave height distribution for monochromatic wave reflection tests

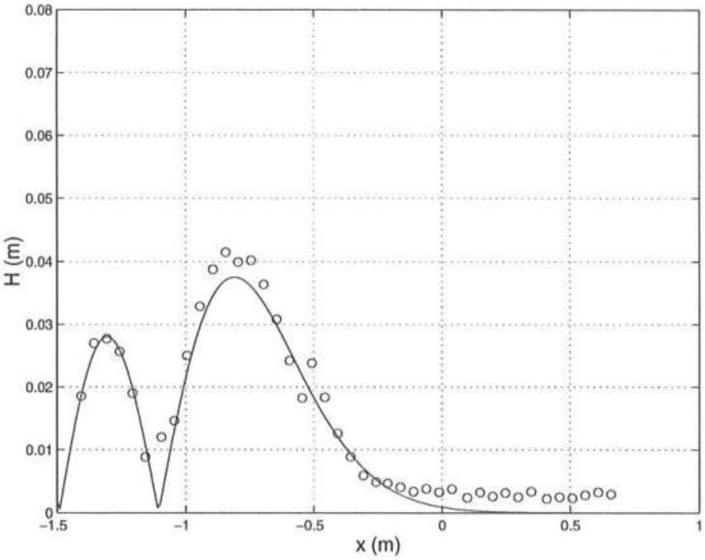

Figure 3.2: Comparison between measured amplitude envelope ('o') and Airy function for test 1

for Test 1 is shown in Figure 3.2. The comparison is good except at the crest of the front, where the deviations are probably due to nonlinear effects. The deviation between the Airy solution and the measured data increases with wave amplitude (Figure 3.3), and when the waves start breaking the measured envelope no longer resembles an Airy function.

3.5 Large amplitude tests - wave breaking

A total of 18 breaking wave test cases were run. The tests have been divided into 3 groups. Each group consists of 6 cases in which the wave period is kept constant and the wave height varied from small to large values. Data has been collected in the form of a time series of the water surface with the help of the capacitance wave gages. Data was recorded for 256 wave periods, and for each test a detailed data set at 29 gage locations has been obtained. The data set from the first gage (located at $x = -5.2$ m) is used to determine the initial conditions (see

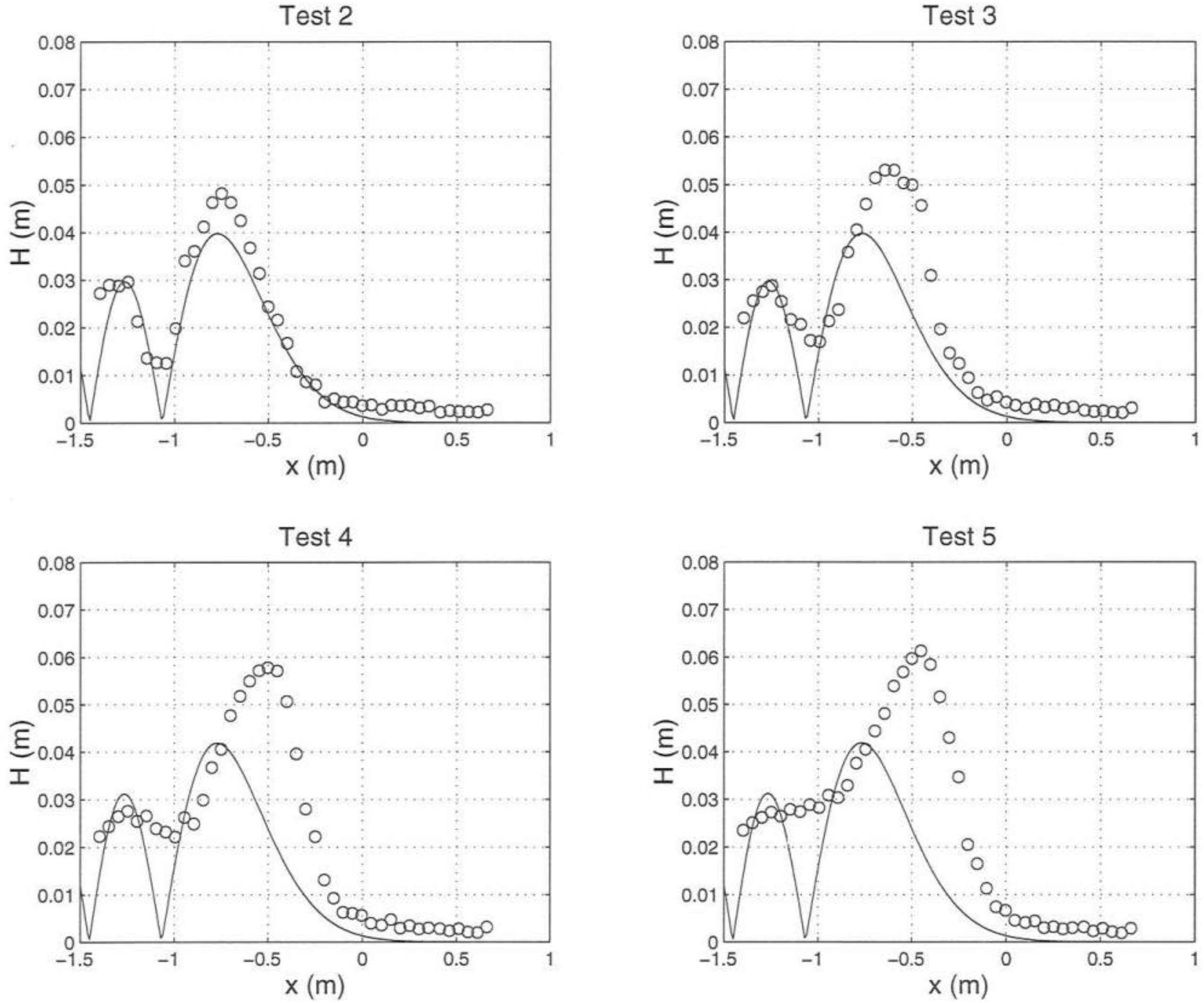

Figure 3.3: Comparison between measured amplitude envelope ('∘') and Airy function for tests $2-5$

Table 3.2: Parameters for monochromatic breaking wave tests determined at $x = -5.2$ m

Test No.	T (s)	H (m)	Sampling freq (Hz)
1	1.2	0.012	83.333
2	1.2	0.018	83.333
3	1.2	0.033	83.333
4	1.2	0.066	83.333
5	1.2	0.095	83.333
6	1.2	0.126	83.333
7	1.3	0.014	76.923
8	1.3	0.029	76.923
9	1.3	0.057	76.923
10	1.3	0.084	76.923
11	1.3	0.104	76.923
12	1.3	0.130	76.923
13	1.4	0.016	71.429
14	1.4	0.026	71.429
15	1.4	0.071	71.429
16	1.4	0.096	71.429
17	1.4	0.117	71.429
18	1.4	0.141	71.429

Table 3.2). Wave blocking conditions were satisfied for the 1.2 sec. and some of the 1.3 sec. waves, while the 1.4 sec. waves were never blocked. Repeatability tests showed that the experiments were repeatable to within 6% error in wave height (see Chawla and Kirby (1999a) for details). All the wave properties are deduced from the time series of the water surface with the help of a zero-upcrossing method.

3.5.1 Numerical model

A simple numerical model has been developed to study wave breaking. The model uses the wave action conservation principle first derived by Bretherton and

Garrett (1969). The conservation principle is given by

$$\frac{\partial}{\partial t}\left(\frac{E}{\sigma}\right)+\nabla\cdot\left(\frac{E}{\sigma}C_{ga}\frac{\mathbf{k}}{k}\right)=0 \tag{3.2}$$

where, E is the wave energy, C_{ga} the group velocity, σ the intrinsic wave frequency and k the wave number.

Assuming steady wave conditions eliminates the first term in (3.2). Also since we are trying to model wave flow in a narrow channel, flow variation across the channel is assumed to be small and (3.2) is integrated over the width of the channel. Adding a dissipation term for wave breaking, the final model equation can be written as

$$\frac{1}{b}\left[\frac{\partial}{\partial x}\left(\frac{bEC_{ga}}{\sigma}\right)\right]=\frac{D}{\sigma} \tag{3.3}$$

where, b is the channel width, and D determines the energy loss due to wave breaking. D is unknown and has to be determined empirically as there is no theoretical solution available.

3.5.1.1 Energy dissipation model

LeMéhauté (1962) first hypothesized that the energy dissipation in a breaking wave can be modeled by the energy dissipation in a moving bore. This idea has been used with reasonable success in simulating depth limited wave breaking (e.g. Battjes and Janssen, 1978). Though the bore model has been derived for shallow water wave breaking, the same idea will be used here to determine an energy dissipation term for current limited wave breaking.

Consider a bore connecting two regions of uniform flow (Figure 3.4). Using the control volume approach, the energy dissipation per unit width across the bore is given by

$$D'=-\frac{1}{4}\rho g(h_2-h_1)^3\sqrt{\frac{g(h_2+h_1)}{2h_2h_1}} \tag{3.4}$$

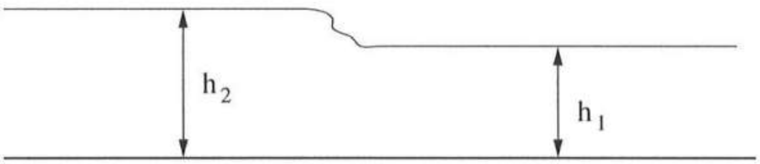

Figure 3.4: Sketch of a single steady bore.

The length scales h_2 and h_1 can then be associated with the wave parameters

$$h_2 - h_1 \sim H \tag{3.5a}$$

$$\frac{(h_2 + h_1)}{2h_2h_1} \sim \frac{1}{\zeta} \tag{3.5b}$$

where H is the wave height and ζ is a vertical length scale which needs to be prescribed. For depth limited breaking models, ζ is given by the water depth h. But for current limited breaking models this would not be a useful scale as wave breaking can occur in deep water too. Instead we use

$$\zeta = \frac{\tanh kh}{k} \tag{3.6}$$

where $\zeta \to h$ in shallow water and $\zeta \to k^{-1}$ in deep water. We get

$$D' = -\frac{\beta}{4}\rho g(H)^3\sqrt{\frac{gk}{\tanh kh}} \tag{3.7}$$

where β is a non-dimensional parameter which relates D' to energy dissipation in breaking waves. Now, D' is the energy dissipation rate over the entire wave, and thus, the dissipation rate per unit area is given by

$$D = \frac{D'}{L} = -\beta\frac{\rho}{8\pi}\left(\sqrt{\frac{(gk)^3}{\tanh kh}}\right)H^3 \tag{3.8}$$

In shallow water, (3.8) reduces to the standard bore model used in depth limited wave breaking (Battjes and Janssen, 1978), except that the parameter β will have a different value.

Apart from an expression for energy dissipation we also need a criterion for the onset of wave breaking. Since wave breaking on opposing currents occurs due to the waves becoming very steep, a steepness limited criterion based on Miche's criterion is used

$$\frac{kH_b}{\gamma \tanh kh} = 1 \tag{3.9}$$

where γ is a non-dimensional parameter.

Eqns. (3.3) together with (3.8) and (3.9) provide a simple linear model for monochromatic waves shoaling and breaking on opposing currents. The model uses the wave action conservation principle, and becomes singular at the blocking point. This is because the wave action conservation principle is based on ray theory, which is not valid close to the blocking point since it forms a caustic. Since the location of the blocking point is determined by the dispersion relation, the model is run using both a linear dispersion relation

$$\sigma = \sqrt{gk \tanh kh} \tag{3.10}$$

and a 3^{rd} order Stokes dispersion relation (Bowden, 1948)

$$\sigma = \sqrt{gk \tanh kh \left[1 + (ka)^2 \left(\frac{8 + \cosh 4kh - 2\tanh^2 kh}{8 \sinh^4 kh}\right)\right]} \tag{3.11}$$

to quantify the importance of amplitude dispersion in determining the model response.

3.5.2 Data to model comparisons

Tests 1, 2, 7, 8, 13 and 14 have small initial amplitudes and results from these cases are essentially similar to the tests for wave reflection. Thus, these tests have been omitted in the present analysis. The parameters β and γ were set to 0.1 and 0.6 respectively.

The wave height comparisons are shown in Figure 3.5. In all the tests the wave heights have been normalized with the initial wave height. The model works much better when using a Stokes dispersion relation as opposed to the linear dispersion relation. This is because close to the blocking point the waves steepen quite considerably and terms of $O(ka)^2$ are no longer small enough to be neglected. The shoaling properties are quite accurately predicted by the wave action conservation principle. We also find that a bore dissipation model does a reasonable job in predicting energy dissipation due to wave breaking.

The heirarchial nature of the blocking effect can be observed as we increase the wave height keeping the wave period constant. In test 3 waves are blocked at the entrance of the channel. Due to non-linear effects the actual blocking occurs later than predicted by linear theory. When the wave height is increased further in test 4, the required blocking current is greater than the maximum current in the system. Thus the waves reach the narrow channel without getting blocked. At this point if the wave amplitude remains unchanged then the waves should propagate right through the channel. However the waves continue to lose energy due to wave breaking and they propagate into the channel till the amplitude becomes small enough for the maximum current to block the waves. It is therefore very important to be able to predict energy decay due to current limited wave breaking to accurately simulate wave blocking.

Since the wave breaking is occurring in deep water, we can also use a white-capping model (Hasselmann, 1974) to determine the energy dissipation in the waves. In a white-capping model

$$D = -\beta_c \sigma E \tag{3.12}$$

where E is the wave energy, and 0.02 is the calibrated value used for parameter β_c . The comparison between the bore model and the white-capping model is shown in Figure 3.6. The two models give very similar results, and we shall stick with the bore model because it can also be used in shallow water.

Another point that comes to attention is that though the blocking point is well predicted by the Stokes dispersion relation in cases like Tests 3 and 4, the model fails in this respect in Tests 5 and 6. To get an idea of why this happens we take a look at the wave period distribution for all the tests, given in Figure 3.7. The wave period data beyond the blocking point is scattered due to fluctuations in the water surface caused by the turbulence in the current. These fluctuations are on the order of 1 cm, and are perceived as waves by the zero-upcrossing method. From the figure we see that in Tests 5 and 6 the wave period shifts from a 1.2 sec period to a 1.4 sec period, for which the blocking conditions are not satisfied. This tendency is most pronounced in Tests 5 and 6, but can also be seen to a smaller extent in Tests 9 to 12. It is absent in the 1.4 sec wave tests.

The shift to longer wave periods occurs due to the development of side band instabilities. Benjamin and Feir (1967) showed that water waves are unstable to side band growth and the growth of these instabilities depend upon the frequency and wave amplitude. Due to the increase in wave steepness, they become highly pronounced when the waves are riding on opposing currents and have been observed in the laboratory (Lai *et al.*, 1989). Their effects become even greater as the waves approach the blocking point, because the group velocity C_{ga} tends to zero and the wave energy travels very slowly. Thus, a significant amount of energy could be transferred from the primary wave to the side bands even through small spatial distances, as the time available for the interaction to take place is large. Since the lower side band requires a stronger blocking current than the primary wave or the upper side band, it can continue to propagate forward while the other two are blocked. This effect can be clearly observed in the frequency spectra for Test 6 (see Figure 3.8). As the spectrum moves into stronger currents, the energy is transferred

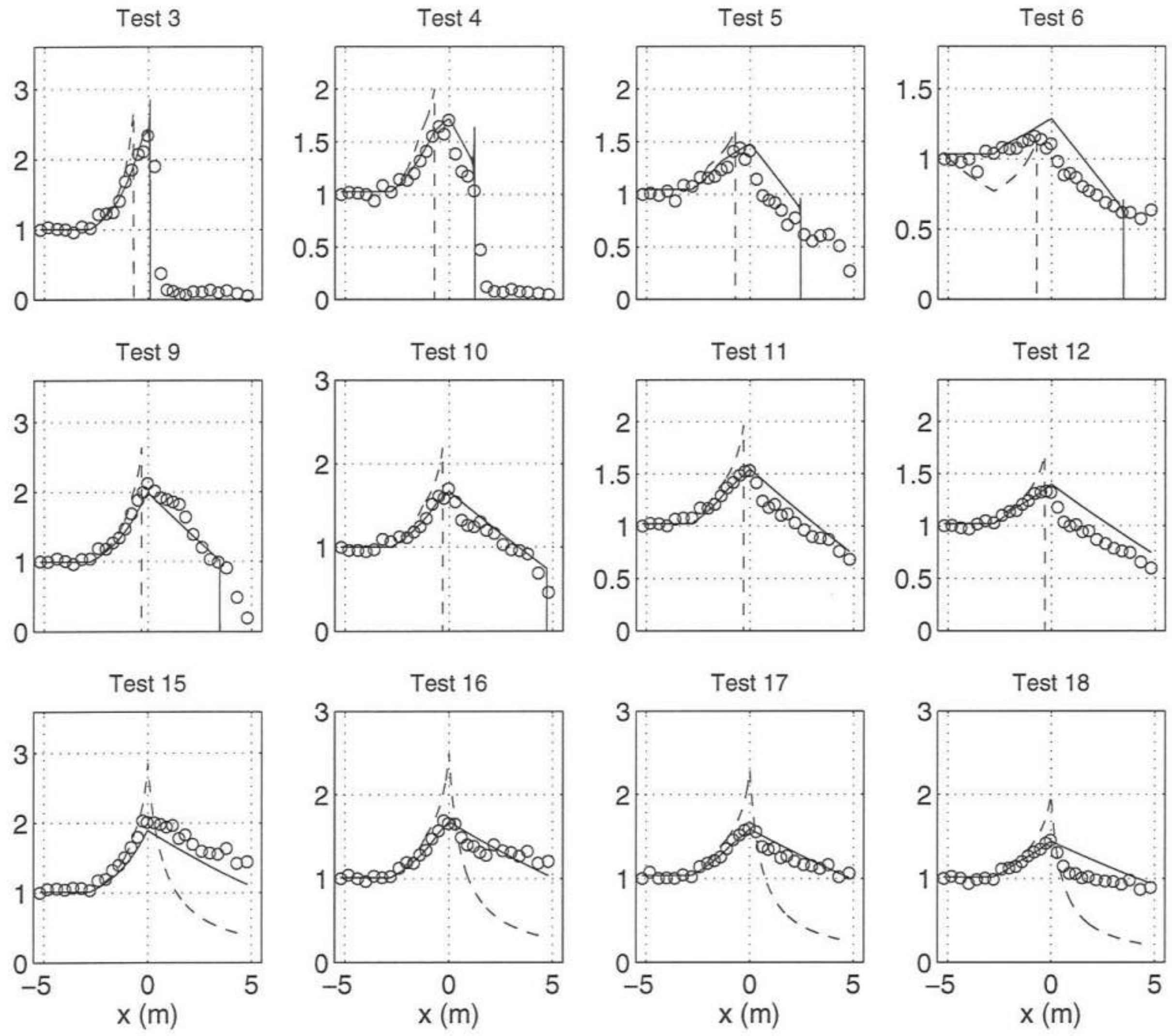

Figure 3.5: Normalized H for monochromatic wave tests ('solid line' Stokes dispersion relation; 'dashed line' linear dispersion relation; 'o' data).

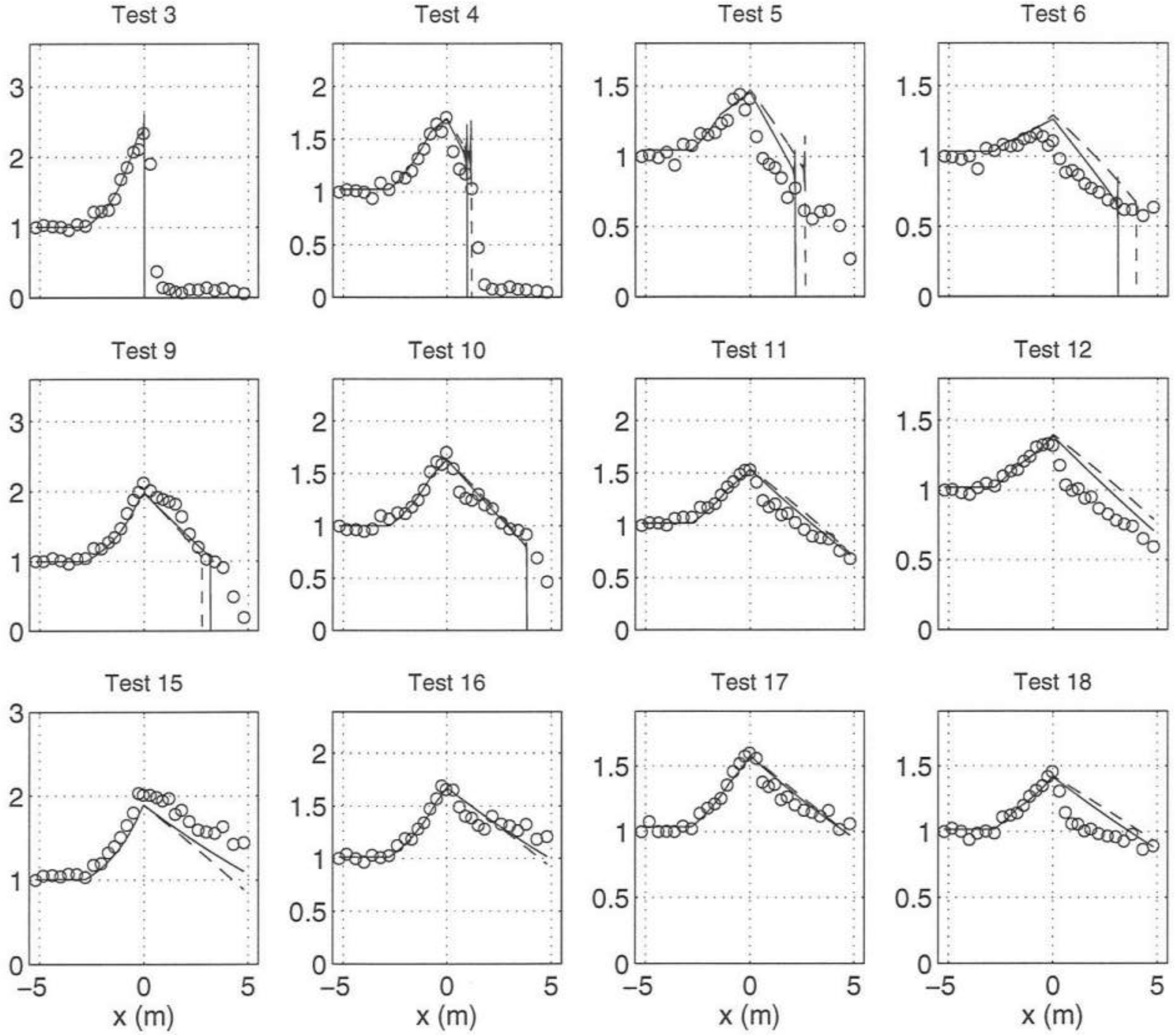

Figure 3.6: Normalized H for monochromatic wave tests ('solid line' Bore model; 'dashed line' White capping model; 'o' data).

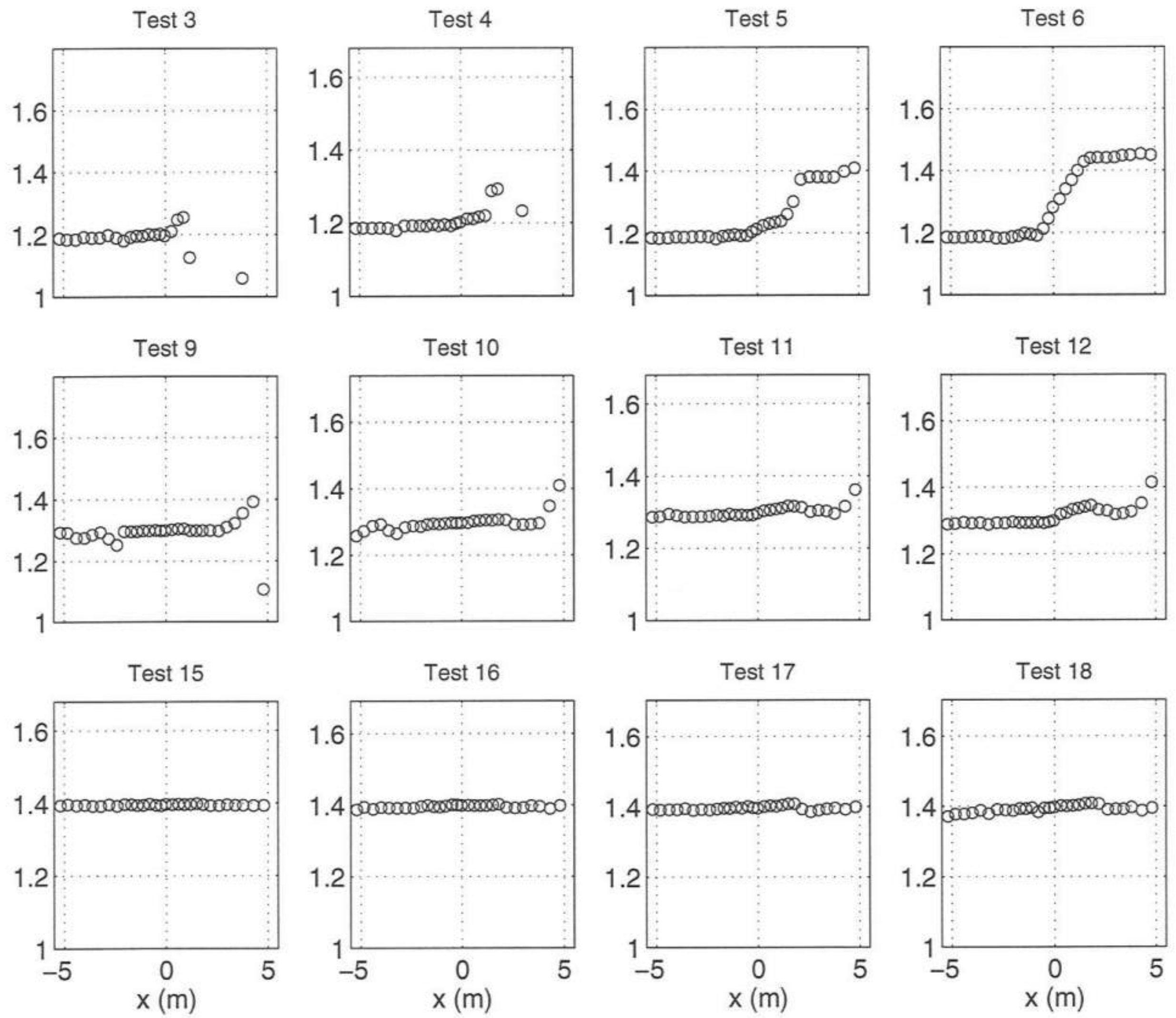

Figure 3.7: Measured wave period T_p for monochromatic wave tests.

to the lower side band, while the upper side band and primary wave component get blocked. In particular note that between $x = -0.5$ m to $x = -0.03$ m, the energy in the lower side band increases by almost 10 times. In the narrow channel the blocking condition for the primary wave component and the upper side band is satisfied and they get blocked, while the lower side band propagates right through the channel. The occurance of this effect depends both upon the growth of the side band instabilities and the position of the primary wave component in the frequency spectrum. Our simple linear model cannot simulate this phenomenon, and a more detailed analysis is required.

3.6 Summary

Experimental studies on a series of monochromatic waves on an opposing blocking current have been conducted. The experiments can be broadly classified into two groups – small amplitude tests where the waves are reflected from the blocking point, and the large amplitude tests where wave breaking occurs with no reflection.

In the wave reflection tests we find that the measured envelope is an Airy function for the smallest waves, Thus confirming the predictions of linear theory. With increasing non-linearity the amplitude envelope deviates from the Airy function and there is a transition region between the case where the waves are reflected from the blocking point with no breaking to the case where waves break at the blocking point with no reflection. Partial wave reflection was also observed in cases where the required blocking current is slightly greater than the maximum current.

In the breaking wave tests a simple wave action conservation model together with a modified bore dissipation breaking model is used to simulate the data. Comparisons show that amplitude dispersion plays an important role in determining wave blocking due to the rapid increase in the wave steepness close to the blocking

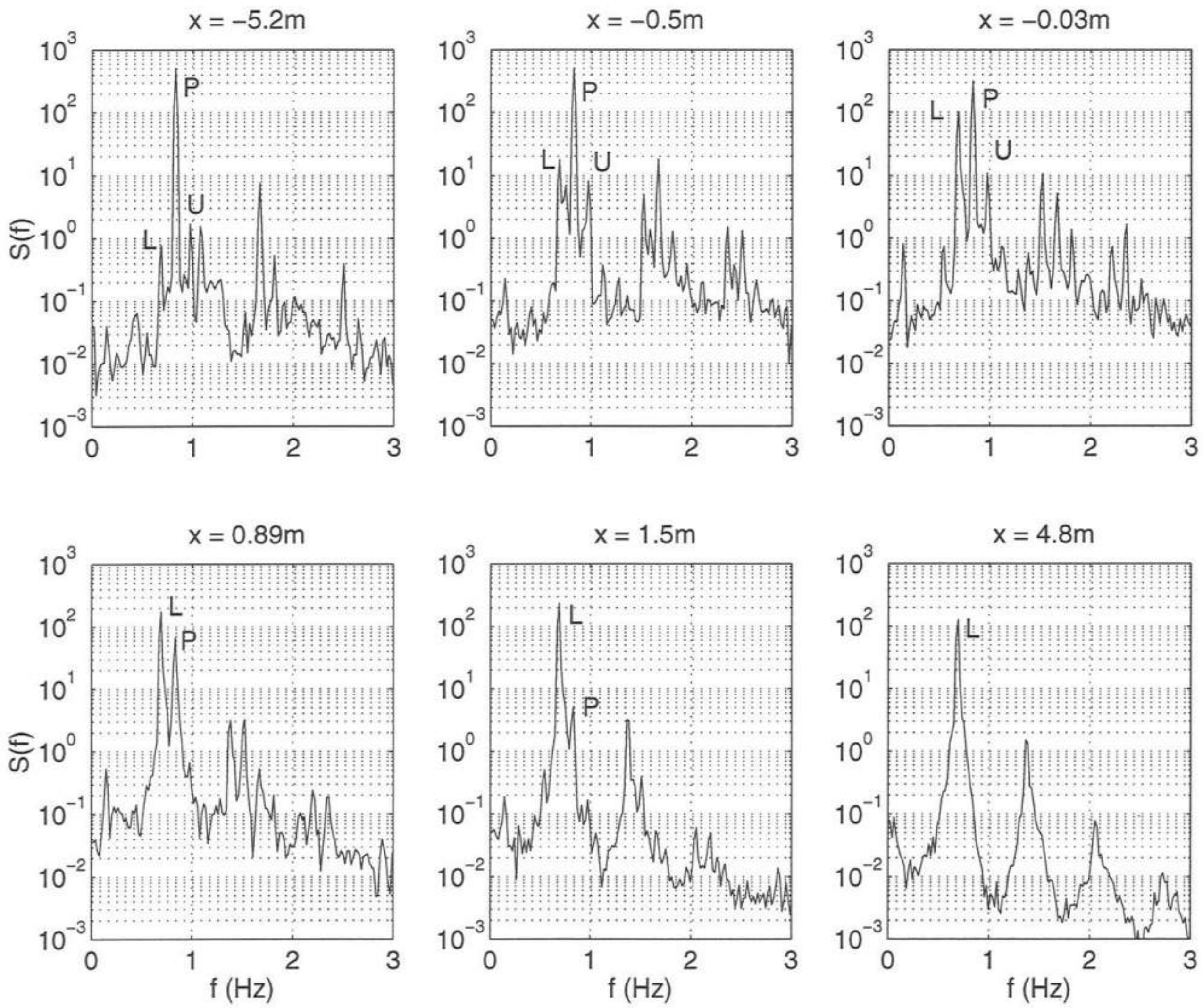

Figure 3.8: Frequency spectra for Test 6 at different locations ('L' lower side band; 'P' primary wave component; 'U' upper side band).

point, and a third order Stokes dispersion relation works much better than a linear dispersion relation in predicting the blocking point. The energy decay is predicted reasonably well with the modified bore model. The advantage of using this dissipation model to simulate energy decay due to current limited wave breaking is that in shallow water it asymptotes to the standard bore model used to simulate depth limited wave breaking (Battjes and Janssen, 1978). However, it should be kept in mind that though the dissipation models for current limited and depth limited breaking are very similar, the parametric coefficients β and γ for the two processes are very different.

In some of the cases, the wave energy for the largest amplitudes was shifted to lower frequencies due to side band instabilities and the waves were not blocked. The growth of side bands can be accentuated close to the blocking point due to the increased wave steepness and the longer temporal scales at which the energy propagates, leading to significant energy transfer to the lower frequencies. The growth of side bands also makes the waves very groupy, which in turn increases the complexity of wave breaking. It is thus clear that side bands in a carrier wave play an important role in determining whether waves are blocked or not, and ignoring them could lead to significant errors in wave modeling.

From our experimental studies on monochromatic waves we find that there is a hierarchy in the wave field characteristics. As the initial wave amplitude on a blocking current is increased the waves

1. are blocked and reflected,
2. are blocked and break at the blocking point,
3. pass through the maximum current due to amplitude dispersion but break and still get blocked, and

4. transfer significant energy to a lower side band which does not get blocked while the primary wave and the upper side band do.

Chapter 4

NARROW-BANDED SPECTRAL TESTS

4.1 Introduction

The excess momentum released by waves breaking on a beach acts as a forcing mechanism for fluid motion in the nearshore region. Due to the irregular nature of wave motion, the breaker line is always moving. This moving breaker line has been identified as one of the mechanisms for generating long waves in the nearshore region. To study if it was possible to similarly generate long waves downstream of a moving blocking point, a series of experiments were conducted on narrow banded spectral waves. The temporally varying amplitude envelope of a narrow banded spectrum creates a moving blocking point. Two sets of experiments were conducted. The first set consisted of a series of tests on wave groups generated by a bichromatic spectrum, while the second set was a series of tests on wave packets generated by a Gaussian shaped spectrum.

4.2 Wave groups

Wave groups were constructed by superposing two monochromatic waves having the same amplitude but slightly different frequencies. The difference between the frequencies determining the number of waves in a group. Three different sets of wave groups were used. Each set consisted of 4 different energy levels, making a total of 12 tests. The test particulars are given in Table 4.1, where the tests with

Table 4.1: Parameters for wave group tests determined at $x = -4.6$ m

Test No.	T_1 (s)	T_2 (s)	H_s (m)	Sampling freq (hz)
1	1.06	1.2	0.028	88.889
2	1.06	1.2	0.054	88.889
7	1.06	1.2	0.068	88.889
8	1.06	1.2	0.098	88.889
3	1.01	1.3	0.028	87.912
4	1.01	1.3	0.054	87.912
9	1.01	1.3	0.068	87.912
10	1.01	1.3	0.083	87.912
5	1.15	1.3	0.025	82.051
6	1.15	1.3	0.053	82.051
11	1.15	1.3	0.074	82.051
12	1.15	1.3	0.089	82.051

similar input spectrum have been grouped together. 36 gage measurements were made for each test between $x = -4.6$ m and $x = 4.61$ m.

The frequency spectra at the first gage ($x = -4.6$ m) for all the test cases are shown in Figure 4.1. The figure shows that though the signal that was sent to the wavemaker is bichromatic, the waves do not remain bichromatic by the time they reach the first gage. For the larger wave amplitude tests, wave energy is transferred to the side bands. Also when the frequency of one of the design wave components is close to 1 hz, the growth of an anomalous third wave component is observed. This anomalous wave component does not have significant energy in tests 5,6,11 and 12, where the design frequencies are further away from 1 hz. The cause for this anomaly is not very clear and is currently under study. The corresponding time series for these tests are shown in Figures 4.2 to 4.4.

The cleanest wave groups were observed for test 6 as there are only two wave components in the spectrum (see Figure 4.1). The evolution of the wave

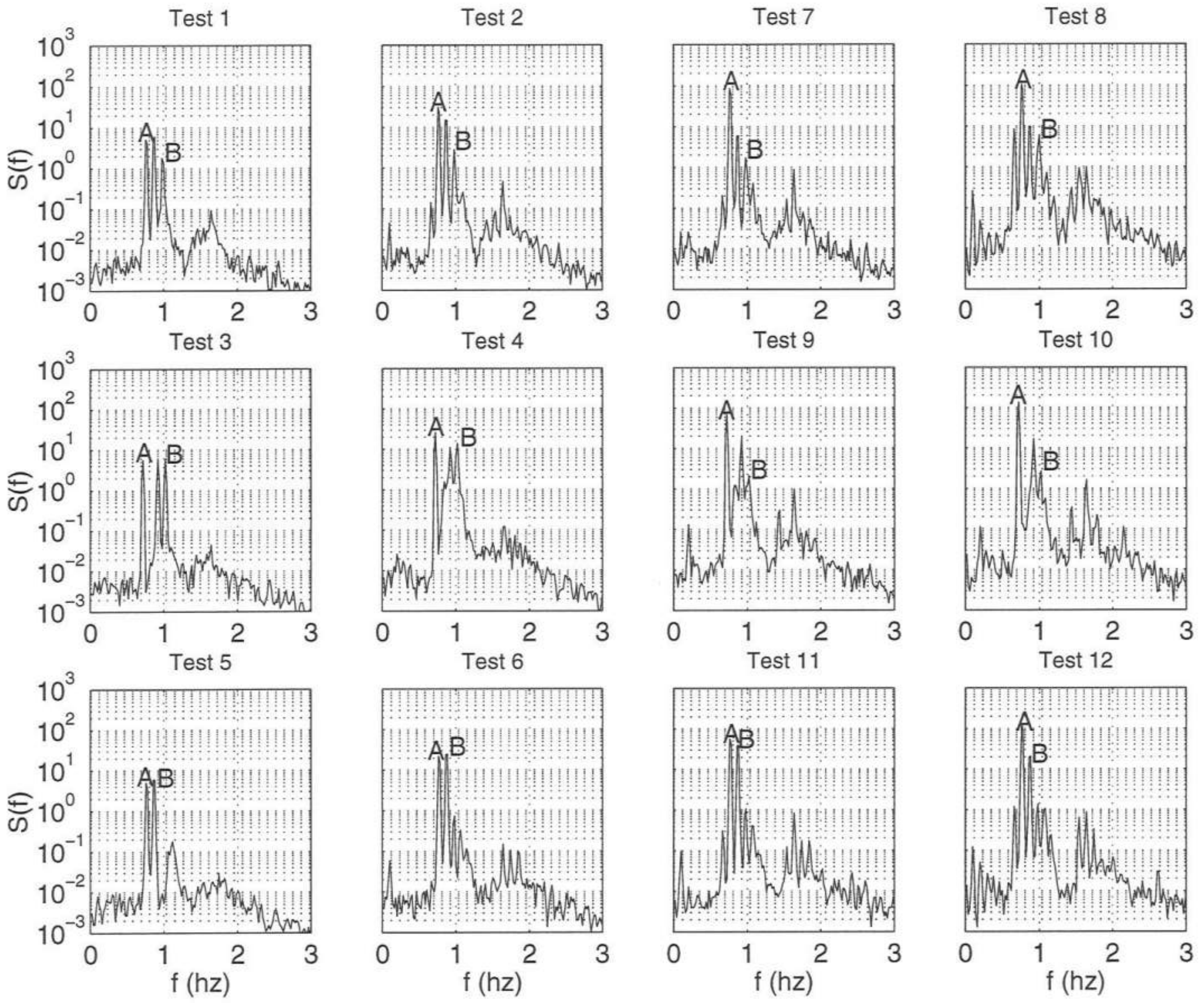

Figure 4.1: Frequency spectra at $x = -4.6$ m for wave group tests. The input waves are labeled by **A** and **B**.

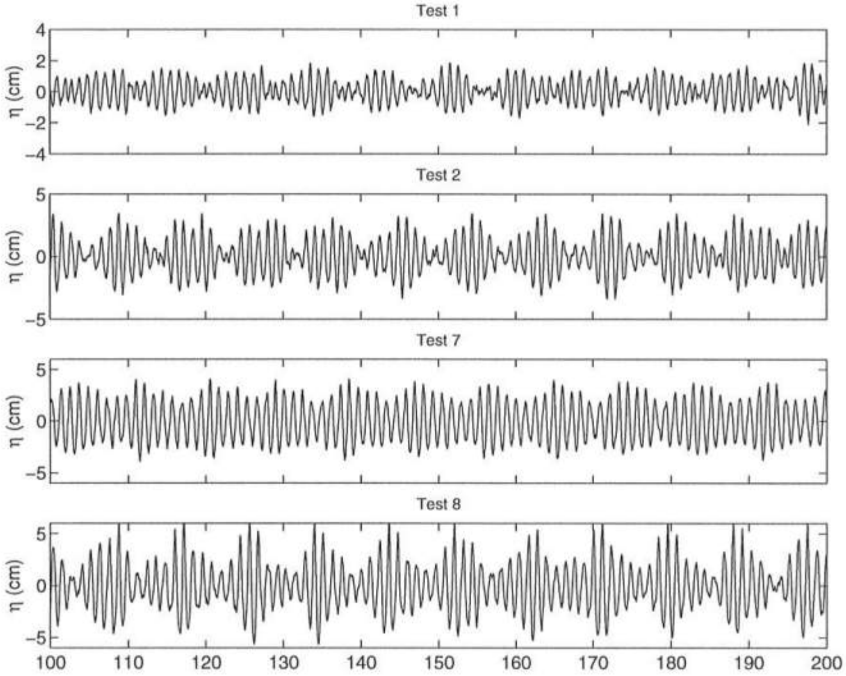

Figure 4.2: Time series at $x = -4.6$ m for Tests $1, 2, 7, 8$ (wave group tests)

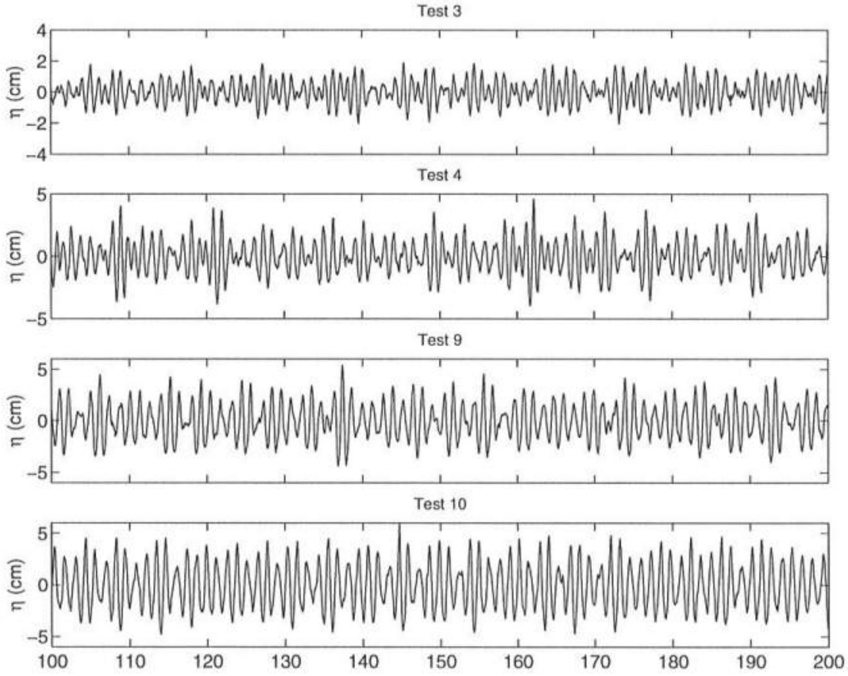

Figure 4.3: Time series at $x = -4.6$ m for Tests $3, 4, 9, 10$ (wave group tests)

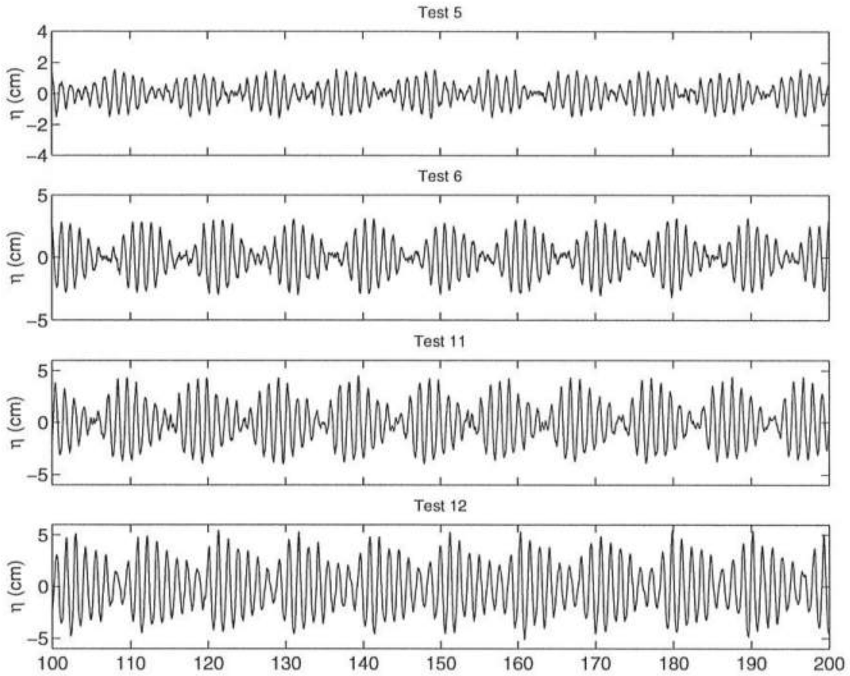

Figure 4.4: Time series at $x = -4.6$ m for Tests 5, 6, 11, 12 (wave group tests)

groups through the blocking region for this case is shown in Figures 4.5 and 4.6. The figures show the time series at 12 different locations in the channel. As the waves propagate into stronger currents the groups become asymmetrical and the waves are transformed from being groupy to being monochromatic to finally being blocked. The corresponding spectral plots (Figures 4.7 and 4.8) show that the two wave components are blocked at their respective blocking points. There is very little interaction and no long waves are generated downstream of the blocking point. Similar results were also observed by Chen *et al.* (1998) in their numerical simulations.

4.3 Wave packets

Wave packets have been generated with the help of Gaussian shaped frequency spectra. For our experiments 12 design test conditions were generated. As in

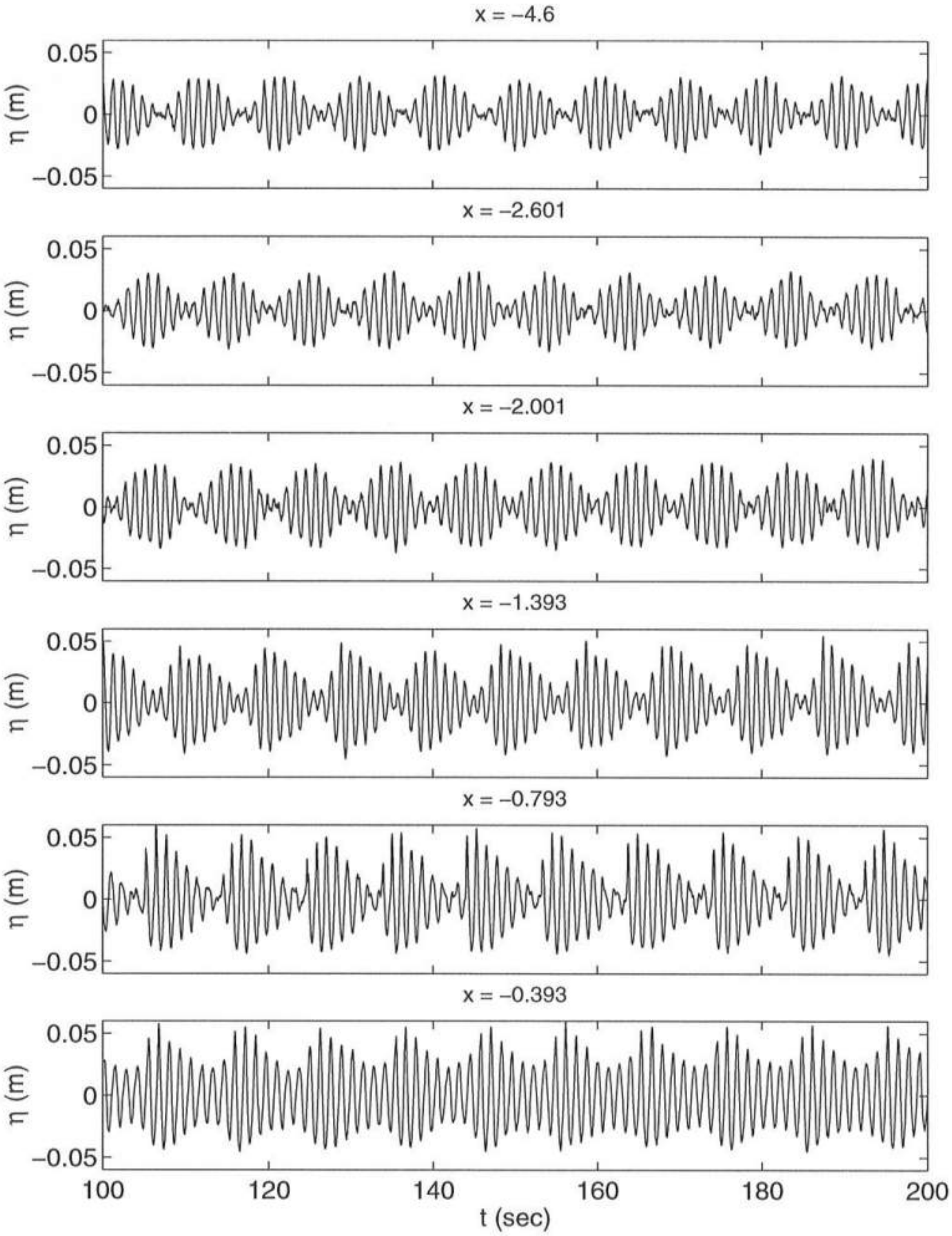

Figure 4.5: Time series of the wave groups at six different locations in the channel (Test 6)

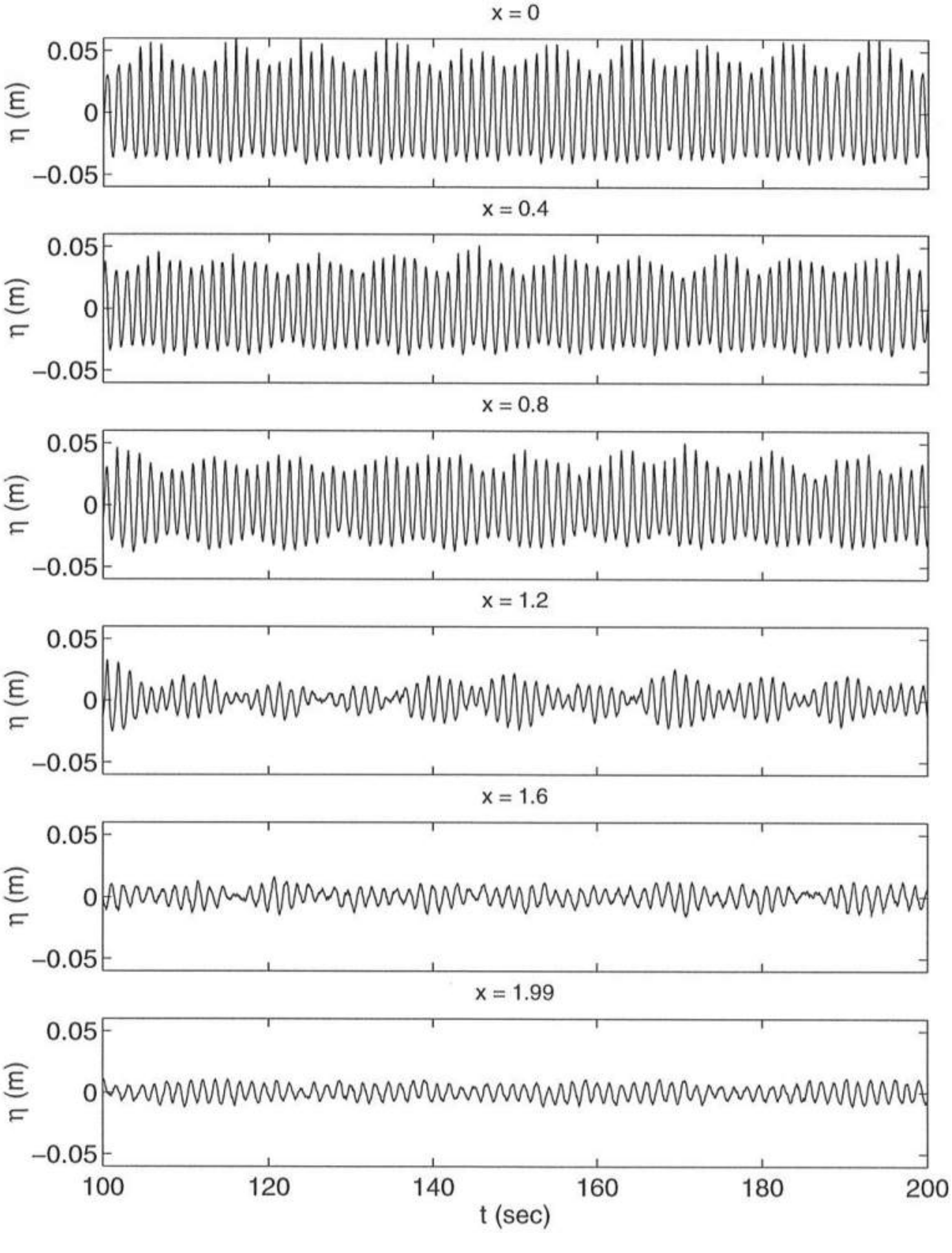

Figure 4.6: Time series of the wave groups at six different locations in the channel (Test 6)

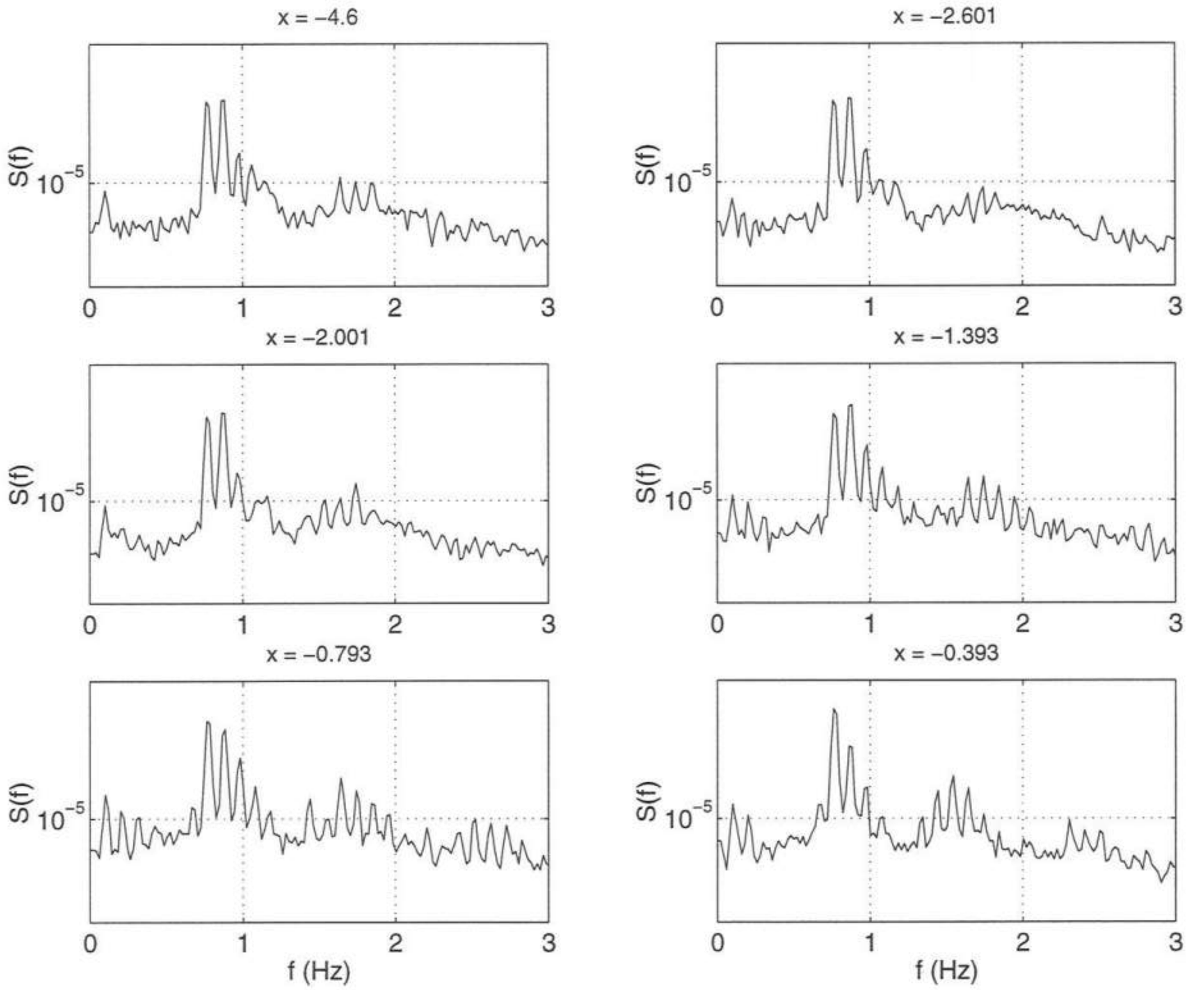

Figure 4.7: Frequency spectra corresponding to the six time series shown in Figure 4.5 (Test 6)

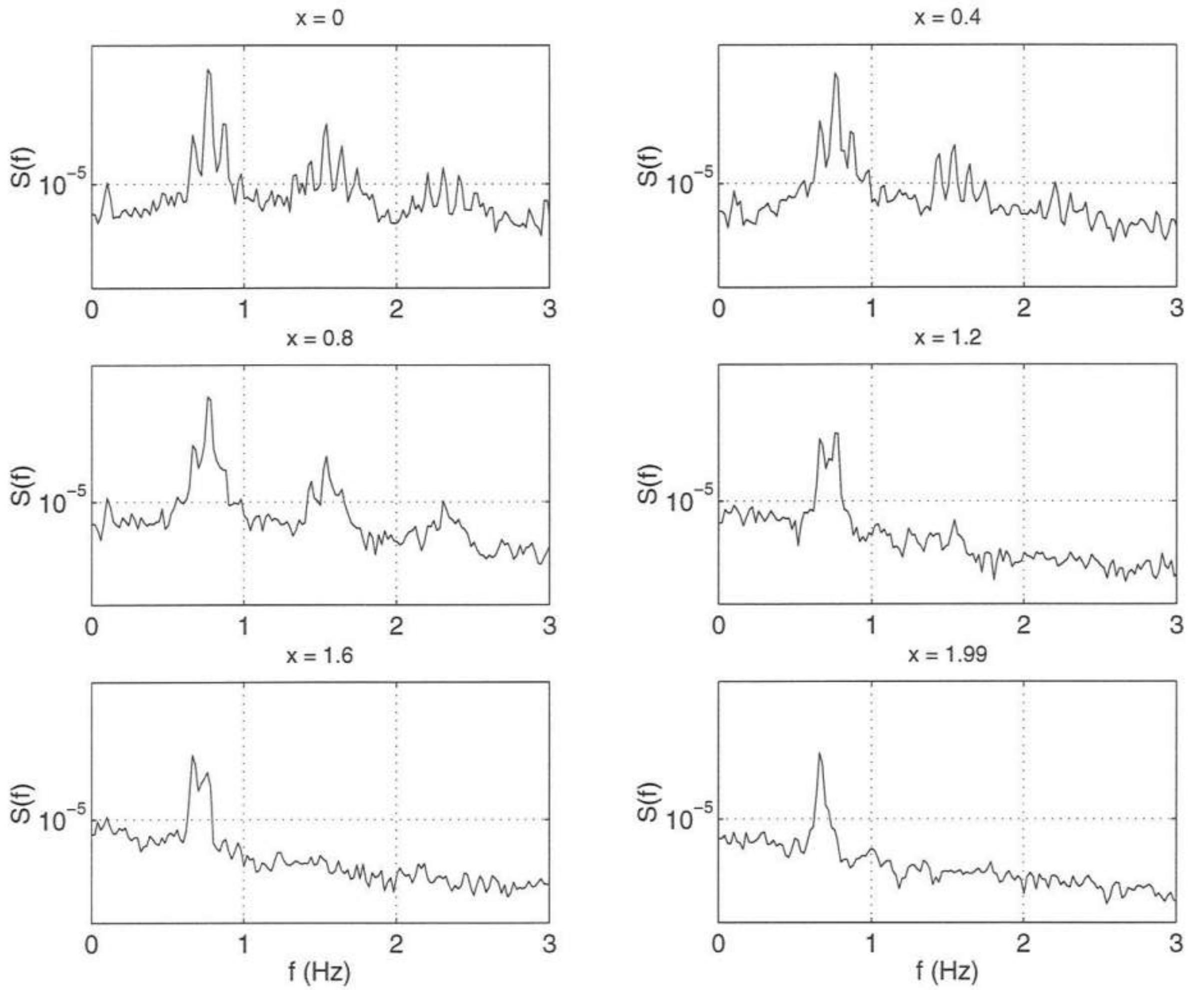

Figure 4.8: Frequency spectra corresponding to the six time series shown in Figure 4.6 (Test 6)

the case of the wave group tests, these tests have been divided into 3 sets. Each set consisting of 4 different test conditions with varying energy content. The equation for the design spectra was given by

$$S(f) = \frac{\gamma}{\sqrt{2\pi}\alpha} \exp\bigl(-0.5\frac{(f - f_p)^2}{\alpha^2}\bigr) \tag{4.1}$$

where, f_p is the peak frequency, and γ and α are coefficients determining the energy content and width of the spectrum. The larger the value of α, the lesser the number of individual wave components in the packet.

The time series of the wave paddle motion for the 12 cases are shown in Figures 4.9 to 4.11, where the tests with similar forms have been grouped together. The tests were designed such that they are similar to the corresponding wave group tests. By the time the wave packet reached the first gage ($x = -4.6$ m), the packet had diffused out, leading to much smaller wave heights (see Figures 4.12 to 4.14). This is specially true for Test 3, where the signature of the wave packet has been all but lost in the noise of the water surface. The test particulars for the wave packet tests are given in Table 4.2. H_{max} is the maximum wave height in the wave packet. T_p is the peak period and α is the parameter used in (4.1).

Similar to the wave group tests, test 6 consists of a relatively clean packet and the evolution of this packet in space is shown in Figures 4.15 and 4.16. At the blocking point the energy from the wave packet is reflected back and further away from the blocking point ($x = -2$ m) it is easy to distinguish the incident wave packet from the reflected packet. Closer to the blocking point the incident and reflected wave packets interact with each other and very close to the blocking point it becomes very difficult to distinguish between the two. The corresponding spectral plots (Figures 4.17 and 4.18) show that no long waves are generated in the wave packet tests either.

Table 4.2: Parameters for wave packet tests determined at $x = -4.6$ m

Test No.	T_p (s)	H_{max} (m)	α
1	1.125	0.0175	0.08
2	1.125	0.035	0.08
7	1.125	0.07	0.08
8	1.125	0.094	0.08
3	1.137	0.013	0.15
4	1.137	0.02	0.15
9	1.137	0.031	0.15
10	1.137	0.05	0.15
5	1.219	0.017	0.08
6	1.219	0.032	0.08
11	1.219	0.054	0.08
12	1.219	0.084	0.08

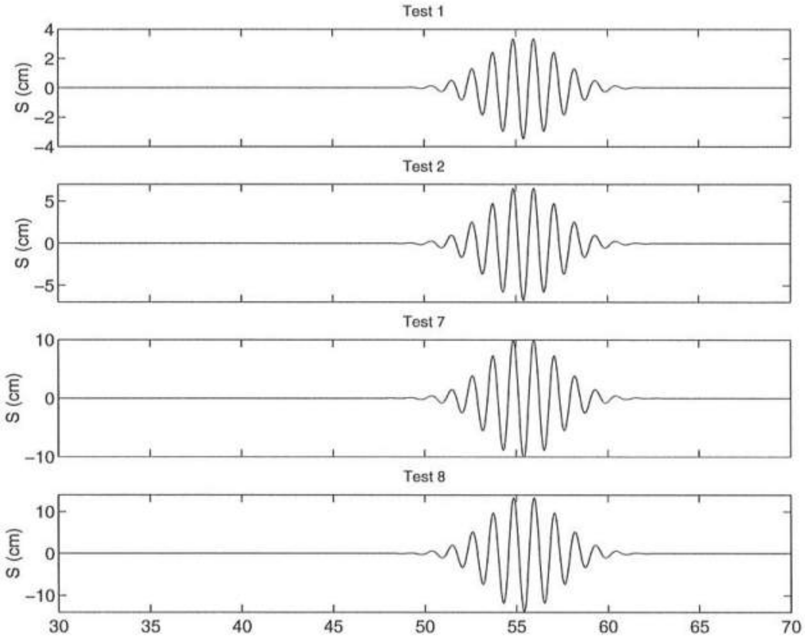

Figure 4.9: Time series of the wave paddle motion for Tests 1, 2, 7, 8 (wave packet tests)

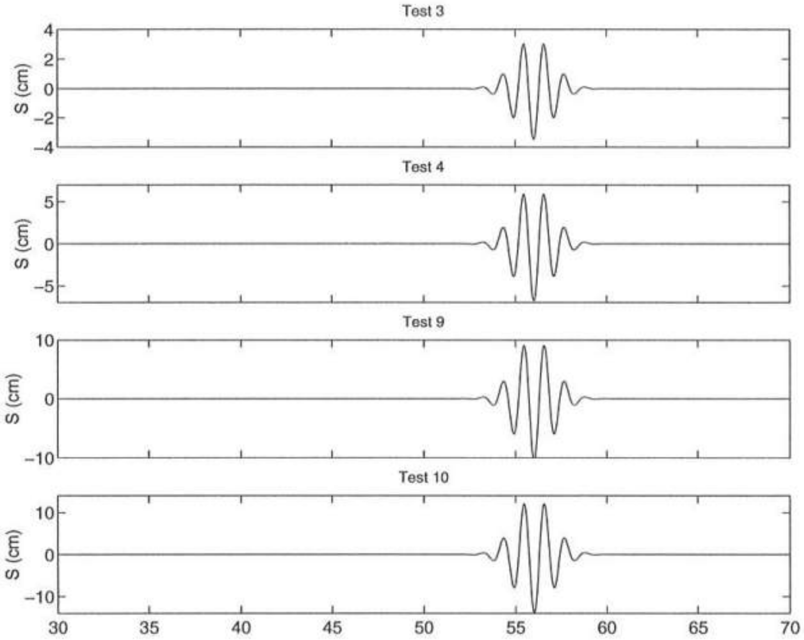

Figure 4.10: Time series of the wave paddle motion for Tests 3, 4, 9, 10 (wave packet tests)

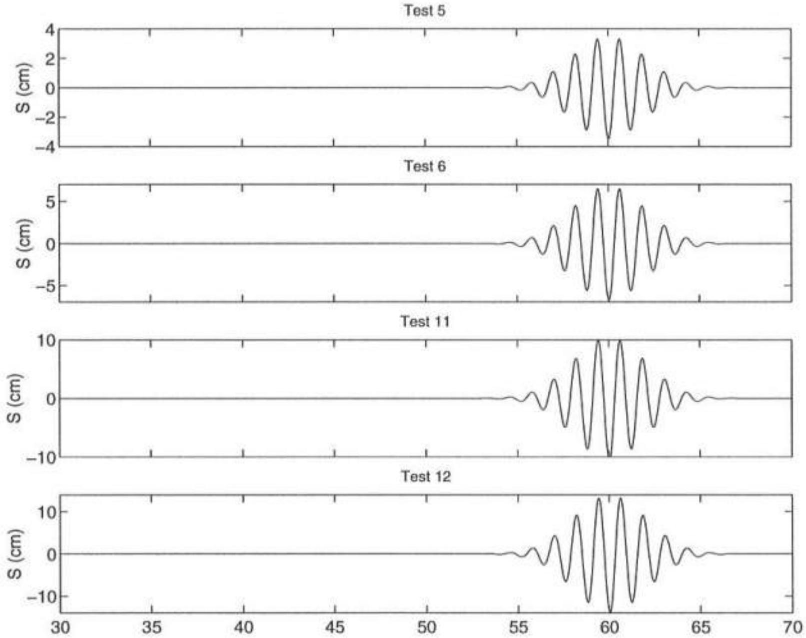

Figure 4.11: Time series of the wave paddle motion for Tests 5, 6, 11, 12 (wave packet tests)

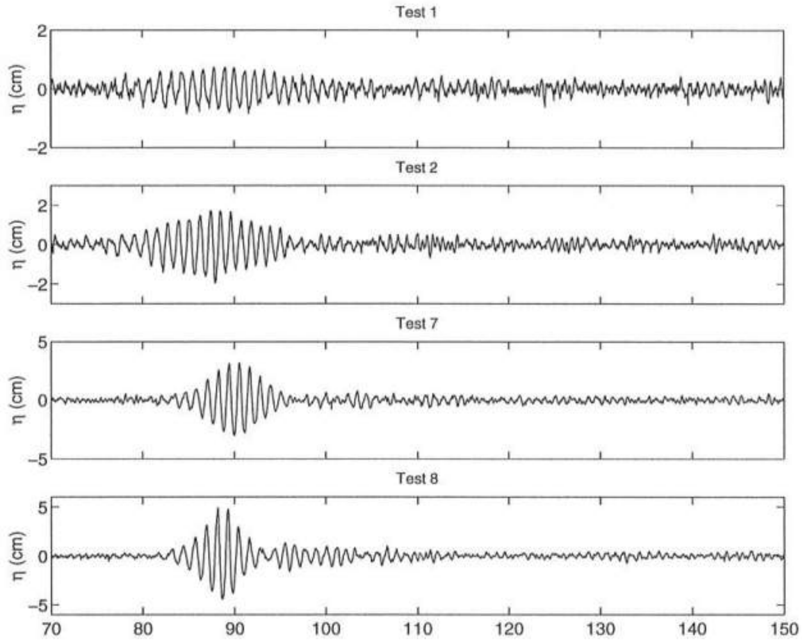

Figure 4.12: Time series of the water surface at $x = -4.6$ m for Tests $1, 2, 7, 8$ (wave packet tests)

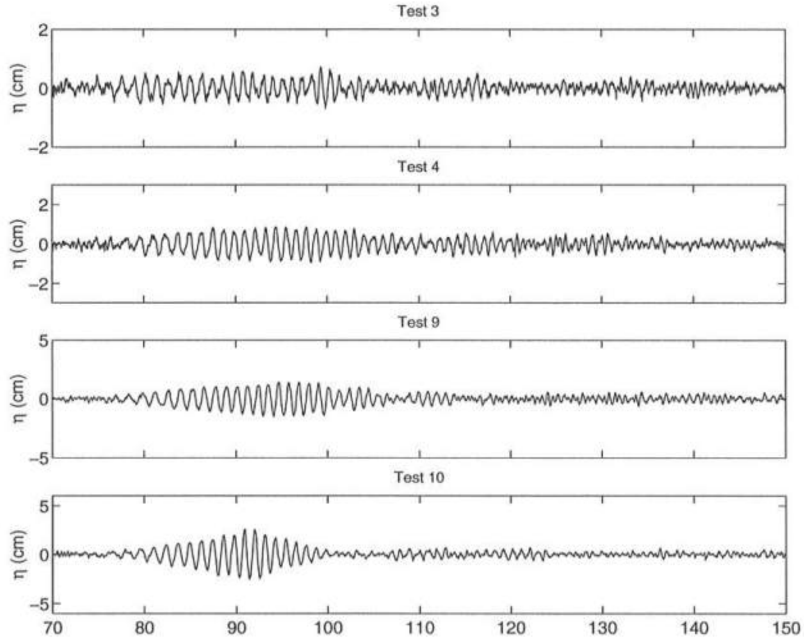

Figure 4.13: Time series of the water surface at $x = -4.6$ m for Tests $3, 4, 9, 10$ (wave packet tests)

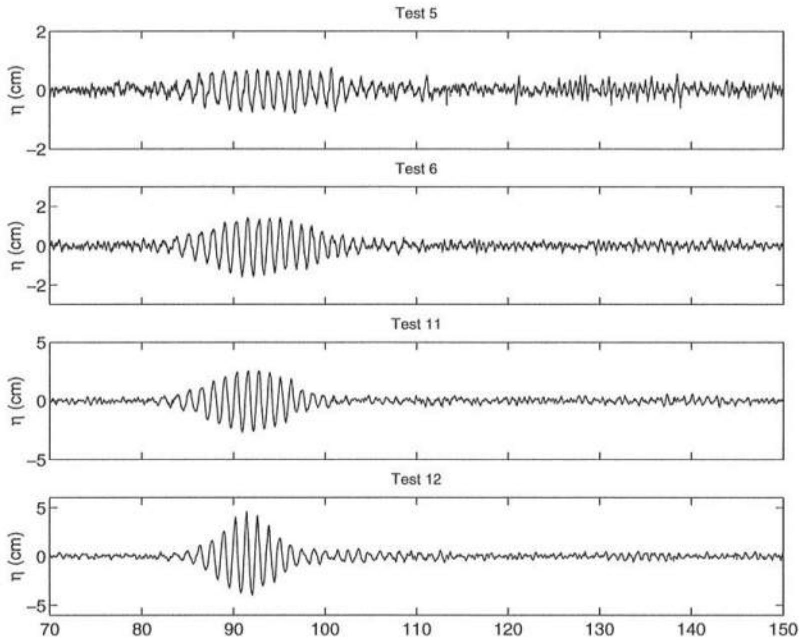

Figure 4.14: Time series of the water surface at $x = -4.6$ m for Tests $5, 6, 11, 12$ (wave packet tests)

4.4 Summary

A series of experimental tests were conducted on the evolution of wave groups and wave packets through the blocking region. The aim was to see if analogous to a moving breaking point in shallow water, a moving blocking point could act as a forcing mechanism for the generation of long waves downstream of the blocking points. Our test results indicate that this is not the case. The individual wave components in the wave groups get blocked at their respective blocking points with little interaction, and the waves evolve from being groupy to being monochromatic. Similar results were also observed in the numerical simulations of Chen *et al.* (1998). Reflection of the wave packets from the blocking point was observed in the wave packet data. Detailed plots of the narrow banded spectral tests are available in Chawla and Kirby (1999a).

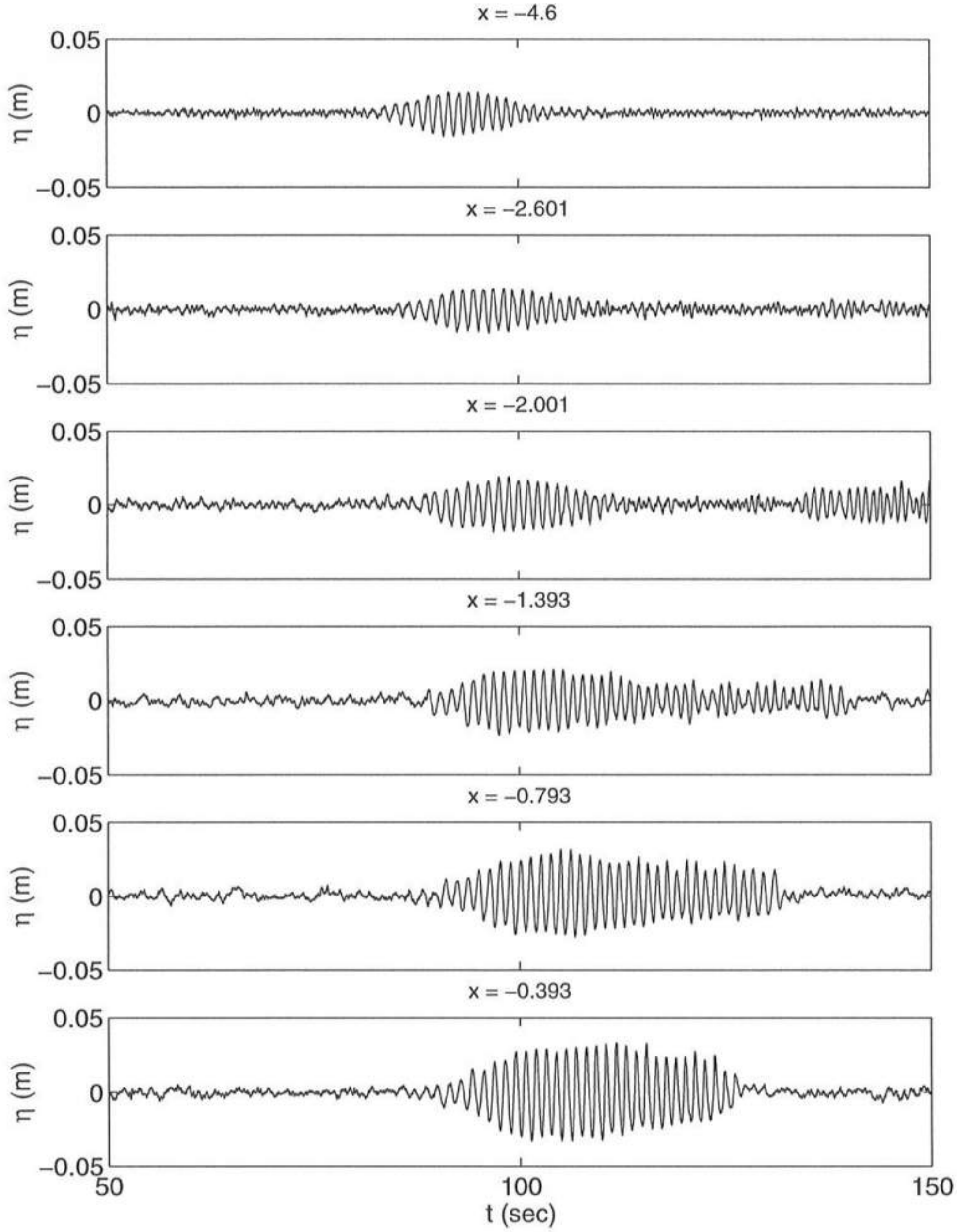

Figure 4.15: Time series of the wave packet at six different locations in the channel (Test 6)

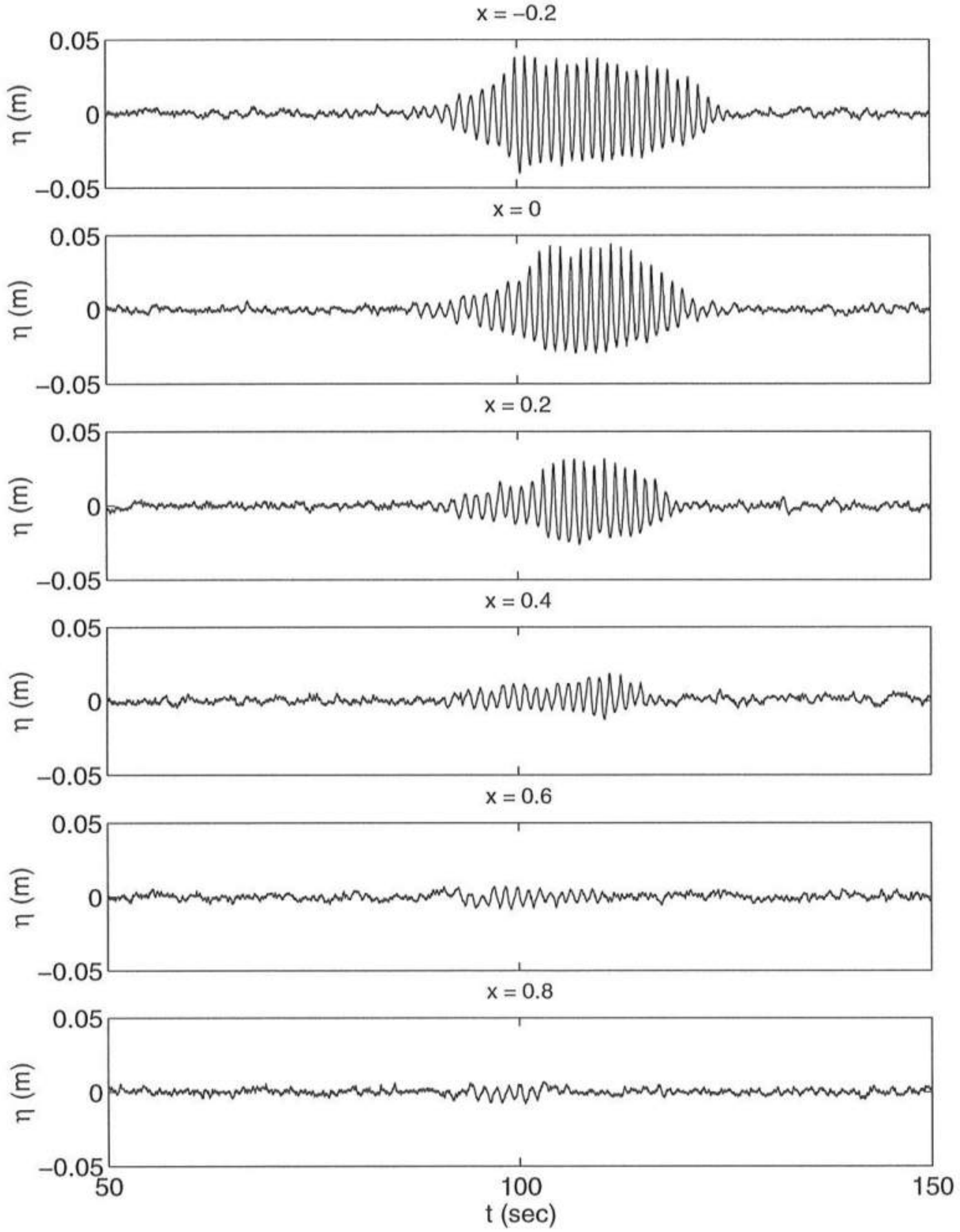

Figure 4.16: Time series of the wave packet at six different locations in the channel (Test 6)

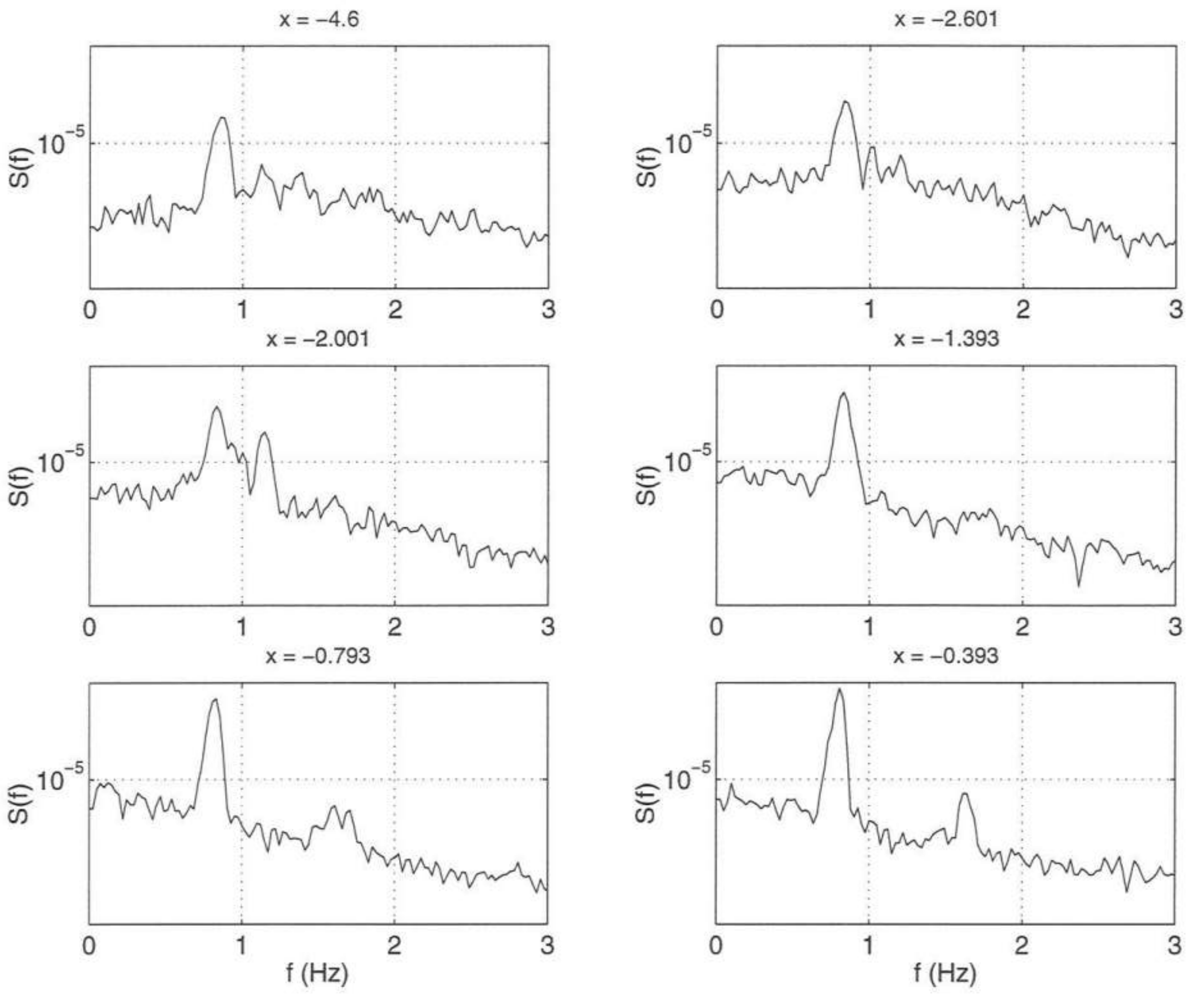

Figure 4.17: Frequency spectra corresponding to the six time series shown in Figure 4.15

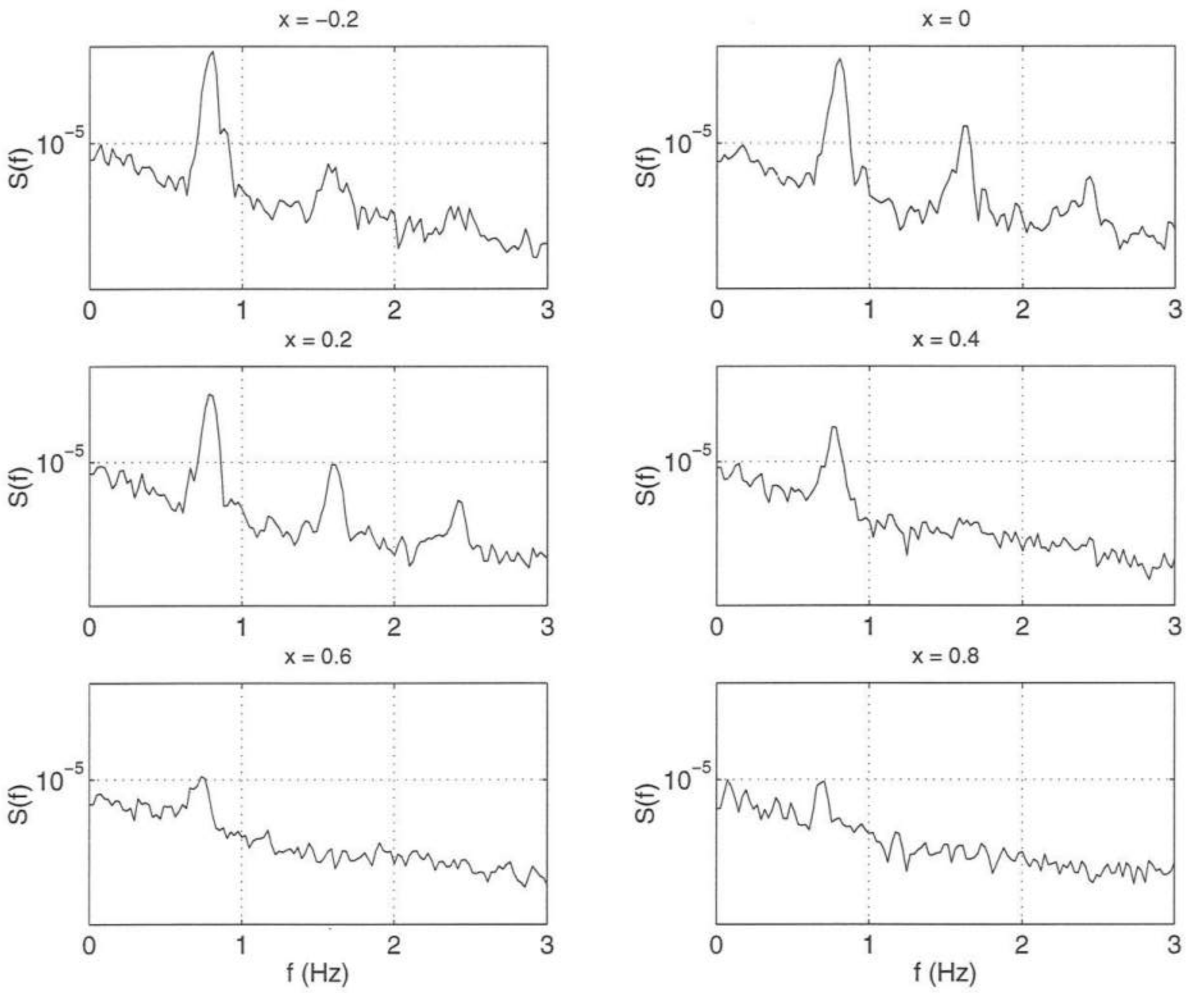

Figure 4.18: Frequency spectra corresponding to the six time series shown in Figure 4.16

Chapter 5

WEAKLY NON-LINEAR EVOLUTION EQUATION FOR NARROW-BANDED WAVES PROPAGATING IN STRONG CURRENTS

5.1 Introduction

Benjamin and Feir (1967) in their pioneering work showed both theoretically and experimentally that deep water waves with a carrier frequency f are unstable to side band perturbations at $f \pm \Delta f$. They conducted an instability analysis on Euler's equations and showed that the growth rate of these perturbations is directly dependent on the steepness of the waves. This sparked a great interest in the long term temporal and spatial evolution of deep water waves and wave packets, and a good review on the subject has been given by Yuen and Lake (1980).

Whitham (1965) deduced the basic governing equations for the slow modulation of wave amplitude, wave number, etc. Chu and Mei (1970, 1971) using a WKB-perturbation technique extended the scope of Whitham's theory by including new terms which directly represented the modulation rates. The evolution of these instabilities were found to be governed by the Schrödinger equation separately by Zakharov (1968), Hasimoto and Ono (1972) and Davey (1972). Permanent form solutions of the Schrödinger equation in the form of envelope solitons were predicted by Zakharov and Shabat (1972) who solved the equation directly using the inverse scattering technique of Gardner *et al.* (1967). Yuen and Lake (1975) derived the non-linear Schrödinger equation using Whitham's theory by carrying out the averaged variational principle to a higher order, and thus showed that the two different methods used to study the evolution of the side bands were in fact the same. They also verified the solutions obtained by Zakharov and Shabat (1972) with the help of experimental studies. Their experiments showed a recurrence pattern which was confirmed by Lake *et al.* (1977) and Yuen and Ferguson (1978). Though the recurrence of a monochromatic wave was predicted by the non-linear Schrödinger model, the experiments of Lake *et al.* (1977) showed that the recurrence is accompanied by a decrease in the frequency, which could not be predicted by the non-linear equation. Lo and Mei (1985) carried out the analysis to a higher order in non-linearity and showed that the growth in the energy of the side bands was unequal with the lower side band growing much faster. However, even in their numerical simulations recurrence occurred with no apparent shift in the frequency. Based on the experimental studies of Melville (1983), Trulsen and Dsythe (1990) showed that the down-shift occurs due to wave breaking at the steepest waves. Combining the model of Lo and Mei (1985) with a damping term to simulate energy dissipation, they showed that this was a possible mechanism for the down shift, though they were unable to recover a clean monochromatic wave.

Studies on side band instabilities in the presence of currents were carried out by Turpin *et al.* (1983) and Gerber (1987). They showed that these instabilities are highly pronounced in the case of an opposing current due to the rapid steepening of the waves. This increase in the growth rate of the side bands has been observed in the experiments carried out by Lai *et al.* (1989) and in our own experiments as well. Our experimental studies indicate that the evolution of side bands through the blocking region can adversely affect the dynamics of the wave field beyond the blocking point. The earlier models have been developed by considering perturbations on a carrier wave that is moving with the group velocity. But at the blocking point this carrier wave gets blocked, and the evolution of the side bands cannot be predicted any further into the domain.

A non-linear model for wave evolution needs to be developed that is valid in the domain beyond the blocking point. We have seen from our graphical solution in Figure 1.4 that, in the presence of currents, the dispersion relation has two roots (denoted by **B** and **C** in the figure). As the current increases the two roots move towards each other and beyond the blocking point there are no solutions of the dispersion relation. In fact there are solutions but they are in the complex domain. This can be seen from the linear dispersion relation for waves and currents in deep water.

$$(\omega - kU)^2 = gk$$

Solving the quadratic equation in k we get

$$k = \frac{2U\omega + g \pm g\sqrt{1 + \dfrac{4U\omega}{g}}}{2U^2}$$

k becomes complex for $U < -\dfrac{g}{4\omega}$. Figure 5.1 shows how the real and imaginary roots of the dispersion relation vary with the current. Beyond the blocking point two complex conjugate solutions are obtained. This leads to a complex phase function. The water surface motion η is given by

$$\eta \sim e^{i\psi}$$

where ψ is the phase. For a complex phase the wave changes from a sinusoidal form to an exponential form, and a decaying solution can be obtained by using the appropriate root.

A numerical model has thus been developed which accounts for blocking effects by allowing the phase to be complex. The model is one-dimensional in space

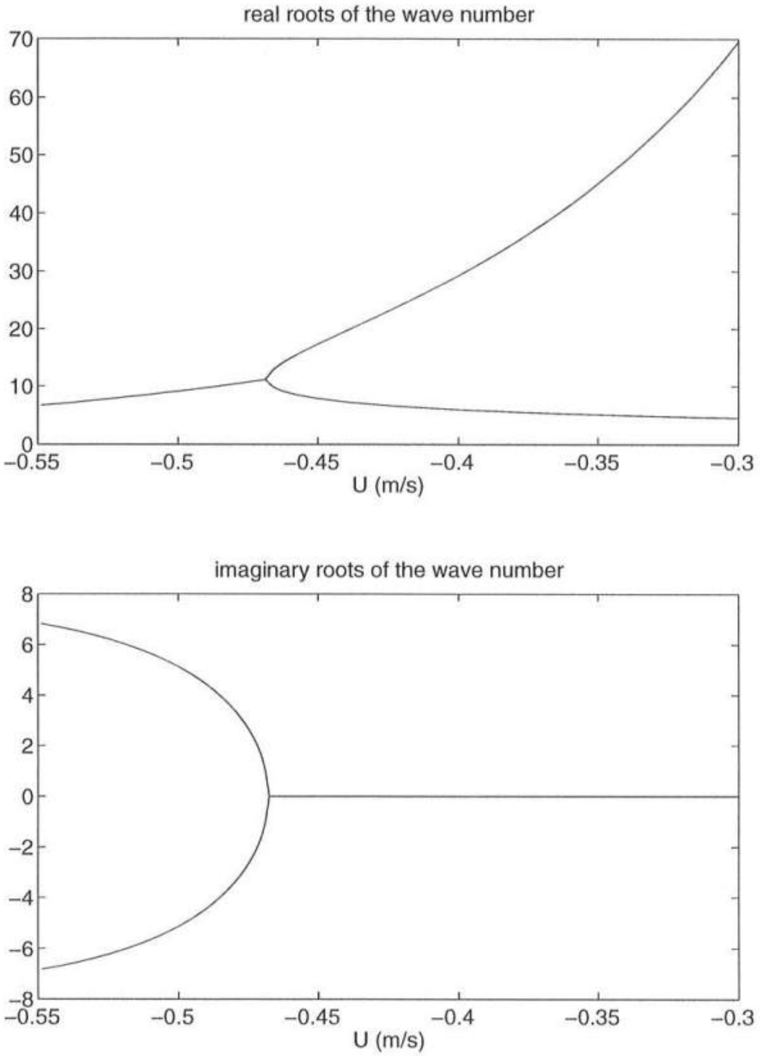

real roots of the wave number

imaginary roots of the wave number

Figure 5.1: real and imaginary roots of the Doppler shifted linear dispersion relation as a function of U (T = 1.2 s)

and has been developed for narrow channels with varying width. The orientation of the coordinate system is chosen such that the $x-$ axis lies along the channel centerline, the $y-$ axis is in the cross channel direction and the $z-$ axis points in the vertical direction. The short wave motion is in the positive x direction, while the underlying steady depth uniform current is in the opposite direction.

5.2 Boundary value problem

The boundary value problem for irrotational fluid flow in terms of a velocity potential $\acute{\Phi}$ is given by

$$\acute{\Phi}_{\acute{x}\acute{x}} + \acute{\Phi}_{\acute{y}\acute{y}} + \acute{\Phi}_{\acute{z}\acute{z}} = 0; \quad -\acute{h} \leq \acute{z} \leq \acute{\eta} \tag{5.1a}$$

$$\acute{\Phi}_{\acute{z}} + \acute{h}_{\acute{x}}\acute{\Phi}_{\acute{x}} + \acute{h}_{\acute{y}}\acute{\Phi}_{\acute{y}} = 0; \quad \acute{z} = -\acute{h} \tag{5.1b}$$

$$\acute{\eta} = -\frac{\acute{\Phi}_{\acute{t}}}{g} - \frac{1}{2g}\left(\acute{\Phi}_{\acute{x}}^2 + \acute{\Phi}_{\acute{y}}^2 + \acute{\Phi}_{\acute{z}}^2\right); \quad \acute{z} = \acute{\eta} \tag{5.1c}$$

$$\begin{aligned} &\acute{\Phi}_{\acute{t}\acute{t}} + g\acute{\Phi}_{\acute{z}} + \left(\acute{\Phi}_{\acute{x}}^2 + \acute{\Phi}_{\acute{y}}^2 + \acute{\Phi}_{\acute{z}}^2\right)_{\acute{t}} \\ &+ \frac{1}{2}\left\{\acute{\Phi}_{\acute{x}}\frac{\partial}{\partial \acute{x}} + \acute{\Phi}_{\acute{y}}\frac{\partial}{\partial \acute{y}} + \acute{\Phi}_{\acute{z}}\frac{\partial}{\partial \acute{z}}\right\}\left(\acute{\Phi}_{\acute{x}}^2 + \acute{\Phi}_{\acute{y}}^2 + \acute{\Phi}_{\acute{z}}^2\right) = 0; \quad \acute{z} = \acute{\eta} \end{aligned} \tag{5.1d}$$

$$\acute{\Phi}_{\acute{y}} = \pm\acute{b}_{\acute{x}}\acute{\Phi}_{\acute{x}}; \quad \acute{y} = \pm\acute{b} \tag{5.1e}$$

where $2\acute{b}$ is the channel width and $\acute{\eta}$ is the surface displacement due to the combined effect of current and waves.

We now nondimensionalize the problem using the following scaling

$$\begin{array}{cc} \eta = \dfrac{\acute{\eta}}{a}; & \Phi = \dfrac{\epsilon k_0^2}{\sqrt{g k_0}}\acute{\Phi} \\ t = \sqrt{g k_0}\,\acute{t}; & (x, y, z, h, b) = k_0(\acute{x}, \acute{y}, \acute{z}, \acute{h}, \acute{b}) \end{array} \tag{5.2}$$

where a is the measure of wave amplitude, k_0 is the measure of wave number and $\epsilon = k_0 a$ is a nonlinearity parameter.

The resulting B.V.P. is given by

$$\Phi_{xx} + \Phi_{yy} + \Phi_{zz} = 0; \quad -h \le z \le \epsilon\eta \tag{5.3a}$$

$$\Phi_z + h_x\Phi_x + h_y\Phi_y = 0; \quad z = -h \tag{5.3b}$$

$$\eta = -\Phi_t - \frac{\epsilon}{2}\Big(\Phi_x^2 + \Phi_y^2 + \Phi_z^2\Big); \quad z = \epsilon\eta \tag{5.3c}$$

$$\begin{aligned}&\Phi_{tt} + \Phi_z + \epsilon\Big(\Phi_x^2 + \Phi_y^2 + \Phi_z^2\Big)_t \\ &+ \frac{\epsilon^2}{2}\left\{\Phi_x\frac{\partial}{\partial x} + \Phi_y\frac{\partial}{\partial y} + \Phi_z\frac{\partial}{\partial z}\right\}\Big(\Phi_x^2 + \Phi_y^2 + \Phi_z^2\Big) = 0; \quad z = \epsilon\eta\end{aligned} \tag{5.3d}$$

$$\Phi_y = \pm b_x\Phi_x; \quad y = \pm b \tag{5.3e}$$

Since the waves are propagating in the positive x direction, we have a fast scale in x and t over which the phase of wave motion changes and a slower scale over which the wavenumber and wave amplitude changes. Across the channel there are no fast scales. Using stretched coordinates we thus have

$$x = x + \frac{X_1}{\epsilon} + \frac{X_2}{\epsilon^2} + \cdots \tag{5.4a}$$

$$t = t + \frac{T_1}{\epsilon} + \frac{T_2}{\epsilon^2} + \cdots \tag{5.4b}$$

$$y = \frac{Y_1}{\epsilon} + \frac{Y_2}{\epsilon^2} + \cdots \tag{5.4c}$$

Furthermore, since we are studying the interactions between an $O(1)$ current and wave motion, we can write Φ and η as

$$\Phi = \Phi_c + \epsilon\Phi_w \tag{5.5a}$$

$$\eta = \eta_c + \epsilon\eta_w \tag{5.5b}$$

where the sub-scripts c and w correspond to current and wave motion respectively.

5.2.1 Solution for current motion

Assuming that the current is steady and uniform in depth, and that both the channel geometry and depth averaged current U are a function of the slow coordinate X_2, we can write Φ_c as

$$\Phi_c = \frac{1}{\epsilon^2}\int U(X_2)dX_2 + \tilde{\Phi}_c(X_2, Y_1, Y_2, z) \tag{5.6}$$

The resulting boundary value problem for current motion in the stretched coordinate system is then given by

$$\epsilon^2 U_{X_2} + \epsilon^2\tilde{\Phi}_{c_{Y_1Y_1}} + \tilde{\Phi}_{c_{zz}} = 0; \quad -h \le z \le \eta_c \tag{5.7a}$$

$$\tilde{\Phi}_{c_z} = -\epsilon^2 U h_{X_2}; \quad z = -h \tag{5.7b}$$

$$\eta_c = -\frac{1}{2}\Big(U^2 + \epsilon^2(\tilde{\Phi}_{c_{Y_1}})^2 + (\tilde{\Phi}_{c_z})^2\Big); \quad z = \eta_c \tag{5.7c}$$

$$\epsilon^2\Big(\eta_{c_{X_2}}U + \eta_{c_{Y_1}}\tilde{\Phi}_{c_{Y_1}}\Big) = \tilde{\Phi}_{c_z}; \quad z = \eta_c \tag{5.7d}$$

$$\tilde{\Phi}_{c_{Y_1}} = \pm\epsilon b_{X_2}U; \quad Y_1 = \pm\epsilon b \tag{5.7e}$$

From the B.V.P. it is clear that the vertical velocity $\tilde{\Phi}_{c_z}$ is $O(\epsilon^2)$. We can thus write $\tilde{\Phi}_c$ as

$$\tilde{\Phi}_c = \tilde{\Phi}_{c1}\Big(X_2, Y_1, Y_2\Big) + \epsilon^2 \tilde{\Phi}_{c2}\Big(X_2, z\Big)$$

Substituting the above expression in (5.7) and solving the B.V.P. by first integrating out the Y_1 dependency using the lateral boundary conditions, we get

$$\tilde{\Phi}_{c1} = \frac{U b_{X_2}}{b} \frac{(Y_1)^2}{2} \tag{5.8a}$$

$$\tilde{\Phi}_{c2} = -\frac{(Ub)_{X_2}}{b} \frac{(z+h)^2}{2} - U h_{X_2} z \tag{5.8b}$$

and the combined expression for Φ_c is given by

$$\Phi_c = \frac{1}{\epsilon^2} \int U(X_2) dX_2 + \frac{U b_{X_2}}{b} \frac{(Y_1)^2}{2} - \epsilon^2 \Big(\frac{(Ub)_{X_2}}{b} \frac{(z+h)^2}{2} + U h_{X_2} z \Big) \tag{5.9}$$

From (5.9) it is clear that the horizontal velocity along the channel has variations in depth and across the channel. However, for our experimental setup these variations were less than 1%. Substituting (5.9) in the surface boundary conditions yields

$$\eta_c = -\frac{U^2(X_2)}{2} + O(\epsilon^4) \tag{5.10a}$$

$$(Ub(h+\eta_c))_{X_2} = O(\epsilon^4) \tag{5.10b}$$

5.2.2 Solution for the combined wave-current interaction

Substituting (5.5) in (5.3), doing a Taylor series expansion about the current surface $z = \eta_c$ and separating the B.V.P. for the steady current (eqn. 5.7), we get a resulting B.V.P. for the combined wave-current interaction

$$\Phi_{wxx} + \Phi_{wyy} + \Phi_{wzz} = 0; \quad -h \le z \le \epsilon\eta_w \tag{5.11a}$$

$$\Phi_{wz} + h_x \Phi_{wx} = 0; \quad z = -h \tag{5.11b}$$

$$\begin{aligned}\eta_w = &- \Phi_{wt} - \frac{\epsilon}{2}\Big((\frac{\Phi_{cx}}{\epsilon} + \Phi_{wx})^2 + (\frac{\Phi_{cy}}{\epsilon} + \Phi_{wy})^2 + (\frac{\Phi_{cz}}{\epsilon} + \Phi_{wz})^2\Big) \\ &+ \frac{1}{2\epsilon}\Big(\Phi_{cx}^{\,2} + \Phi_{cy}^{\,2} + \Phi_{cz}^{\,2}\Big); \quad z = \epsilon\eta_w\end{aligned} \tag{5.11c}$$

$$\begin{aligned}&\Phi_{wtt} + \Phi_{wz} + \eta_w \Phi_{c_{zz}+}\epsilon\Big((\frac{\Phi_{cx}}{\epsilon} + \Phi_{wx})^2 + (\frac{\Phi_{cy}}{\epsilon} + \Phi_{wy})^2 + (\frac{\Phi_{cz}}{\epsilon} + \Phi_{wz})^2\Big)_t \\ &+ \frac{\epsilon^2}{2}\left\{(\frac{\Phi_{cx}}{\epsilon} + \Phi_{wx})\frac{\partial}{\partial x} + (\frac{\Phi_{cy}}{\epsilon} + \Phi_{wy})\frac{\partial}{\partial y} + (\frac{\Phi_{cz}}{\epsilon} + \Phi_{wz})\frac{\partial}{\partial z}\right\} \\ &\Big((\frac{\Phi_{cx}}{\epsilon} + \Phi_{wx})^2 + (\frac{\Phi_{cy}}{\epsilon} + \Phi_{wy})^2 + (\frac{\Phi_{cz}}{\epsilon} + \Phi_{wz})^2\Big) - \\ &\frac{\epsilon^2}{2}\left\{\frac{\Phi_{cx}}{\epsilon}\frac{\partial}{\partial x} + \frac{\Phi_{cy}}{\epsilon}\frac{\partial}{\partial y} + \frac{\Phi_{cz}}{\epsilon}\frac{\partial}{\partial z}\right\}\Big((\frac{\Phi_{cx}}{\epsilon})^2 + (\frac{\Phi_{cy}}{\epsilon})^2 + (\frac{\Phi_{cz}}{\epsilon})^2\Big) = 0; \quad z = \epsilon\eta_w\end{aligned} \tag{5.11d}$$

$$\Phi_{wy} = \pm b_x \Phi_{wx}; \quad y = \pm b \tag{5.11e}$$

Substituting the stretched coordinates (5.4), the velocity potential for current (5.9) and perturbing the wave motion using the small parameter ϵ

$$\Phi_w = \Phi_1 + \epsilon\Phi_2 + \epsilon^2\Phi_3 \tag{5.12a}$$

$$\eta_w = \eta_1 + \epsilon\eta_2 + \epsilon^2\eta_3 \tag{5.12b}$$

the nonlinear B.V.P. can be reduced to a set of linear B.V.P.s at different orders of ϵ. For compactness the following definitions shall be used

$$D \equiv \frac{\partial}{\partial t} + U\frac{\partial}{\partial x} \tag{5.13a}$$

$$\Gamma \equiv D^2 + \frac{\partial}{\partial z} \tag{5.13b}$$

$$D_1 \equiv \frac{\partial}{\partial T_1} + U\frac{\partial}{\partial X_1} \tag{5.13c}$$

$$D_2 \equiv \frac{\partial}{\partial T_2} + U\frac{\partial}{\partial X_2} \tag{5.13d}$$

$$\nabla \equiv \left(\frac{\partial}{\partial x}, \frac{\partial}{\partial z}\right) \tag{5.13e}$$

and the corresponding B.V.P.s for the first three orders of ϵ are given by

$$\Phi_{nxx} + \Phi_{nzz} = F_n; \quad -h \leq z \leq 0, \quad n = 1, 2, 3 \tag{5.14a}$$

$$\Phi_{nz} = G_n; \quad z = -h, \quad n = 1, 2, 3 \tag{5.14b}$$

$$\eta_n = K_n; \quad z = \eta_c, \quad n = 1, 2, 3 \tag{5.14c}$$

$$\Gamma\Phi_n = J_n; \quad z = \eta_c, \quad n = 1, 2, 3 \tag{5.14d}$$

$$\Phi_{nY_1} = H_n; \quad Y_1 = \pm\epsilon b, \quad n = 1, 2 \tag{5.14e}$$

where the forcing terms are given by

$$F_1 = 0 \tag{5.15a}$$

$$F_2 = -2\Phi_{1xX_1} \tag{5.15b}$$

$$F_3 = -\left(\Phi_{1X_1X_1} + \Phi_{1Y_1Y_1}\right) - \left(\Phi_{1xX_2} + \Phi_{1X_2x}\right) - 2\Phi_{2xX_1} \tag{5.15c}$$

$$G_1 = 0 \tag{5.16a}$$

$$G_2 = 0 \tag{5.16b}$$

$$G_3 = -h_{X_2}\Phi_{1x} \tag{5.16c}$$

$$H_1 = 0 \tag{5.17a}$$

$$H_2 = \pm b_{X_2}\Phi_{1x} \tag{5.17b}$$

$$K_1 = -D\Phi_1 \tag{5.18a}$$

$$K_2 = -D\Phi_2 - D_1\Phi_1 - \frac{1}{2}\big(\nabla\Phi_1 \cdot \nabla\Phi_1\big) - \eta_1 D\Phi_{1z} \tag{5.18b}$$

$$\begin{aligned} K_3 = &- D\Phi_3 - D_1\Phi_2 - D_2\Phi_1 - \eta_1\Big(D_1\Phi_{1z} + D\Phi_{2z} + \frac{1}{2}\big(\nabla\Phi_1 \cdot \nabla\Phi_1\big)_z\Big) \\ &- \eta_2 D\Phi_{1z} - \frac{\eta_1^2}{2}D\Phi_{1zz} - \Big(\Phi_{1x}\Phi_{1X_1} + \Phi_{1x}\Phi_{2x} + \Phi_{1z}\Phi_{2z}\Big) - U\frac{b_{X_2}}{b}Y_1\Phi_{1Y_1} \\ &+ U\eta_{c_{X_2}} \end{aligned} \tag{5.18c}$$

$$J_1 = 0 \tag{5.19a}$$

$$J_2 = -2DD_1\Phi_1 - D\big(\nabla\Phi_1 \cdot \nabla\Phi_1\big) - \eta_1\Gamma\Phi_{1z} \tag{5.19b}$$

$$\begin{aligned} J_3 = &- 2U\frac{b_{X_2}}{b}Y_1 D\Phi_{1Y_1} + \eta_1\frac{(Ub)_{X_2}}{b} - D_2 D\Phi_1 - DD_2\Phi_1 - D_1^2\Phi_1 + \eta_{c_{X_2}}\Phi_{1x} \\ &- 2DD_1\Phi_2 - D_1\big(\nabla\Phi_1 \cdot \nabla\Phi_1\big) - 2D\Big(\Phi_{1x}\Phi_{1X_1} + \Phi_{1x}\Phi_{2x} + \Phi_{1z}\Phi_{2z}\Big) \\ &- \frac{1}{2}\nabla\Phi_1 \cdot \nabla\big(\nabla\Phi_1 \cdot \nabla\Phi_1\big) - \eta_1\Big(2DD_1\Phi_1 + \Gamma\Phi_2 + D\big(\nabla\Phi_1 \cdot \nabla\Phi_1\big)\Big)_z \\ &- \eta_2\Gamma\Phi_{1z} - \frac{\eta_1^2}{2}\Gamma\Phi_{1zz} \end{aligned} \tag{5.19c}$$

The first order solution of (5.14) is the linear solution for a propagating wave. Due to the presence of nonlinear forcing terms at higher orders in the surface boundary conditions, we expand the velocity potential using a WKB expansion

$$\Phi_n = \Phi_{n,0} + \Big(\sum_{m=1}^{m=n} \Phi_{n,m} e^{im\psi} + c.c.\Big) \tag{5.20}$$

where $c.c.$ is the complex conjugate and ψ is the phase function given by

$$\psi = \int (k(X_2)dx - \omega dt) \tag{5.21}$$

Thus

$$k = \psi_x \quad ; \quad \omega = -\psi_t \tag{5.22}$$

ω remains constant through the domain but k varies with the current and beyond the blocking point k becomes complex. The solution thus changes from a propagating wave form to an exponentially decaying one. Therefore, to propagate the solution through the blocking region, the phase function ψ is allowed to be complex. The forcing terms in the boundary value problem are also expanded using the WKB expansion. Substituting the expansion in (5.14) we get

$$\left(\frac{\partial^2}{\partial z^2} - m^2k^2\right)\Phi_{n,m} = F_{n,m}; \quad -h \le z \le 0 \tag{5.23a}$$

$$\Phi_{n,m_z} = G_{n,m}; \quad z = -h \tag{5.23b}$$

$$\Phi_{n,m_{Y_1}} = G_{n,m}; \quad y = \pm b \tag{5.23c}$$

$$\left(\frac{\partial}{\partial z} - m^2\sigma^2\right)\Phi_{n,m} = J_{n,m}; \quad z = \eta_c \tag{5.23d}$$

$$\eta_{n,m} = K_{n,m}; \quad z = \eta_c \tag{5.23e}$$

where

$$\sigma \equiv \omega - kU \tag{5.24}$$

Eqn (5.23) has to be solved sequentially for all m at a particular n before going to the next n level. For $n \geq 2$ there are two special cases.

$\underline{m = 0}$: The governing equation is given by

$$\Phi_{n,0_{zz}} = F_{n,0} \tag{5.25}$$

Integrating (5.25) in depth and using the boundary conditions we get

$$\int_{-h}^{\eta_c} F_{n,0} dz = J_{n,0} - G_{n,0} \tag{5.26}$$

$\underline{m = 1}$: The boundary value problem is given by

$$\left(\frac{\partial^2}{\partial z^2} - k^2 \right) \Phi_{n,1} = F_{n,1}; \quad -h \leq z \leq \eta_c \tag{5.27a}$$

$$\Phi_{n,1_z} = G_{n,1}; \quad z = -h \tag{5.27b}$$

$$\left(\frac{\partial}{\partial z} - \sigma^2 \right) \Phi_{n,1} = J_{n,1}; \quad z = \eta_c \tag{5.27c}$$

$$\eta_{n,1} = K_{n,1}; \quad z = \eta_c \tag{5.27d}$$

The homogeneous solution to (5.27) is a freely propagating wave governed by the linearized problem. To prevent secular terms, the inhomogeneous solution must satisfy a solvability condition which is given by

$$\int_{-h}^{\eta_c} \Phi_{1,1} F_{n,1} dz = \Phi_{1,1} J_{n,1}\Big|_{z=\eta_c} - \Phi_{1,1} G_{n,1}\Big|_{z=-h} \tag{5.28}$$

The two solvability conditions (5.26) and (5.28) yield the evolution equations for the wave amplitude and the corresponding long wave motion.

5.2.2.1 First order solution

The forcing terms at the lowest order are given by

$$F_1 = 0 \quad ; \quad G_1 = 0 \quad ; \quad J_1 = 0$$

At $m = 0$

$$\Phi_{1,0_z} = 0$$

Thus,

$$\Phi_{1,0} = \Phi_{1,0}(X_1, X_2, Y_1, Y_2, T_1, T_2, \cdots) \tag{5.29}$$

At $m = 1$ the boundary value problem is

$$\begin{aligned} \left(\frac{\partial^2}{\partial z^2} - k^2\right)\Phi_{1,1} &= 0; \quad -h \le z \le \eta_c \\ \Phi_{1,1_z} &= 0; \quad z = -h \\ \left(\frac{\partial}{\partial z} - \sigma^2\right)\Phi_{1,1} &= 0; \quad z = \eta_c \end{aligned} \tag{5.30}$$

which yields the linear solution for a propagating wave

$$\Phi_{1,1} = -\frac{iA}{2\sigma}\left(\frac{\cosh Q}{\cosh q}\right) \tag{5.31a}$$

$$\sigma^2 = k \tanh q \tag{5.31b}$$

where A is the wave amplitude, and the following definitions have been used for compactness

$$Q \equiv k(z+h) \qquad q \equiv k(h+\eta_c) \tag{5.32}$$

Substituting the solution for Φ_1 in the forcing term for η_1 yields at the different harmonics

$$\eta_{1,0} = 0 \tag{5.33a}$$

$$\eta_{1,1} = \frac{A}{2} \tag{5.33b}$$

5.2.2.2 Second order solution

Using the solutions at $n = 1$, the forcing terms at this order can be determined and are given by

$$F_{2,0} = 0 \quad ; \quad F_{2,1} = -\frac{kA_{X_1}}{\sigma}\left(\frac{\cosh Q}{\cosh q}\right) \quad ; \quad F_{2,2} = 0$$

$$G_{2,0} = 0 \quad ; \quad G_{2,1} = 0 \quad ; \quad G_{2,2} = 0$$

$$J_{2,0} = \alpha|A|^2\left\{\left(\frac{i\sigma^3}{4\sinh^2 q} + c.c.\right) - \frac{i\left(\sigma-\sigma^*\right)|\sigma|^2}{2|\tanh q|^2}\left(1+|\tanh q|^2\right)\right\} \quad ;$$
$$J_{2,1} = A_{T_1} + UA_{X_1} \quad ; \quad J_{2,2} = \frac{3i\sigma^3 A^2}{4\sinh^2 q}$$

where α defined by

$$\alpha \equiv e^{\psi-\psi^*} \tag{5.35}$$

is a coefficient which denotes the nonlinear forcing mechanism. Note that $\alpha = 1$ everywhere before the blocking point. Beyond the blocking point α will either be an exponentially growing or decaying function depending upon the choice of the wave number.

At $m = 0$ we have

$$\Phi_{2,0_{zz}} = 0 \qquad -h \leq z \leq \eta_c$$

$$\Phi_{2,0_z} = 0 \qquad z = -h$$

and thus get

$$\Phi_{2,0} = \Phi_{2,0}(X_1, X_2, Y_1, Y_2, T_1, T_2, \cdots) \tag{5.37}$$

At $m = 1$ we have

$$\left(\frac{\partial^2}{\partial z^2} - k^2\right)\Phi_{2,1} = -\frac{kA_{X_1}}{\sigma}\Big(\frac{\cosh Q}{\cosh q}\Big); \quad -h \leq z \leq \eta_c$$

$$\Phi_{2,1_z} = 0; \quad z = -h$$

$$\left(\frac{\partial}{\partial z} - \sigma^2\right)\Phi_{2,1} = A_{T_1} + UA_{X_1}; \quad z = \eta_c$$

Substituting the forcing terms $F_{2,1}, G_{2,1}$ and $J_{2,1}$, and solution at $n = 1$ in (5.28) yields

$$A_{T_1} + (U + C_g)A_{X_1} = 0 \tag{5.39}$$

where C_g is the group velocity for a wave propagating in a frame of reference with the current and is given by

$$C_g = \frac{\sigma}{2k}\Big(1 + \frac{2q}{\sinh 2q}\Big) \tag{5.40}$$

The homogeneous solution for $\Phi_{2,1}$ is the same as $\Phi_{1,1}$, and the particular solution can be obtained by the method of variation of parameters to yield

$$\Phi_{2,1} = -\frac{iB}{2\sigma}\Big(\frac{\cosh Q}{\cosh q}\Big) - \Big(\frac{Q\sinh Q}{2k\sigma\cosh q}\Big)A_{X_1}$$

The first term in the expression can be absorbed in the solution for $\Phi_{1,1}$ and we get

$$\Phi_{2,1} = -\Big(\frac{Q\sinh Q}{2k\sigma\cosh q}\Big)A_{X_1} \tag{5.41}$$

At $m = 2$ we have

$$\left(\frac{\partial^2}{\partial z^2} - 4k^2\right)\Phi_{2,2} = 0; \quad -h \leq z \leq \eta_c$$

$$\Phi_{2,2_z} = 0; \quad z = -h$$

$$\left(\frac{\partial}{\partial z} - 4\sigma^2\right)\Phi_{2,2} = \frac{3i\sigma^3A^2}{4\sinh^2 q}; \quad z = \eta_c$$

which yields the particular solution

$$\Phi_{2,2} = -\frac{3i\sigma A^2\cosh 2Q}{16\sinh^4 q} \tag{5.43}$$

Eqns (5.37), (5.41) and (5.43) give the solution for Φ_2, and together with the solutions for Φ_1 and η_1 can be substituted in the forcing term for η_2 to yield at the different harmonics

$$\eta_{2,0} = -\left[\Big(\Phi_{1,0_{T_1}} + U\Phi_{1,0_{X_1}}\Big) + \frac{|A|^2}{4}\alpha\Big(\frac{|\sigma|^2(1+|\tanh q|^2)}{|\tanh q|^2} - (k\tanh q + c.c.)\Big)\right] \tag{5.44a}$$

$$\eta_{2,1} = \frac{i}{2\sigma}\left[A_{T_1} + \Big(U - \frac{q\sigma\tanh q}{k}\Big)A_{X_1}\right] \tag{5.44b}$$

$$\eta_{2,2} = \frac{k\cosh q}{8\sinh^3 q}(2\cosh^2 q + 1)A^2 \tag{5.44c}$$

5.2.2.3 Third order solution

To determine the governing envelope equations at third order we only need to evaluate the solvability condition at $n = 3$. Using the solutions at $n = 2$ and $n = 1$, the forcing terms for $m = 0, 1$ at third order are given by

$$\begin{aligned}
F_{3,0} &= -\Big(\Phi_{1,0_{X_1X_1}} + \Phi_{1,0_{Y_1Y_1}}\Big) \\
F_{3,1} &= \frac{i}{2\sigma}\Big(A_{X_1X_1} + A_{Y_1Y_1}\Big)\frac{\cosh Q}{\cosh q} - \frac{1}{2}\Bigg[k\Big(\frac{A\cosh Q}{\sigma\cosh q}\Big)_{X_2} + \Big(\frac{kA\cosh Q}{\sigma\cosh q}\Big)_{X_2}\Bigg] \\
&+ \frac{iQ\sinh Q}{\sigma\cosh q}A_{X_1X_1}
\end{aligned} \tag{5.45a}$$

$$G_{3,0} = 0 \quad ; \quad G_{3,1} = -h_{X_2}\frac{kA}{2\sigma\cosh q} \tag{5.45b}$$

$$\begin{aligned}
J_{3,0} &= -\Big(\Phi_{1,0_{T_1T_1}} + 2U\Phi_{1,0_{X_1T_1}} + U^2\Phi_{1,0_{X_1X_1}}\Big) \\
&+ \frac{\alpha}{2}\Bigg\{\Big(\frac{\sigma-\sigma^*}{|\sigma|^2}\Big)(A_{X_1}A^*R_1 - A^*_{X_1}AR^*_1) + \Big\{A_{X_1}A^*\big(\frac{R_2}{2} + R_3\big) + c.c.\Big\}\Bigg\} \\
J_{3,1} &= \frac{Ub_{X_2}}{b}Y_1A_{Y_1} + \frac{kA}{2\sigma}\eta_{c_{X_2}} + \frac{A}{2b}(Ub)_{X_2} + i\Big(\frac{C_g^2}{2\sigma} + \frac{q\sigma^2C_g}{k^2}\Big)A_{X_1X_1} \\
&+ \frac{1}{2}\Big(A_{T_2} + UA_{X_2}\Big) + \frac{A_{T_2}}{2} + \frac{U\sigma}{2}\Big(\frac{A}{\sigma}\Big)_{X_2} \\
&- \frac{i\sigma kA}{\sinh 2q}\Bigg(\Phi_{1,0_{T_1}} + \Big(U - \frac{\sinh 2q}{\sigma}\Big)\Phi_{1,0_{X_1}}\Bigg) + i\alpha|A|^2A(R_4 + R_5)
\end{aligned} \tag{5.45c}$$

where

$$R_1 = k^* + \frac{q|k|^2\sigma^2}{k^2} + (\sigma^*)^2(q + \tanh q) \tag{5.46a}$$

$$R_2 = \frac{k}{\sigma}(2 - \tanh^2 q) - \frac{q\tanh q}{k}\Big(\frac{k^2}{\sigma\cosh^2 q}\Big)^* \tag{5.46b}$$

$$R_3 = C_g\Big(\frac{|k|^2}{|\sigma|^2} - \frac{(k^*)^2}{2|\sigma|^2\cosh^2 q^*} - \sigma(\sigma - \sigma^*)\Big) \tag{5.46c}$$

$$R_4 = \frac{(\sigma - \sigma^*)}{4|\sigma|^2}|k|^2(k + k^*)(\tanh q + \tanh q^*) \tag{5.46d}$$

$$\begin{aligned} R_5 = \frac{1}{8\sinh^4 q}\Bigg\{ & \frac{3|k|^2}{|\sigma|^2}\sigma^2(2\sigma - \sigma^*)\cosh 2q + 3k|\sigma|^2(2\sigma - \sigma^*)\sinh 2q \\ & + 3\sigma k^2(1 - 2\sinh^2 q) - \sigma^3\sinh^2 q\Big(\frac{|\sigma|^2(1 + |\tanh q|^2)}{|\tanh q|^2} \\ & - (k\tanh q + k^*\tanh q^*)\Big) - \frac{|k|^2\sigma^*\sinh 2q(1 + 2\cosh^2 q)}{2\sinh 2q^*} \\ & - \sinh^2 q\Big(\frac{|k|^2\sigma^3}{|\sigma|^2} + \frac{k(k - k^*)}{\sigma}\sinh^2 q\big(\frac{|k|^2}{|\sigma|^2} + |\sigma|^2\big)\Big) \\ & + \frac{|k|^2}{|\sigma|^2}\sigma\sinh^4 q(k + k^*)(\tanh q + \tanh q^*)\Bigg\} \end{aligned} \tag{5.46e}$$

Substituting the forcing terms in (5.26) and (5.28) and simplifying, we get a set of coupled equations

$$\begin{aligned} & \Phi_{1,0_{T_1T_1}} + 2U\Phi_{1,0_{X_1T_1}} + U^2\Phi_{1,0_{X_1X_1}} - (h + \eta_c)\Big(\Phi_{1,0_{X_1X_1}} + \Phi_{1,0_{Y_1Y_1}}\Big) \\ & = \frac{\alpha}{2}\Bigg\{\Big(\frac{\sigma - \sigma^*}{|\sigma|^2}\Big)(A_{X_1}A^*R_1 - A^*_{X_1}AR^*_1) + \Big\{A_{X_1}A^*\big(\frac{R_2}{2} + R_3\big) + c.c.\Big\}\Bigg\} \end{aligned} \tag{5.47a}$$

$$\begin{aligned} & 2A_{T_2} + 2(U + C_g)A_{X_2} + \sigma\Big(\frac{U + C_g}{\sigma}\Big)_{X_2}A - i\sigma_{kk}A_{X_1X_1} - i\frac{C_g}{k}A_{Y_1Y_1} \\ & + \frac{Ub_{X_2}}{b}Y_1A_{Y_1} - \frac{2i\sigma kA}{\sinh 2q}\Bigg(\Phi_{1,0_{T_1}} + \Big(U - \frac{\sinh 2q}{\sigma}\Big)\Phi_{1,0_{X_1}}\Bigg) \\ & + 2i\alpha|A|^2A(R_5 + R_6) = 0 \end{aligned} \tag{5.47b}$$

where

$$\sigma_{kk} = \frac{2q\sigma\cosh^2 q}{k^2\sinh 2q} - \frac{C_g^2}{\sigma} - \frac{2q\sinh qC_g}{k\cosh q} \tag{5.48}$$

The variation in the channel width can be taken into account by integrating (5.47) across the channel and using the lateral boundary conditions. From (5.14) and (5.17) the lateral boundary conditions is given by

$$\Phi_{1,0_{Y_1}} = 0; \quad Y_1 = \pm\epsilon b \tag{5.49a}$$

$$A_{Y_1} = \pm i\epsilon k A b_{X_2}; \quad Y_1 = \pm\epsilon b \tag{5.49b}$$

Integrating (5.47) across $Y_1 = \pm\epsilon b$ and using (5.49) we get a set of coupled equations for the width averaged amplitude $\bar{A}$, and long wave $\bar{\Phi}_{1,0}$

$$\begin{aligned}&\bar{\Phi}_{1,0_{T_1T_1}} + 2U\bar{\Phi}_{1,0_{X_1T_1}} + (U^2 - (h+\eta_c))\bar{\Phi}_{1,0_{X_1X_1}} \\ &= \frac{\alpha}{2}\left\{ \Big(\frac{\sigma - \sigma^*}{|\sigma|^2}\Big)(\bar{A}_{X_1}\bar{A}^* R_1 - \bar{A}^*_{X_1}\bar{A}{R_1}^*) + \Big\{\bar{A}_{X_1}\bar{A}^*\big(\frac{R_2}{2} + R_3\big) + c.c.\Big\}\right\}\end{aligned} \tag{5.50a}$$

$$\begin{aligned}&2\bar{A}_{T_2} + 2(U + C_g)\bar{A}_{X_2} + \frac{\sigma}{b}\Big(\frac{(U+C_g)b}{\sigma}\Big)_{X_2}\bar{A} - i\sigma_{kk}\bar{A}_{X_1X_1} \\ &- \frac{2i\sigma k\bar{A}}{\sinh 2q}\left(\bar{\Phi}_{1,0_{T_1}} + \Big(U - \frac{\sinh 2q}{\sigma}\Big)\bar{\Phi}_{1,0_{X_1}}\right) + 2i\alpha|\bar{A}|^2\bar{A}(R_5 + R_6) = 0\end{aligned} \tag{5.50b}$$

Eqn. (5.50) is a third order weakly non-linear evolution model for a narrow-banded wave envelope propagating on a strong current in a narrow varying channel. The model is also valid beyond the blocking point.

For sake of convenience we shall rewrite (5.50) in dimensional form

$$\begin{aligned}&\bar{\Phi}_{1,0_{tt}} + 2U\bar{\Phi}_{1,0_{xt}} + (U^2 - g(h+\eta_c))\bar{\Phi}_{1,0_{xx}} \\ &= \frac{\alpha g^2}{2}\left\{ \Big(\frac{\sigma - \sigma^*}{|\sigma|^2}\Big)(\bar{A}_x\bar{A}^* R_1 - \bar{A}^*_x\bar{A}{R_1}^*) + \Big\{\bar{A}_x\bar{A}^*\big(\frac{R_2}{2} + R_3\big) + c.c.\Big\}\right\}\end{aligned} \tag{5.51a}$$

$$\begin{aligned}&2\bar{A}_t + 2(U + C_g)\bar{A}_x + \frac{\sigma}{b}\Big(\frac{(U + C_g)b}{\sigma}\Big)_x \bar{A} - i\sigma_{kk}\bar{A}_{xx} \\ &- \frac{2i\sigma k\bar{A}}{g\sinh 2q}\left(\bar{\Phi}_{1,0_t} + \Big(U - \frac{g\sinh 2q}{\sigma}\Big)\bar{\Phi}_{1,0_x}\right) + 2i\alpha|\bar{A}|^2\bar{A}(gR_5 + R_6) = 0\end{aligned} \tag{5.51b}$$

where the primes have been omitted for brevity. The expression for σ is now given by

$$\sigma^2 = gk\tanh q \tag{5.52}$$

The expressions for the coefficients R_1 to R_6, C_g and σ_{kk} remain unchanged except that they are now evaluated with the dimensional values of σ and k.

When there is no wave blocking then ψ, k and σ are real and (5.51) simplifies to

$$\bar{\Phi}_{1,0_{tt}} + 2U\bar{\Phi}_{1,0_{xt}} + (U^2 - g(h + \eta_c))\bar{\Phi}_{1,0_{xx}} = \alpha\Big\{\frac{\sigma^3}{2k\tanh^2 q} + \frac{C_g\sigma^2}{4\sinh^2 q}\Big\}(|A|^2)_x \tag{5.53a}$$

$$\begin{aligned}&2\bar{A}_t + 2(U + C_g)\bar{A}_x + \frac{\sigma}{b}\Big(\frac{(U + C_g)b}{\sigma}\Big)_x \bar{A} - i\sigma_{kk}\bar{A}_{xx} - \frac{2i\sigma k\bar{A}}{g\sinh 2q}\left(\bar{\Phi}_{1,0_t}\right. \\ &\left. + \Big(U - \frac{g\sinh 2q}{\sigma}\Big)\bar{\Phi}_{1,0_x}\right) + 2i\alpha|\bar{A}|^2\bar{A}\Big(\frac{\sigma k^2(\cosh 4q + 8 - 2\tanh^2 q)}{16\sinh^4 q}\Big) = 0\end{aligned} \tag{5.53b}$$

For a constant width (5.53) reduces to the 1-D evolution model of Turpin *et al.* (1983).

In the linear limit, and neglecting frequency dispersion (5.51) reduces to

$$2\bar{A}_t + 2(U + C_g)\bar{A}_x + \frac{\sigma}{b}\Big(\frac{(U + C_g)b}{\sigma}\Big)_x \bar{A} = 0 \tag{5.54}$$

Multiplying (5.54) with $\frac{1}{\rho}g\bar{A}^*$, adding the complex conjugate of the resulting equation and using the following definition for wave energy E

$$E \equiv \frac{1}{2}\rho g|\bar{A}|^2,$$

we get

$$\left(\frac{E}{\sigma}\right)_t + \frac{1}{b}\left(\frac{b(U + C_g)E}{\sigma}\right)_x = 0 \tag{5.55}$$

Eqn. (5.55) is the width integrated wave action conservation principle.

5.2.2.4 Choice of k beyond the blocking point

We have already seen from the graphical solution of the dispersion relation in Figure 5.1 that beyond the blocking point we get a pair of complex conjugate roots. The choice of the wave number has to be done carefully so as to choose the decaying solution beyond the blocking point.

Based on the equation for the surface motion

$$\eta_w = \frac{A}{2}e^{i\psi} + O(\epsilon)$$

and the expression for non-linear forcing given by (5.35), a positive $Im(k)$ ($Im(f)$ refers to the imaginary part of complex function f) seems to be the appropriate choice as it leads to a decaying solution for the surface motion and the non-linear forcing for a *fixed* wave amplitude. However, since both the forcing term and the surface motion are dependent on the wave amplitude, it is necessary to study how the envelope equation varies beyond the blocking point before choosing the wave number root.

Consider a linearized version of the evolution equation (5.51) in a uniform medium (i.e. no shoaling)

$$2\bar{A}_t + 2(U + C_g)\bar{A}_x - i\sigma_{kk}\bar{A}_{xx} = 0 \tag{5.56}$$

Assuming a plane wave solution for the wave amplitude

$$\bar{A} = ae^{i(Kx - \Omega t)}$$

and substituting in (5.56) we get

$$\Omega = (U + C_g)K + K^2 \frac{\sigma_{kk}}{2} \tag{5.57}$$

Solving the quadratic eqn. (5.57) for K, we get a pair of solutions

$$K_1 = \Big(\frac{-(U + C_g) + \sqrt{(U + C_g)^2 + 2\Omega\sigma_{kk}}}{\sigma_{kk}}\Big) \tag{5.58a}$$

$$K_2 = \Big(\frac{-(U + C_g) - \sqrt{(U + C_g)^2 + 2\Omega\sigma_{kk}}}{\sigma_{kk}}\Big) \tag{5.58b}$$

Figure 5.2 shows the plots of the two roots as a function of Ω for a wave with $T = 1.2s$. In the figure $K_1 \rightarrow 0$ as $\Omega \rightarrow 0$, which means that for this root the wave amplitude will be constant in space when there are no modulations in time, which makes physical sense. However, in the case of K_2 there will be spatial modulations in the wave amplitude even in the absence of any temporal variations. Furthermore, in the deep water limit, with $\frac{\Omega}{\sigma} \ll 1$, the roots can be approximated as

$$K_1 \approx \frac{2k\Omega}{\sigma} \tag{5.59a}$$

$$K_2 \approx 2k\Big(2 - \frac{\Omega}{\sigma}\Big) \tag{5.59b}$$

which yields

$$\frac{d\Omega}{dK_1} \approx \frac{\Omega}{2k} \tag{5.60a}$$

$$\frac{d\Omega}{dK_2} \approx -\frac{\Omega}{2k} \tag{5.60b}$$

K_2 has a negative group velocity and will propagate wave energy backwards. Thus, K_2 is the spurious root to the solution.

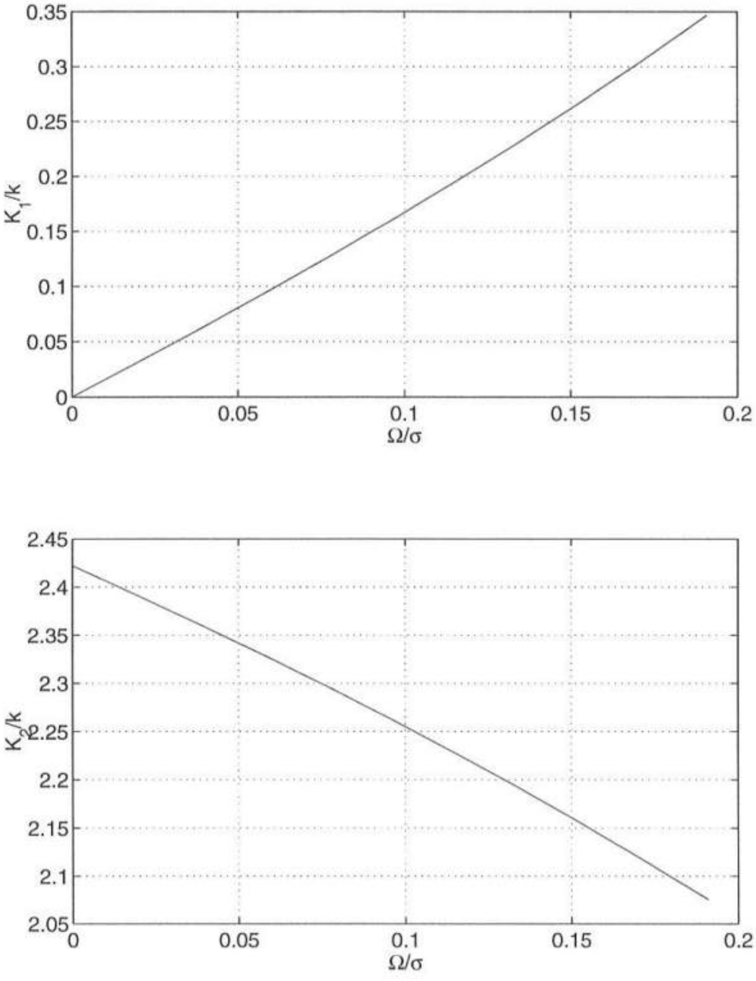

Figure 5.2: K_1 and K_2 as a function of Ω. (T = 1.2 s, U = 0.0 m/s, h = 0.5 m)

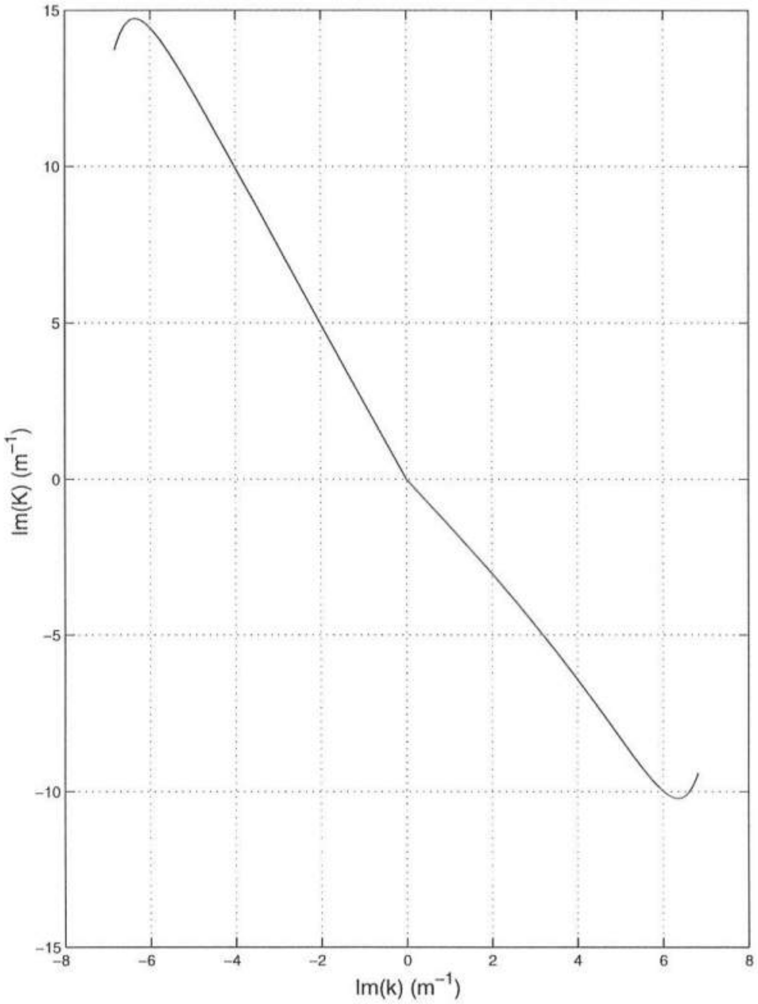

Figure 5.3: $Im(K_1)$ as a function of $Im(k)$

A positive $Im(K_1)$ will yield a decaying solution for the envelope equation beyond the blocking point. Using (5.48) and (5.40) $Im(K_1)$ has been plotted as a function of $Im(k)$ in Figure 5.3, for $\Omega \approx 0.5\mathrm{s}^{-1}$. From the figure it is clear that the choice of a positive $Im(k)$ will lead to an exponential growth in the wave amplitude A. Since $|Im(K_1)| > |Im(k)|$, the growth in the amplitude will be stronger than the subsequent decay due to the complex phase, causing the waves to blow up beyond the blocking point. Thus, to simulate wave blocking we have to choose the root with a negative $Im(k)$.

5.2.2.5 Energy dissipation due to wave breaking

Energy dissipation due to wave breaking is introduced as an additional sink term in the envelope equation. Considering only the shoaling model we have

$$2\bar{A}_{T_2} + 2(U + C_g)\bar{A}_{X_2} + \frac{\sigma}{b}\left(\frac{(U + C_g)b}{\sigma}\right)_{X_2} \bar{A} + \gamma\bar{A} = 0 \tag{5.61}$$

where γ is the energy dissipation coefficient. The expression for γ is evaluated using the empirical dissipation term D (given by eqns. (3.3) and (3.8) developed in Chapter 3).

To compare γ with D, we first write (5.61) as an energy equation in exactly the same way as we did for (5.55)

$$\frac{1}{b}\left[\frac{\partial}{\partial x}\left(\frac{bE(U + C_g)}{\sigma}\right)\right] = -\frac{\gamma E}{\sigma} \tag{5.62}$$

where we have made the assumption of steady waves to eliminate the time derivative term. Comparing eqns. (5.62), (3.3) and (3.8) we get

$$\gamma = \frac{2\beta}{\sigma\pi} g k^2 |A| \tag{5.63}$$

Similar to the Miche's criterion used in Chapter 3, a slope criterion is used to determine the onset of wave breaking. But for numerical stability reasons the energy dissipation term is ramped up smoothly as waves approach the limiting slope

$$\gamma = \frac{2\beta}{\sigma\pi} g k^2 |A| [1 + \tanh(40(m - m_0))] \tag{5.64}$$

where the terms in the square brackets is the empirical ramp function, m is the wave slope ($m = k|A|$) and m_0 is the limiting slope based on (3.9) in Chapter 3.

5.3 Numerical Scheme

The set of coupled equations in (5.51) are solved using two second order finite difference schemes. The spatial coordinate x has been discretized by $x_j = j\Delta x$, while the time has been discretized by $t_k = k\Delta t$.

For the long wave motion we use a backward time centered space (BTCS) numerical scheme. The derivatives are thus given by

$$\bar{\Phi}_{1,0_{tt}} = \frac{1}{(\Delta t)^2}\left(\bar{\Phi}^{k+1}_{1,0_j} + \bar{\Phi}^{k-1}_{1,0_j} - 2\bar{\Phi}^{k}_{1,0_j}\right)$$

$$\bar{\Phi}_{1,0_{xx}} = \frac{1}{(\Delta x)^2}\left(\bar{\Phi}^{k+1}_{1,0_{j+1}} + \bar{\Phi}^{k+1}_{1,0_{j-1}} - 2\bar{\Phi}^{k+1}_{1,0_j}\right)$$

$$\bar{\Phi}_{1,0_{xt}} = \frac{1}{2\Delta x\Delta t}\left(\bar{\Phi}^{k+1}_{1,0_{j+1}} - \bar{\Phi}^{k+1}_{1,0_{j-1}} - \bar{\Phi}^{k}_{1,0_{j+1}} + \bar{\Phi}^{k}_{1,0_{j-1}}\right)$$

$$\bar{A}_x = \frac{1}{2\Delta x}\left(\bar{A}^{k+1}_{j+1} - \bar{A}^{k-1}_{j+1}\right)$$

Solving for the entire spatial domain at any time step leads to a set of equations which in matrix form can be written as

$$\Big[C_1\Big]\left\{\bar{\Phi}^{k+1}_{1,0}\right\} = \left\{F\left(\bar{\Phi}^{k}_{1,0}, \bar{\Phi}^{k-1}_{1,0}, \quad \text{nonlinear terms in} \quad \bar{A}^{k+1}\right)\right\} \tag{5.66}$$

For the envelope equation we use a Crank-Nicolson scheme. The scheme is centered in space, and centered in time but about grid level $k+\frac{1}{2}$ with a grid spacing of $\frac{\Delta t}{2}$. The derivatives are thus given by

$$\bar{A}_t = \frac{1}{\Delta t}\left(\bar{A}_j^{k+1} - \bar{A}_j^k\right)$$

$$\bar{A}_x = \frac{1}{4\Delta x}\left(\bar{A}_{j+1}^{k+1} - \bar{A}_{j-1}^{k+1} + \bar{A}_{j+1}^k - \bar{A}_{j-1}^k\right)$$

$$\bar{A}_{xx} = \frac{1}{2(\Delta x)^2}\left(\bar{A}_{j+1}^{k+1} + \bar{A}_{j-1}^{k+1} - 2\bar{A}_j^{k+1} + \bar{A}_{j+1}^k + \bar{A}_{j-1}^k - 2\bar{A}_j^k\right)$$

Once again solving for the entire spatial domain at a particular time step leads to a set of equations which in matrix form are given by

$$\left[C_2\right]\left\{\bar{A}^{k+1}\right\} = \left\{S\left(\bar{\Phi}_{1,0}^{k+1}, \bar{\Phi}_{1,0}^k, \bar{A}^k, \quad \text{nonlinear terms in} \quad \bar{A}^{k+1}\right)\right\} \tag{5.68}$$

The coefficient matrices in (5.66) and (5.68) are tridiagonal and can be easily inverted to obtain $\bar{\Phi}_{1,0}$ and $\bar{A}$ at the new time step for all points in the spatial domain. Since the forcing vectors F and S involve terms at time step $k+1$ the solution is obtained iteratively in the following manner.

- First we solve (5.66) using $\bar{A}^k$ in F,
- then we solve (5.68) using $\bar{\Phi}_{1,0}^{k+1}$ and $\bar{A}^k$ in S,
- we now again solve (5.66) and (5.68) using the new values of $\bar{A}^{k+1}$ in F and S.

5.3.1 Boundary conditions

For the long wave motion $\bar{\Phi}_{1,0}$ Sommerfeld radiating boundary conditions were used at both the upwave and downwave boundaries

$$\bar{\Phi}_{1,0_t} - (U + \sqrt{gh})\bar{\Phi}_{1,0_x} = 0 \quad \text{Upwave boundary} \tag{5.69a}$$

$$\bar{\Phi}_{1,0_t} + (U + \sqrt{gh})\bar{\Phi}_{1,0_x} = 0 \quad \text{Downwave boundary} \tag{5.69b}$$

For the wave envelope equation the Sommerfeld radiating boundary condition was used for the downwave boundary while the upwave boundary condition was the prescribed wave amplitude.

$$A = a_0(t)\tanh(t) \quad \text{Upwave boundary} \tag{5.70a}$$

$$\bar{A}_t + (U + C_g)\bar{A}_x = 0 \quad \text{Downwave boundary} \tag{5.70b}$$

where the $\tanh(t)$ function is used to slowly ramp up the signal to its full value and suppress noise associated with a sudden start.

To test our coupled equation numerical model we simulated the propagation of a soliton. Zakharov and Shabat (1972), using an inverse scattering technique showed that solitons are a permanent form solution of the Schrödinger equation. In the absence of any wave blocking and in a uniform medium (i.e. constant depth and width) our model (given by eqn. (5.51)) can be reduced to a Schrödinger equation. Thus, our model should be able to propagate a soliton without changing shape. The numerical simulation for a case with $b = 0.6$ m, $h = 0.5$ m, $T = 1.2$ s, $U = 0$ m/s, $\Delta x = 0.05$ m, $\Delta t = 0.0074$ s is shown in Figure 5.4. For this test case the wave envelope was prescribed inside the domain instead of at the upwave boundary. There is no change in the shape of the soliton as it propagates through the domain.

5.3.2 Numerical filter

In Section 5.2.2.4 we found that the simplified version of the evolution equation (eqn. (5.56)) yields two roots for a plane wave, of which (5.58a) is the correct root. There are several examples in the literature of numerical simulations

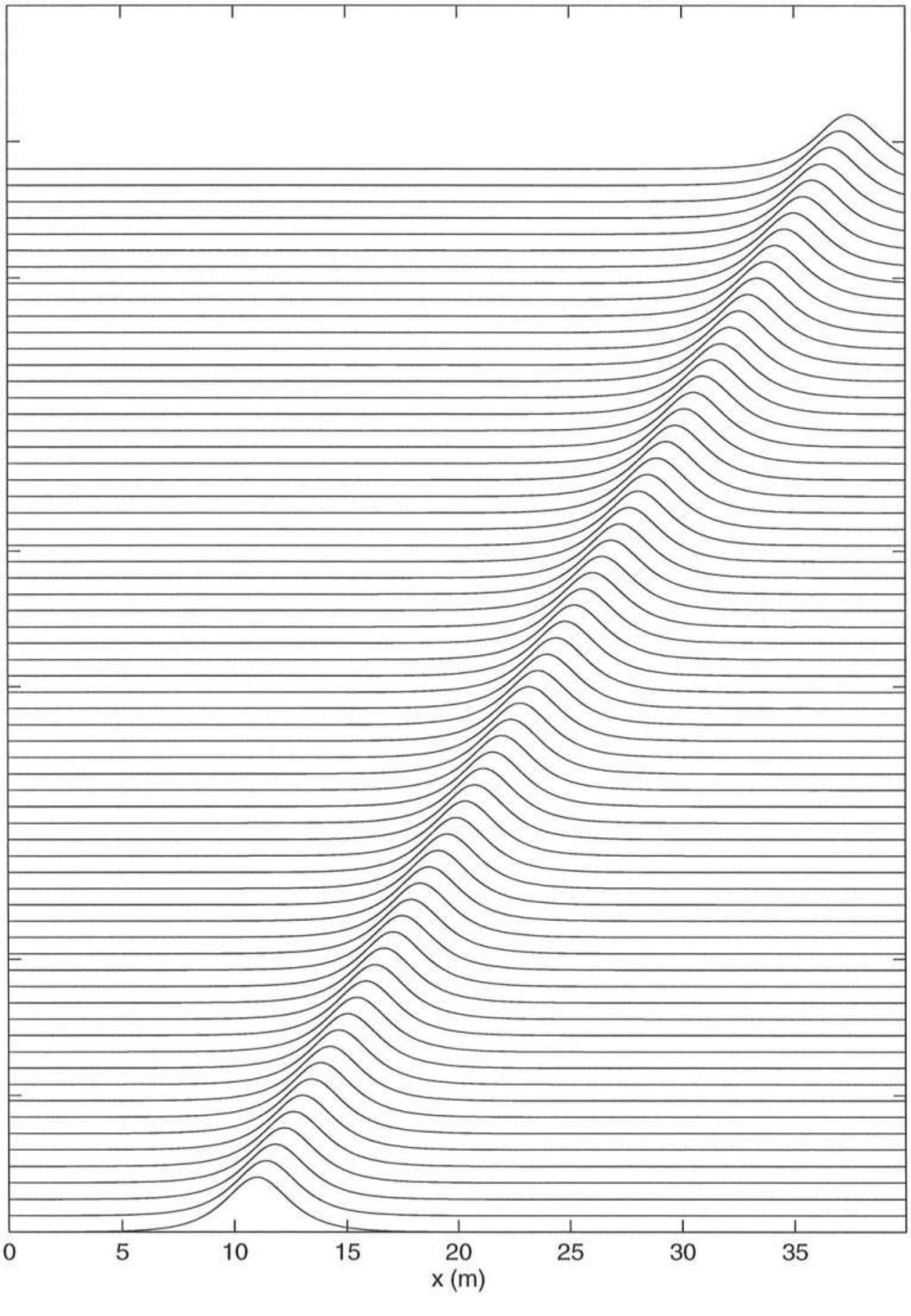

Figure 5.4: Propagation of a soliton in a uniform medium (T = 1.2 s, U = 0 m/s, h = 0.5 m)

of monochromatic wave envelopes in a uniform medium showing that the models pick up the correct root. Similar results have also been obtained in our numerical model for a monochromatic wave (see Figure 5.5). For the numerical simulation we have taken $T = 1.2$ s, $U = 0$ m/s, $h = 0.5$ m, $b = 0.6$ m, $\Delta x = 0.05$ m and $\Delta t = 0.0074$ s

However, a varying channel leads to the development of instabilities which propagate backwards. To illustrate this point consider the linearized version of (5.51)

$$2\bar{A}_t + 2(U + C_g)\bar{A}_x + \frac{\sigma}{b}\Big(\frac{(U + C_g)b}{\sigma}\Big)_x \bar{A} - i\sigma_{kk}\bar{A}_{xx} \tag{5.71}$$

Once again assuming a plane wave solution for the wave amplitude

$$\bar{A} = ae^{i(Kx - \Omega t)}$$

and substituting in the equation we get

$$\Omega = (U + C_g)K + K^2\frac{\sigma_{kk}}{2} - i\frac{\gamma_s}{2} \tag{5.72}$$

where

$$\gamma_s = \frac{\sigma}{b}\Big(\frac{(U + C_g)b}{\sigma}\Big)_x$$

or

$$\Omega = \Omega_r - i\frac{\gamma_s}{2}$$

and

$$A = a_0 e^{-\dfrac{\gamma_s}{2}} e^{i(Kx - \Omega_r t)} \tag{5.73}$$

For a contracting channel, $\gamma_s < 0$ and according to (5.73) this would lead to the growth of instabilities. In a domain that is very slowly varying the growth of these

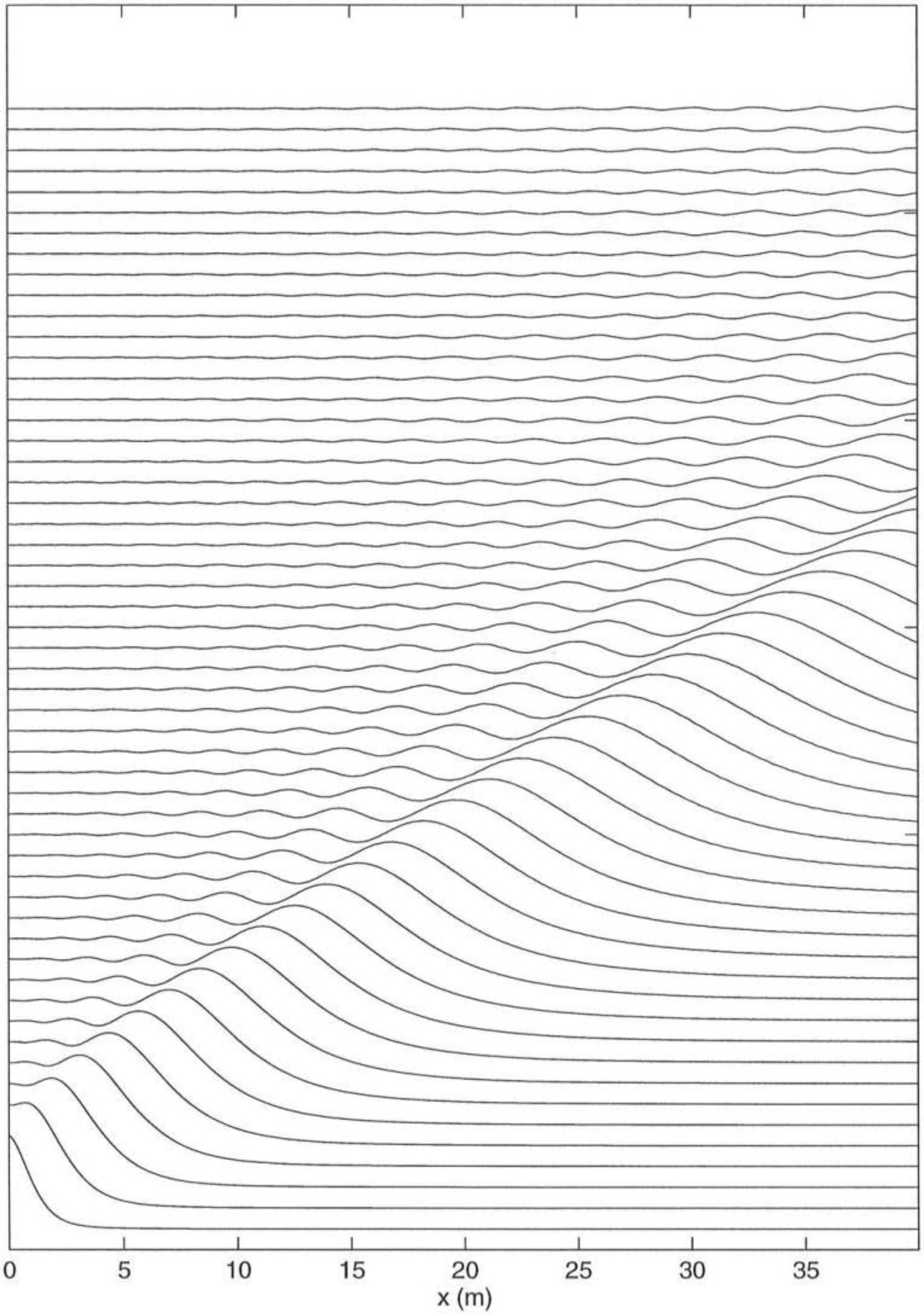

Figure 5.5: Snapshots of the spatial evolution of the wave envelope for a monochromatic wave in a uniform domain(T = 1.2s,U = 0)

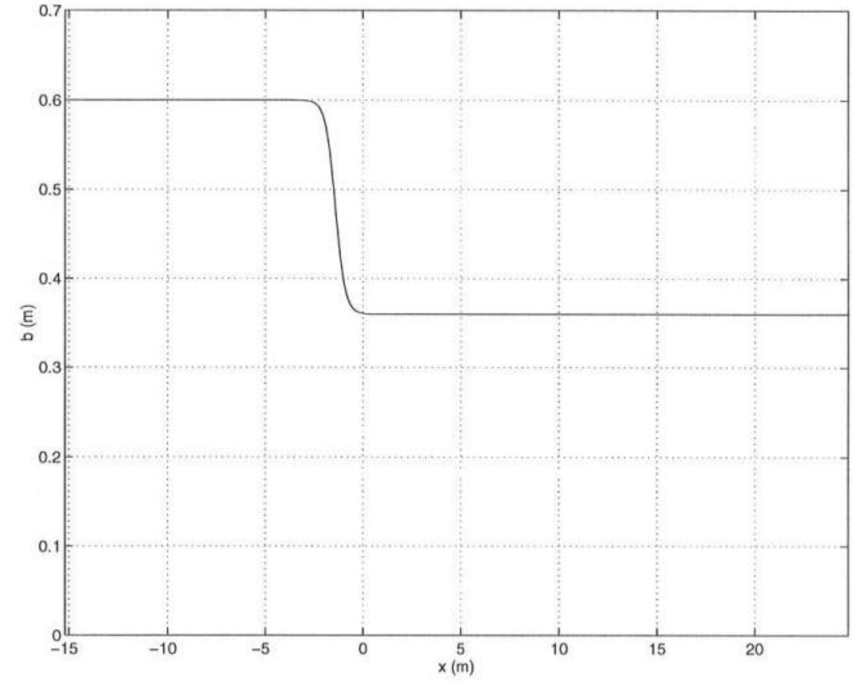

Figure 5.6: Spatial variation of domain width. Depth is constant

instabilities may be insignificant. However in our experimental tests the domain varies abruptly over a few wave lengths and the instabilities are expected to grow faster.

Numerical tests have thus been conducted to study the growth of instabilities in the varying domain. The numerical domain used is shown in Figure 5.6. The domain is similar to the one used in the experiments (see Figure 2.1 in Chapter 2), except that the varying width is described by a tanh function to remove discontinuities. For the simulations $\Delta x = 0.05$ m, $\Delta t = 0.0074$ s, $h = 0.5$ m, $U = 0$ m/s, and initial amplitude $A_0 = 0.01$m. Figure 5.7 shows the spatial snapshots of the wave envelope at different times. The limits of the region where the channel is narrowing is shown by the dashed line. The growth of the instability in the varying part of the channel can be clearly observed. This instability propagates along the spurious root K_2, and since this root has a negative group velocity the disturbance is propagated backward into the domain. An opposing current leads to a larger value of γ_s and consequently a faster growth of the instability as can be seen in Figure 5.8 for a current distribution shown in Figure 5.9. Consequently for a domain which is expanding (Figure 5.10) and has a current distribution given by Figure 5.12, the instability is damped out as can be seen in Figure 5.11.

To simulate the experimental tests conducted on narrow-banded waves (see Chapters 3 and 4) our numerical domain has to have a contracting channel. We thus need a numerical filter which will damp out the instability that propagates along the root K_2. A '3 point' filter is used for this purpose (Shapiro, 1970)

$$A_{new}|_{x=j\Delta x} = \gamma_f A|_{x=j\Delta x} + \frac{1-\gamma_f}{2}\Big(A|_{x=(j-1)\Delta x} + A|_{x=(j+1)\Delta x}\Big) \tag{5.74}$$

Substituting

$$A = A_0 e^{i(Kx-\Omega t)}$$

in the above equation, we get an amplification factor or response function R as a function of K and Δx

$$R = \frac{A_{new}}{A} = \gamma_f + (1-\gamma_f)\cos(K\Delta x) \tag{5.75}$$

where γ_f is a weighting function. Damping occurs when $R < 1$. Substituting (5.59) in (5.75) we can get the response functions for the two roots K_1 and K_2 (see Figure 5.13). The undesired root K_2 has a much higher damping rate, and can be damped out. Figure 5.14 shows the snapshots of the evolution of the same monochromatic wave as shown in Figure 5.8 with the exception that a 3 point filter with $\gamma_f = 0.65$ is used every 10 time steps. The filter damps out the disturbance with negligible effects on the desired solution.

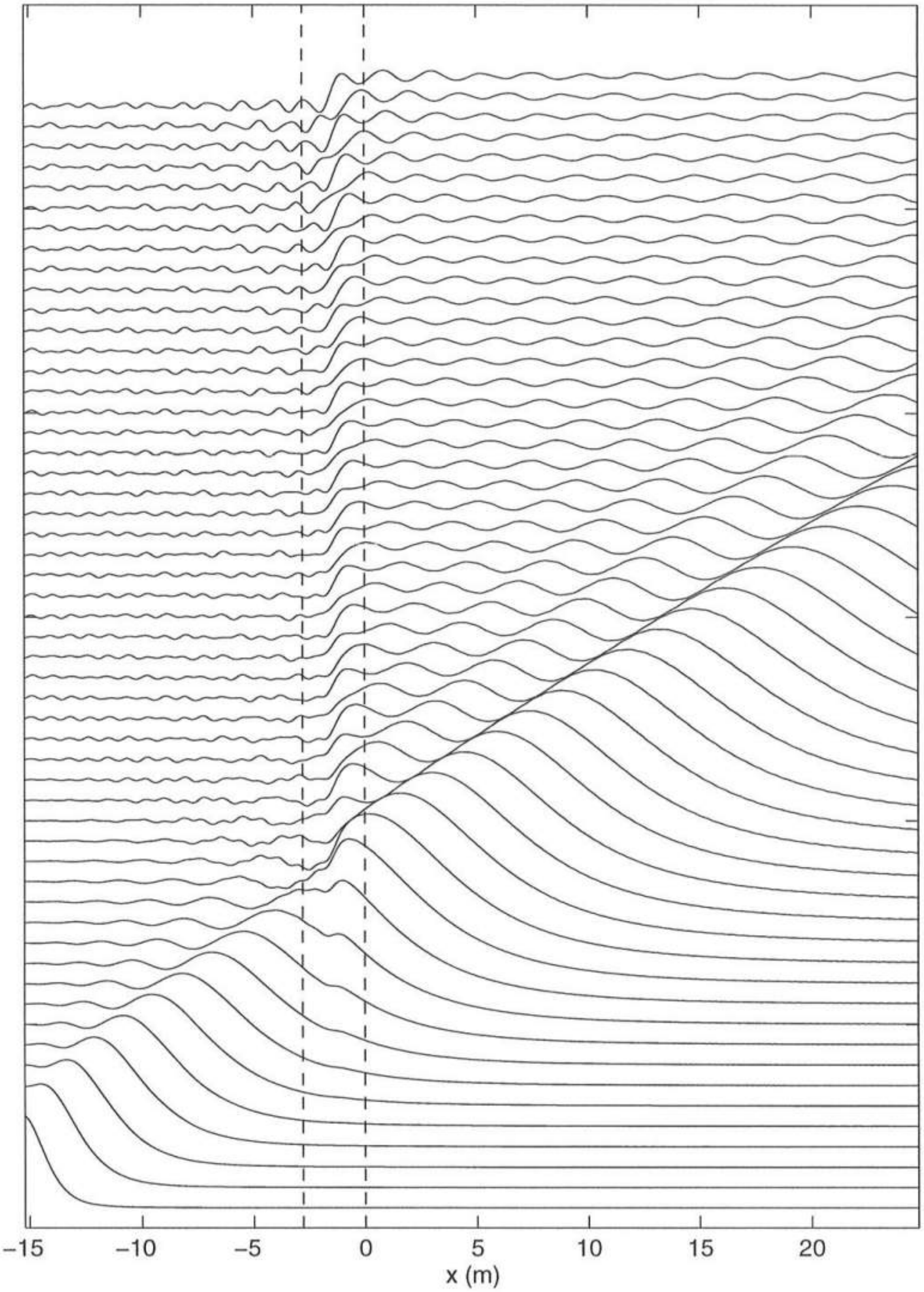

Figure 5.7: Snapshots of the spatial evolution of the wave envelope for a monochromatic wave (T = 1.2s,U = 0)

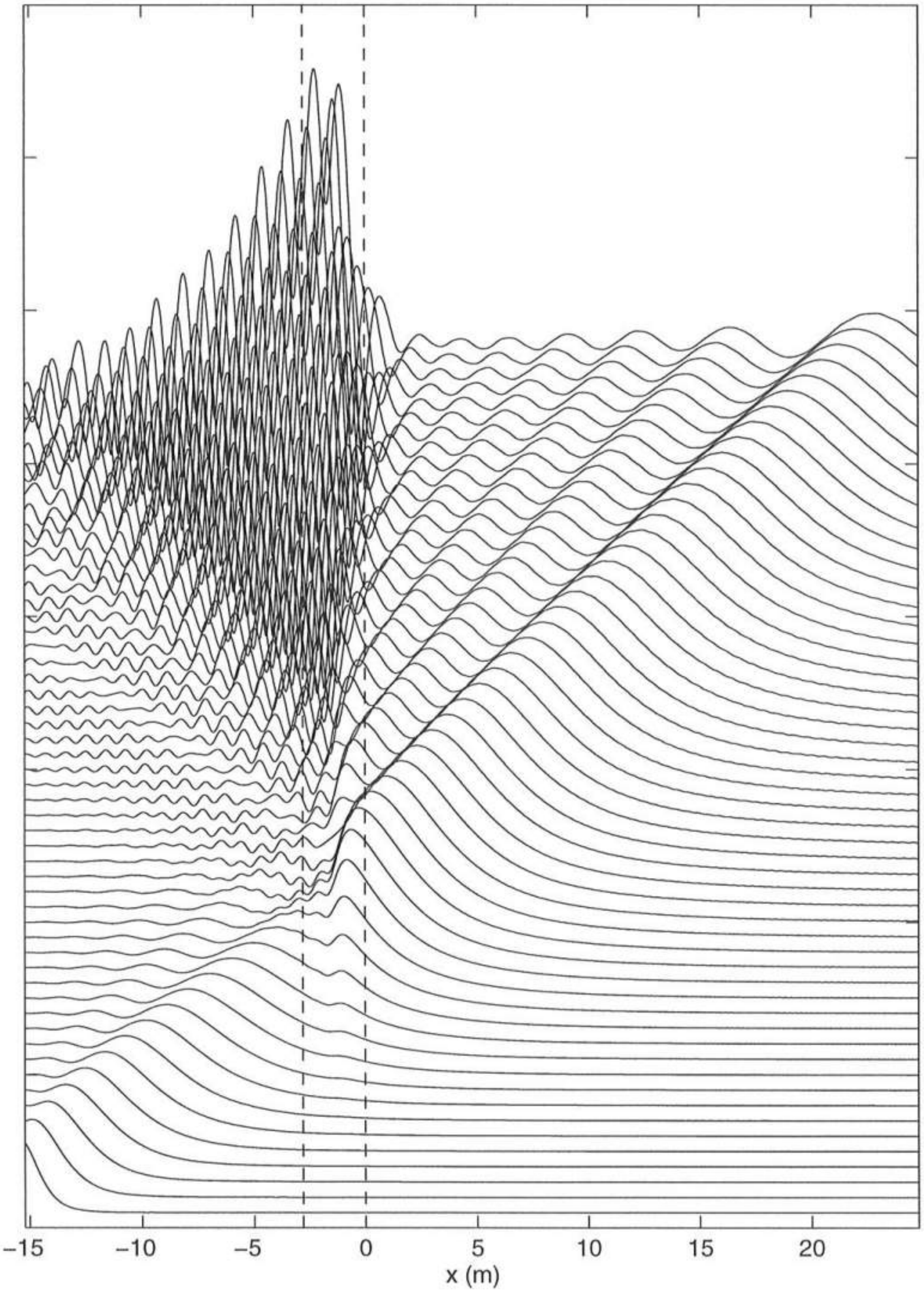

Figure 5.8: Snapshots of the spatial evolution of the wave envelope for a monochromatic wave (T = 1.2s,U given in Figure 5.9)

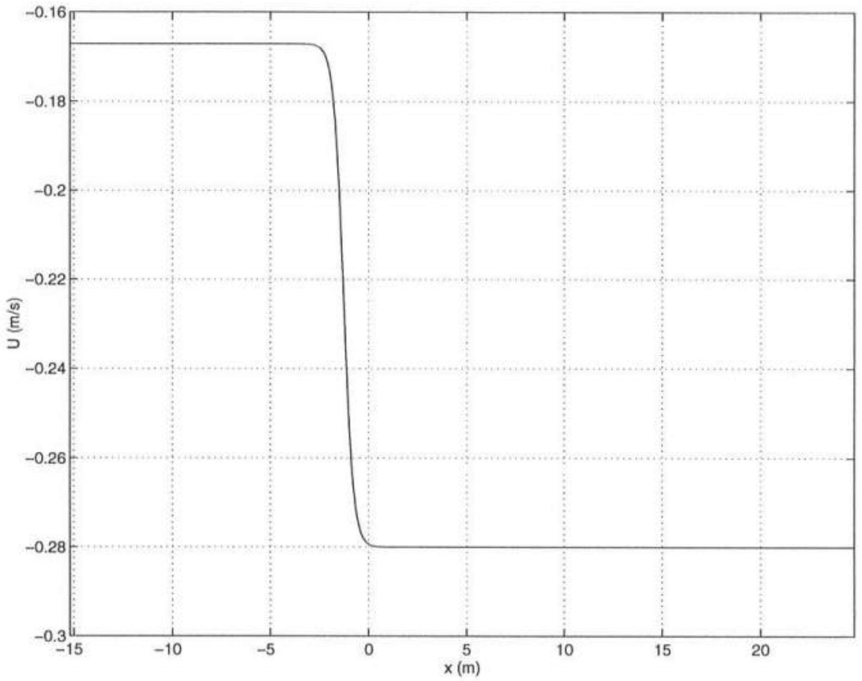

Figure 5.9: Current distribution for numerical test shown in Figure 5.8

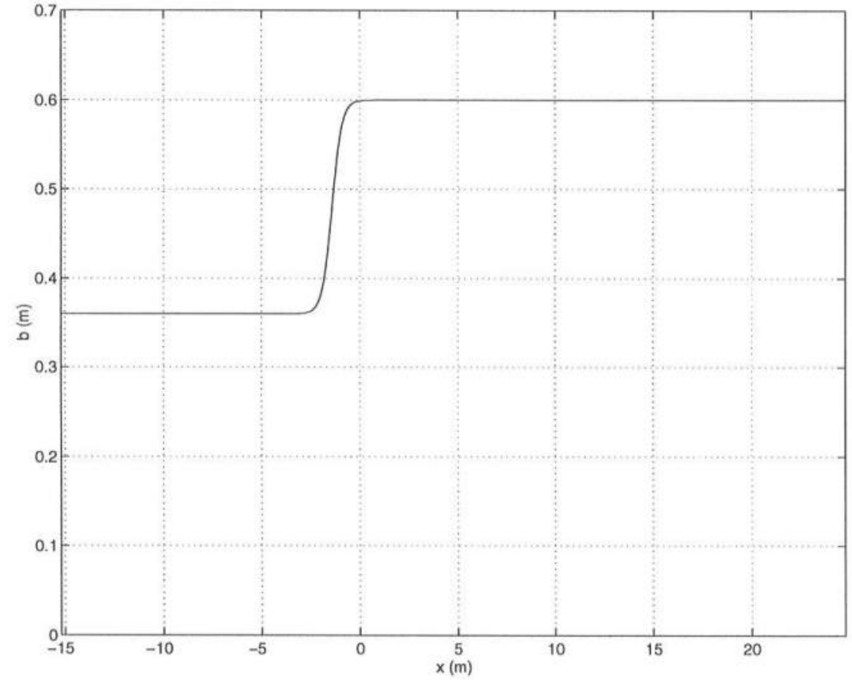

Figure 5.10: Spatial variation of width. Depth is constant

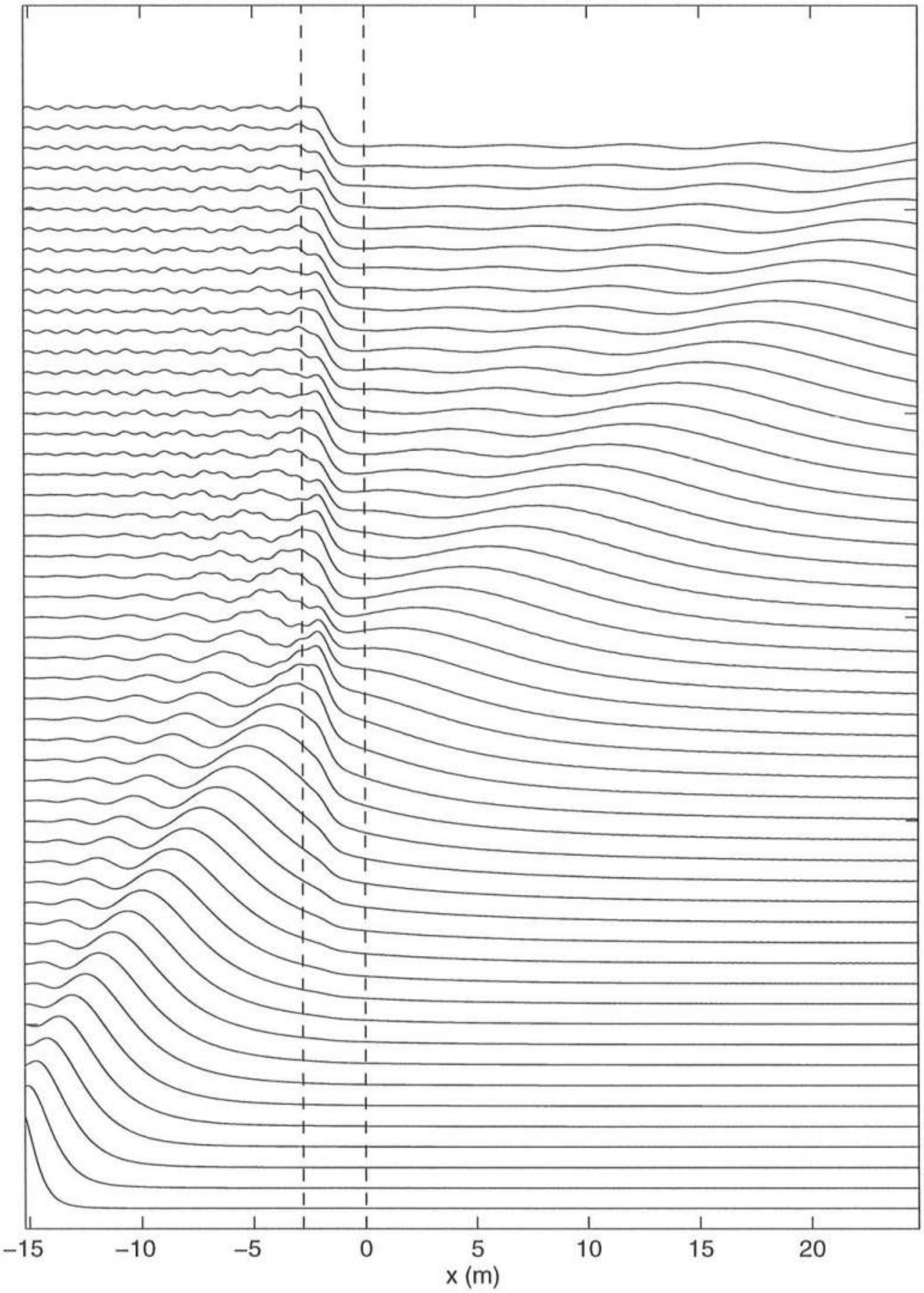

Figure 5.11: Snapshots of the spatial evolution of the wave envelope for a monochromatic wave (T = 1.2s,U given in Figure 5.12)

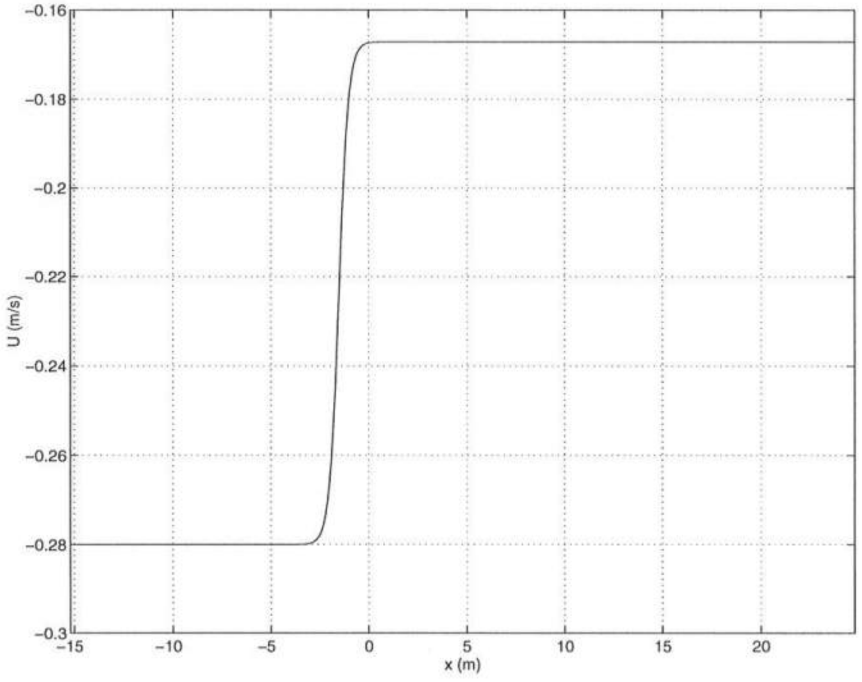

Figure 5.12: Current distribution for numerical test shown in Figure 5.11

5.4 Comparison with data

For comparing with experimental results numerical simulations were done in a domain which is linearly varying just like in the experiments. The numerical domain is shown in Figure 5.15. Numerical filtering was done every 10 time steps with $\gamma_f = 0.7$. The filtering was done only until the blocking point. It should be kept in mind that since the phase function is allowed to be complex, the actual amplitude envelope is given by $|A|e^{-Im(\psi)}$, and this expression is used to compare with the amplitude envelope of the data.

For numerical simulations of monochromatic wave trains we had $\Delta x = 0.05$ m and $\Delta t = 0.0074$ s. Figure 5.16 shows the amplitude comparison of the model with the monochromatic breaking wave Test 2 (T = 1.2 s, H = 0.009 m). From the plot we can see that the model is able to block the waves, but this blocking occurs earlier than in the data. This is because the model uses a linear dispersion relation

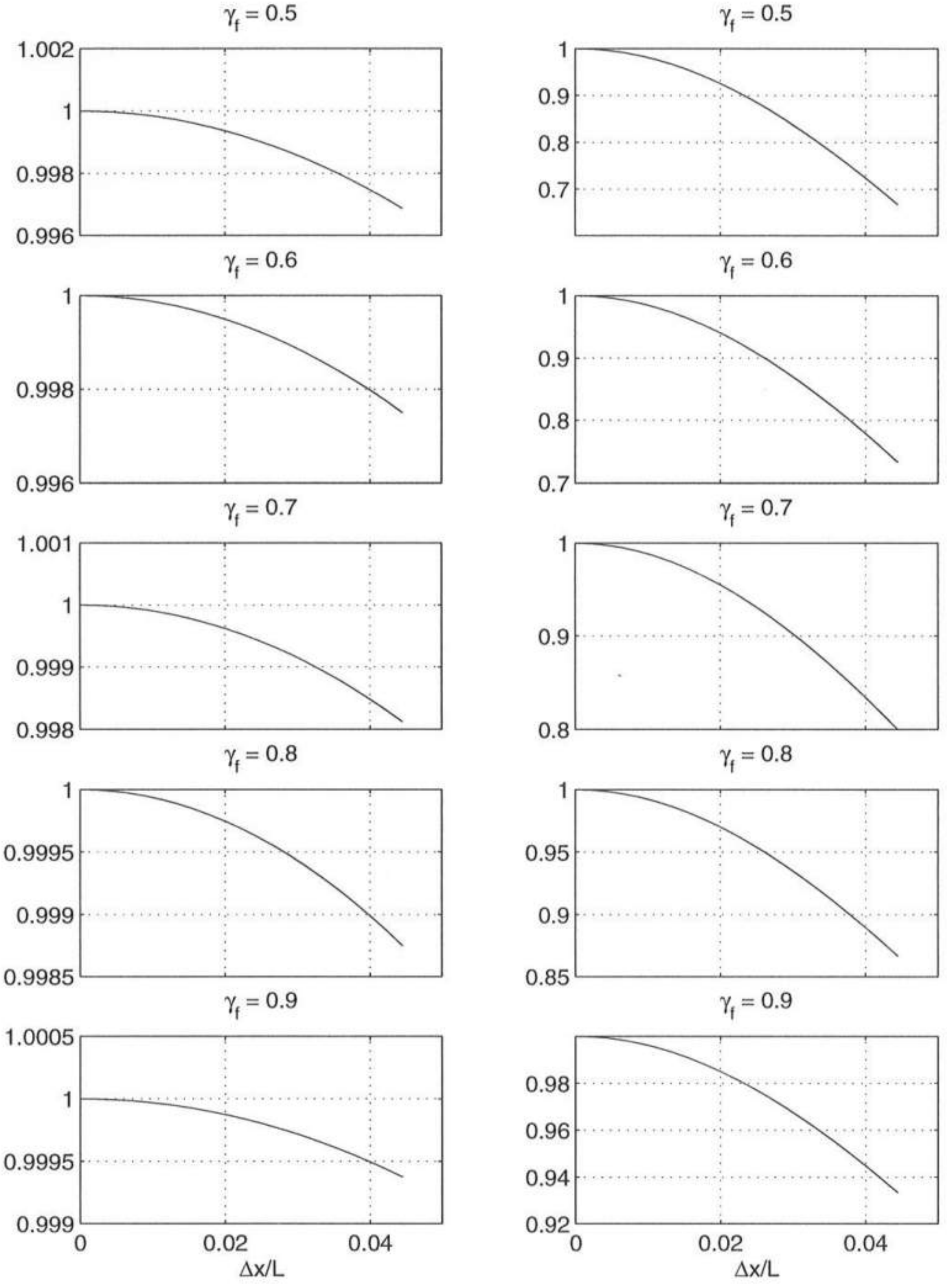

Figure 5.13: Response function for a 3 point filter. Left hand side panels correspond to K_1; Right hand side panels correspond to K_2 (T = 1.2 s; $\dfrac{\Omega}{\sigma} = 0.2$)

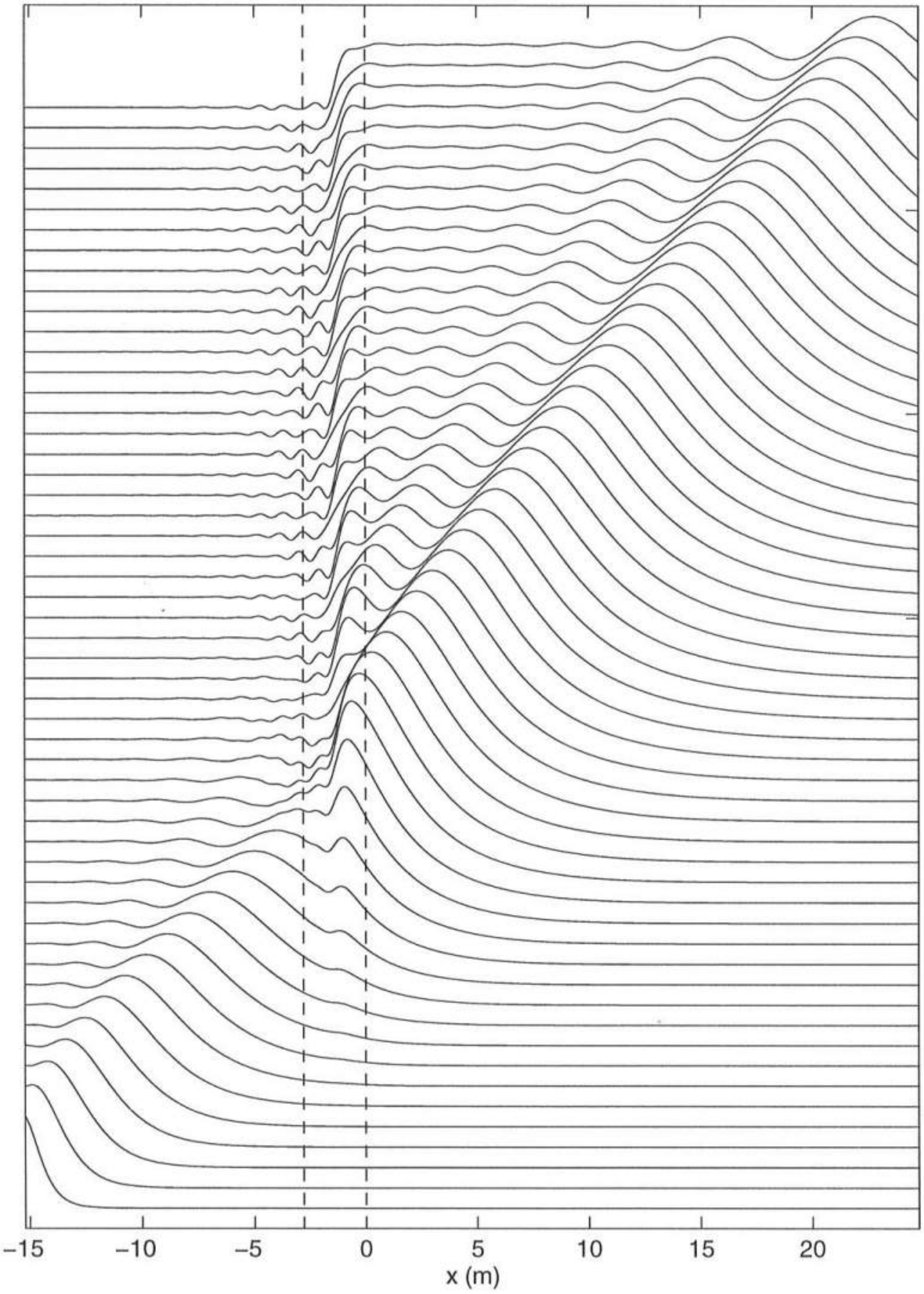

Figure 5.14: Snapshots of the spatial evolution of the wave envelope for a monochromatic wave using a 3 point filter (T = 1.2s,γ_f = 0.65)

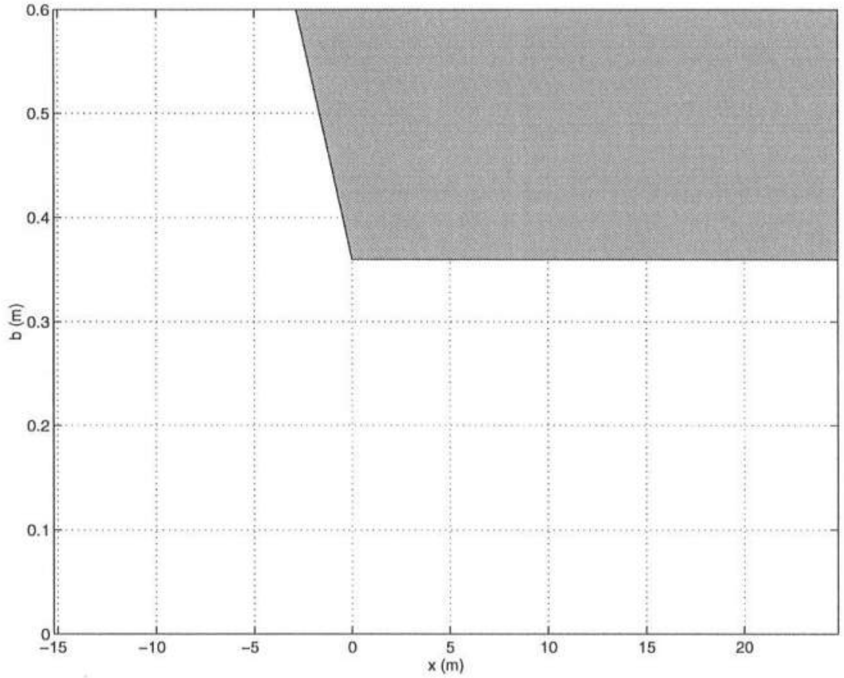

Figure 5.15: Numerical domain for comparisons with data. Depth is constant

(5.52) to predict the location of the blocking point. In the comparison between the model and breaking wave Test 4 (T = 1.2 s, H = 0.066 m) shown in Figure 5.17 this disparity is even larger. The model predicts blocking at the linear blocking point but the data shows that due to the larger wave amplitude the waves reach the maximum current without getting blocked. Beyond this point due to energy dissipation the waves continue to lose energy till the blocking point is reached much further inside the channel. The importance of non-linear dispersion in wave blocking was pointed out in Chapter 3, and the inability of the model to predict this effect is a fairly strong limitation of the model.

Numerical simulations of wave groups have been done for conditions corresponding to the wave group Test 6 shown in Figures 4.5 and 4.6 in Chapter 4. The groups in the model were constructed by modulating a carrier wave with T = 1.22 s. For the simulations we used $\Delta x = 0.05$ m and $\Delta t = 0.012$ s, which corresponds

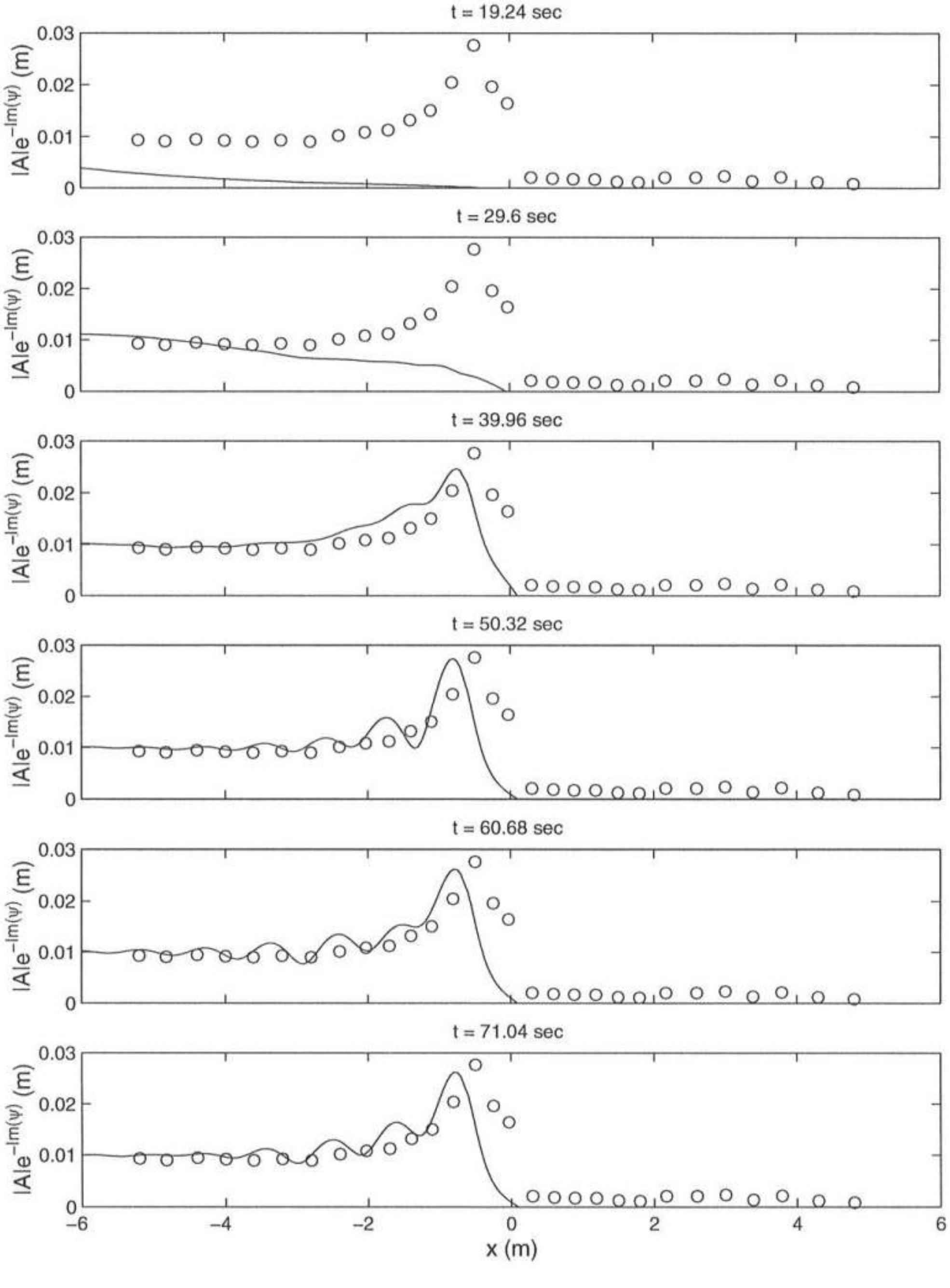

Figure 5.16: Model to data comparison of the amplitude envelope for a monochromatic wave (T = 1.2 s, H = 0.018 m)

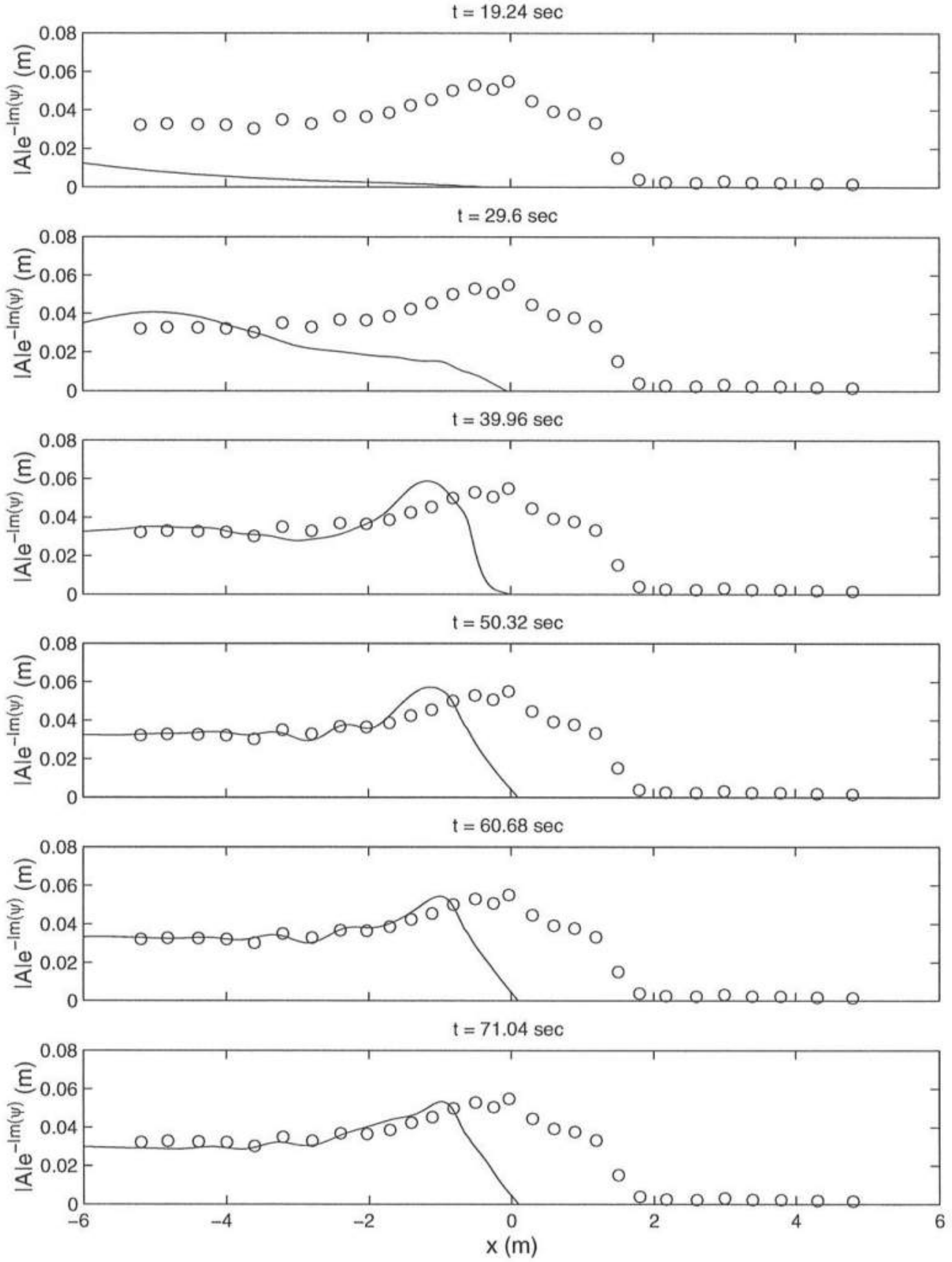

Figure 5.17: Model to data comparison of the amplitude envelope for a monochromatic wave (T = 1.2 s, H = 0.066 m)

to the sampling frequency at which the data was collected in the experiment. The time series of the surface elevation are shown in Figures 5.18 and 5.19, and the corresponding comparison of the amplitude envelopes with the data are shown in Figures 5.20 and 5.21. In the experiments the individual wave components of the wave group are blocked at their respective blocking points and the time series goes from being groupy to being monochromatic and then being completely blocked. In the model however the entire wave group gets blocked at the blocking point of the carrier frequency and there is no selective blocking as seen in the experiments. This limitation of the model to not separately block parts of the frequency spectrum also prevents the model to reproduce the experimental results of Test 6 in the monochromatic breaking wave experiments where the energy of the lower side band is not blocked (see Chapter 3).

Numerical simulations have also been conducted to simulate Test 6 of the wave packet experiments shown in Chapter 4. The wave packet in the model was created from a half-sine wave and it contained 8 waves. The wave period of the carrier wave was 1.22 s. A strong filter ($\gamma_f = 0.6$ and filtering every 5 time steps) was used to remove all the numerical instabilities. The time series of the data (see Figures 4.15 and 4.16 in Chapter 4) shows that the wave packets are reflected from the blocking point and close to the blocking point the incident wave packet and the reflected wave packets interact. In the model simulations shown in Figures 5.22 and 5.23 we also see a reflected wave packet. Though the numerical model has been developed only for the forward propagating root it is possible that close to the blocking point when the incident and reflected roots are very close to each other, the narrow banded spectrum around the incident root may capture the reflected root also. However it is not clear whether the reflected packet in the numerical results is the reflection from the blocking point or the backward propagation of numerical

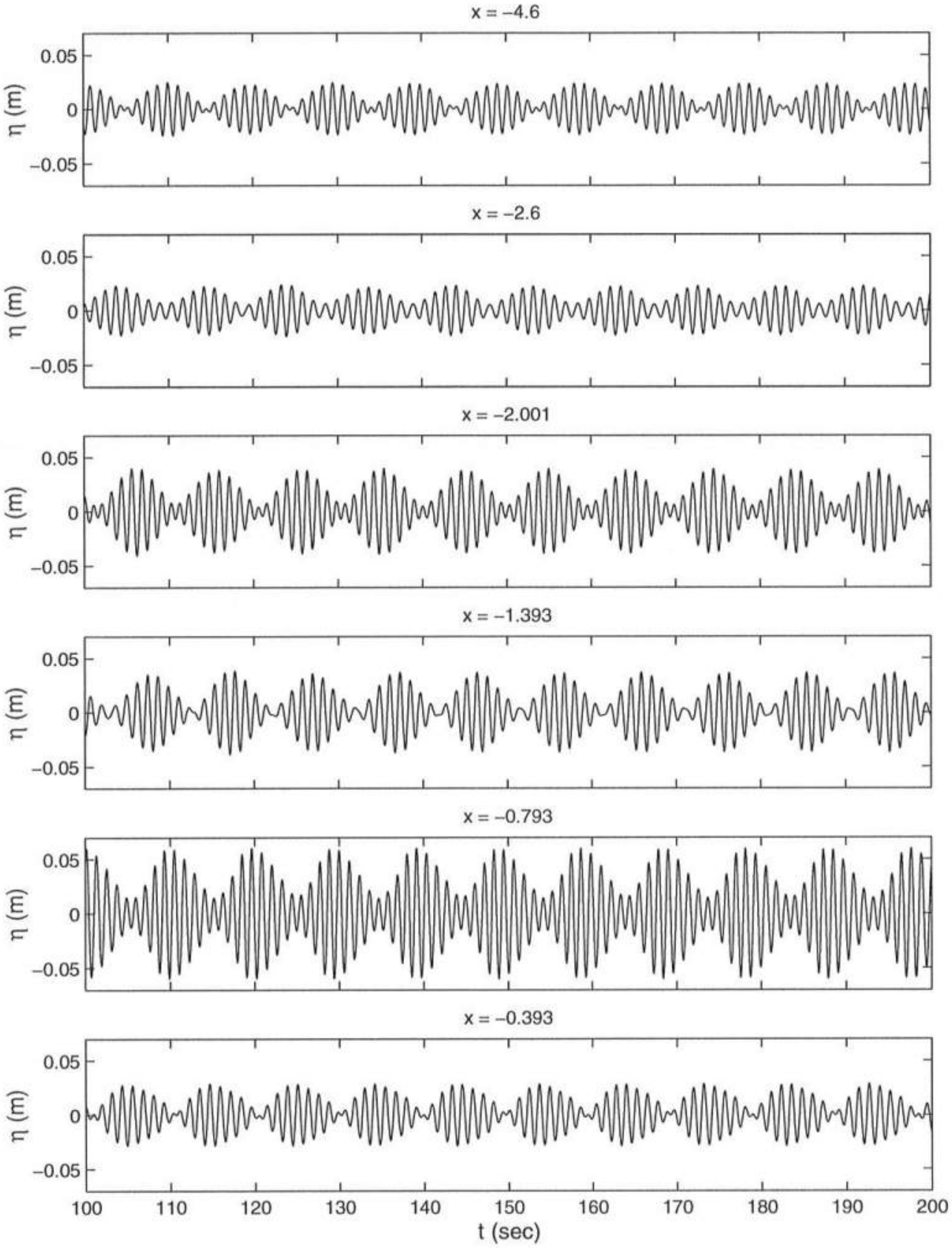

Figure 5.18: Time series of the model simulations of the surface elevation η at positions corresponding to the wave group data on Figure 4.5 in Chapter 4

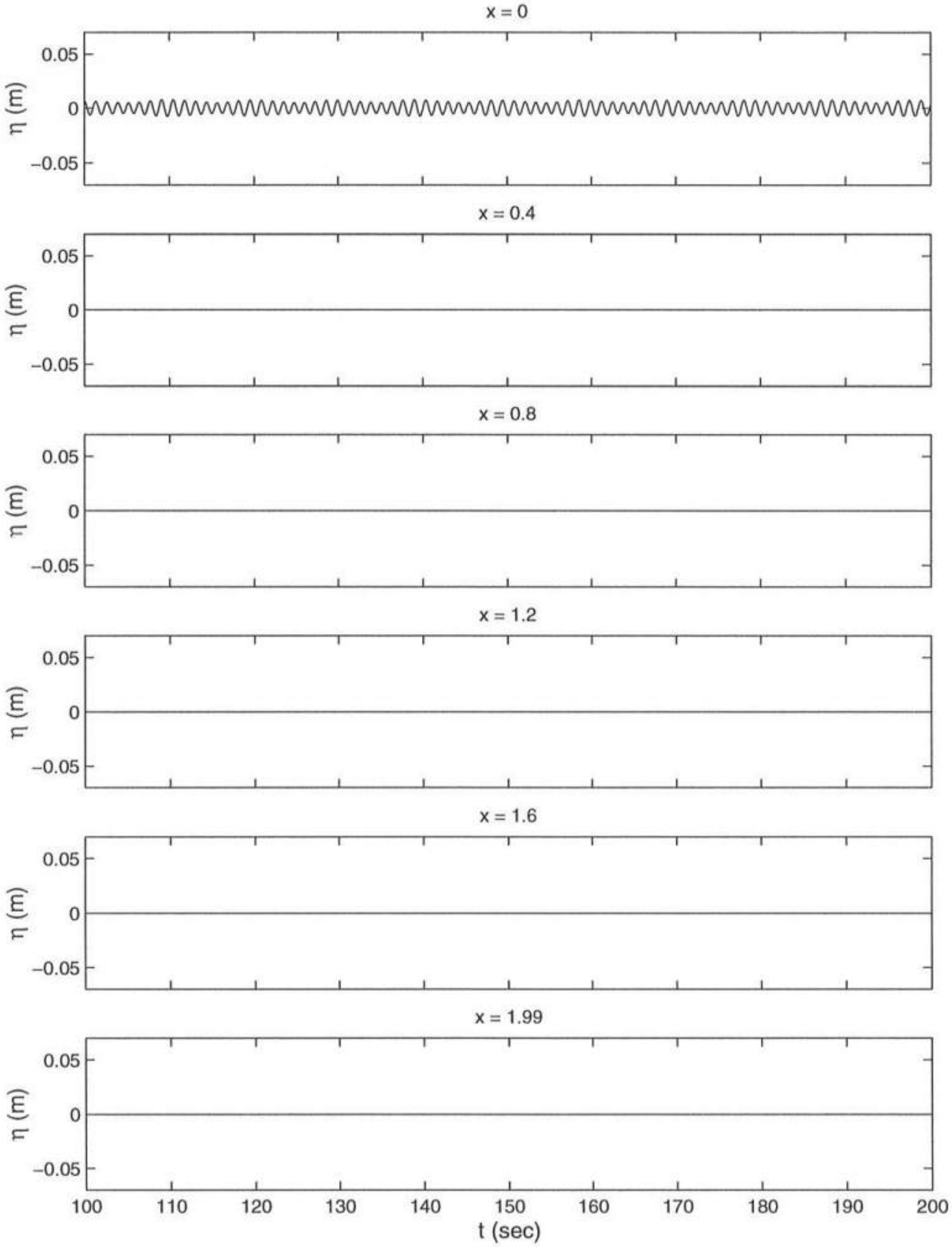

Figure 5.19: Time series of the model simulations of the surface elevation η at positions corresponding to the gage data on Figure 4.6 in Chapter 4

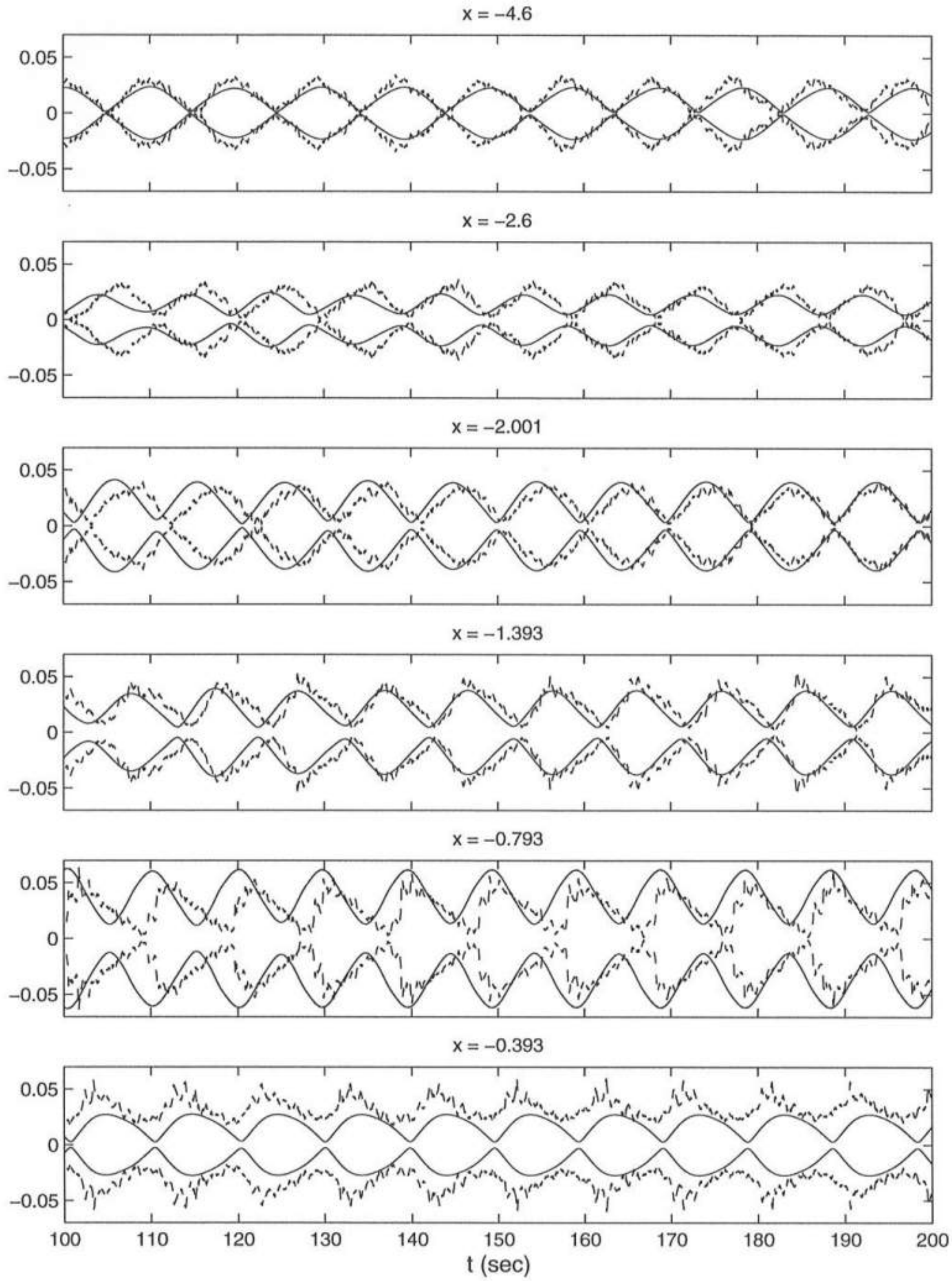

Figure 5.20: Model ('solid line') to data ('dashed line') comparisons of the amplitude envelope corresponding to the surface motion in Figures 5.18 and 4.5

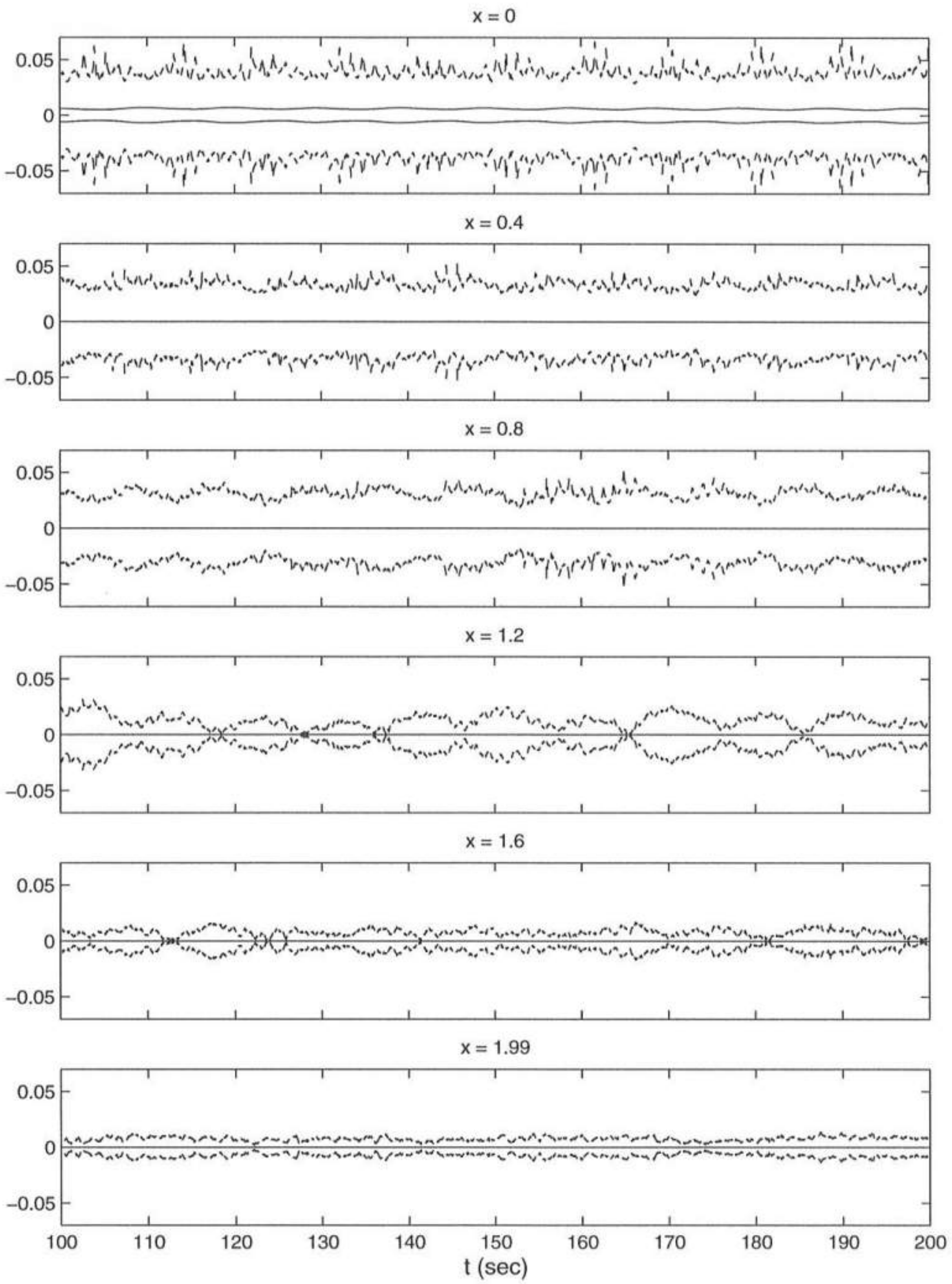

Figure 5.21: Model ('solid line') to data ('dashed line') comparisons of the amplitude envelope corresponding to the surface motion in Figures 5.19 and 4.6

instabilities. The separation distance between the incident and reflected wave packets at any particular gage location is greater in the experimental data as compared to model simulations because the blocking point in the experiments is further away from the wavemaker due to non-linear dispersion effects. The comparisons of the amplitude envelopes of the model and experimental data (Figures 5.24 and 5.25) shows that the actual blocking of the packet occurs later than predicted by the model.

5.5 Summary

A weakly non-linear model has been developed for the evolution of the envelope of a narrow-banded spectrum propagating in strong currents. The model has been developed for channels of varying width and depth. Beyond the blocking point, the roots of the dispersion relation branch out to give a pair of complex conjugate roots. Thus, the wave changes from a progressive periodic form to an exponentially damped form. Choosing the correct root leads to the decay of wave motion beyond the blocking point. In the absence of wave blocking and for a channel of constant width, our model can be reduced to the model of Turpin *et al.* (1983).

The model consists of a pair of coupled equations for the wave envelope and the long wave motion. Usually in the literature the long wave motion is integrated out to yield just a single equation. However, due to the complex nature of the coefficients this is not possible in our case and we have to solve a coupled system of equations. The numerical scheme consists of a BTCS scheme for the long wave equation and a Crank-Nicolson scheme for the envelope equation. Numerical tests on the propagation of a soliton have shown that the model works well. The governing envelope equation has two roots, one in which the wave energy is transported in the direction of propagation of the carrier wave, and a second spurious root in which the energy is transported in the opposite direction. In the uniform channel, the model

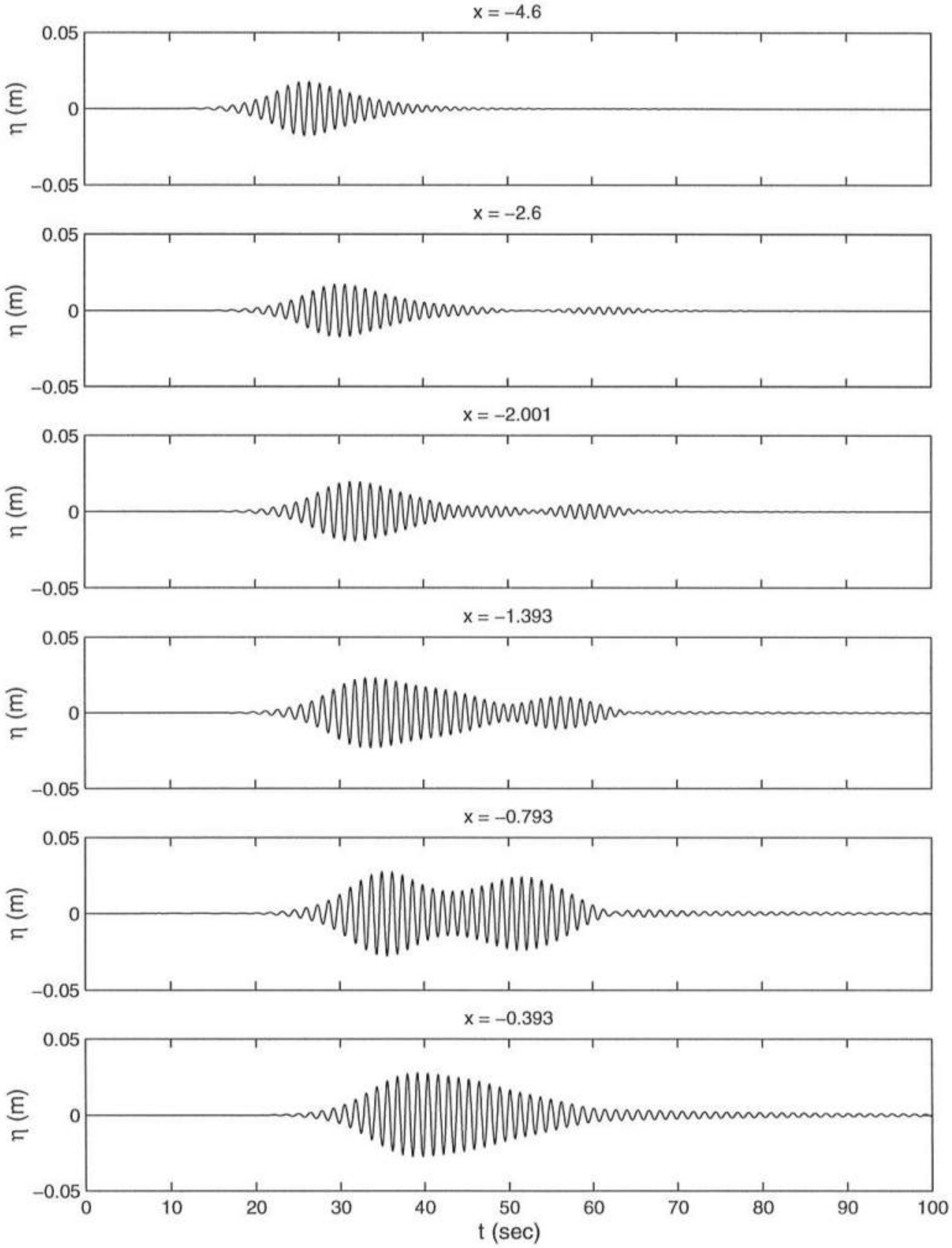

Figure 5.22: Time series of the model simulations of the surface elevation η at positions corresponding to the wave packet data on Figure 4.15 in Chapter 4

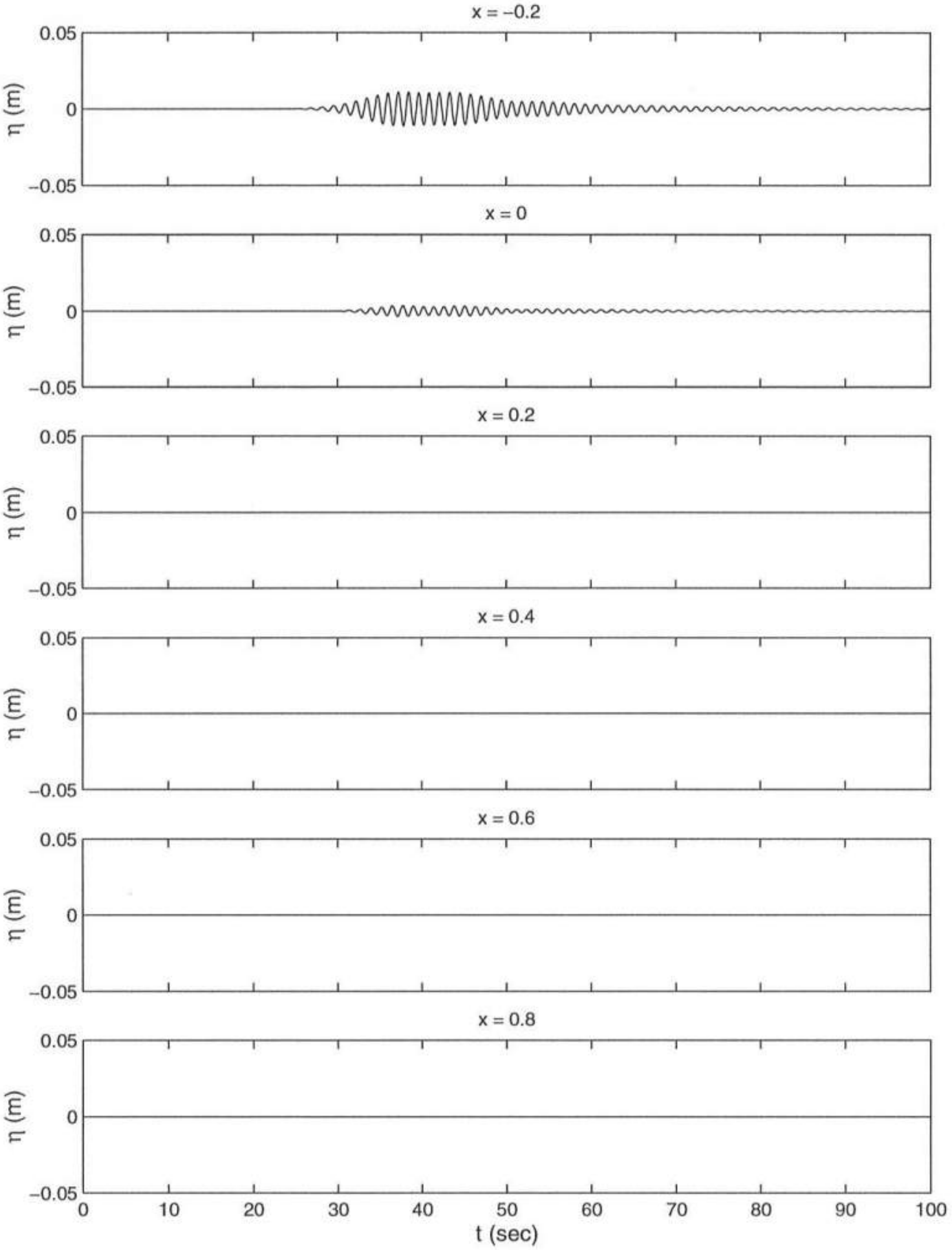

Figure 5.23: Time series of the model simulations of the surface elevation η at positions corresponding to the wave packet data on Figure 4.16 in Chapter 4

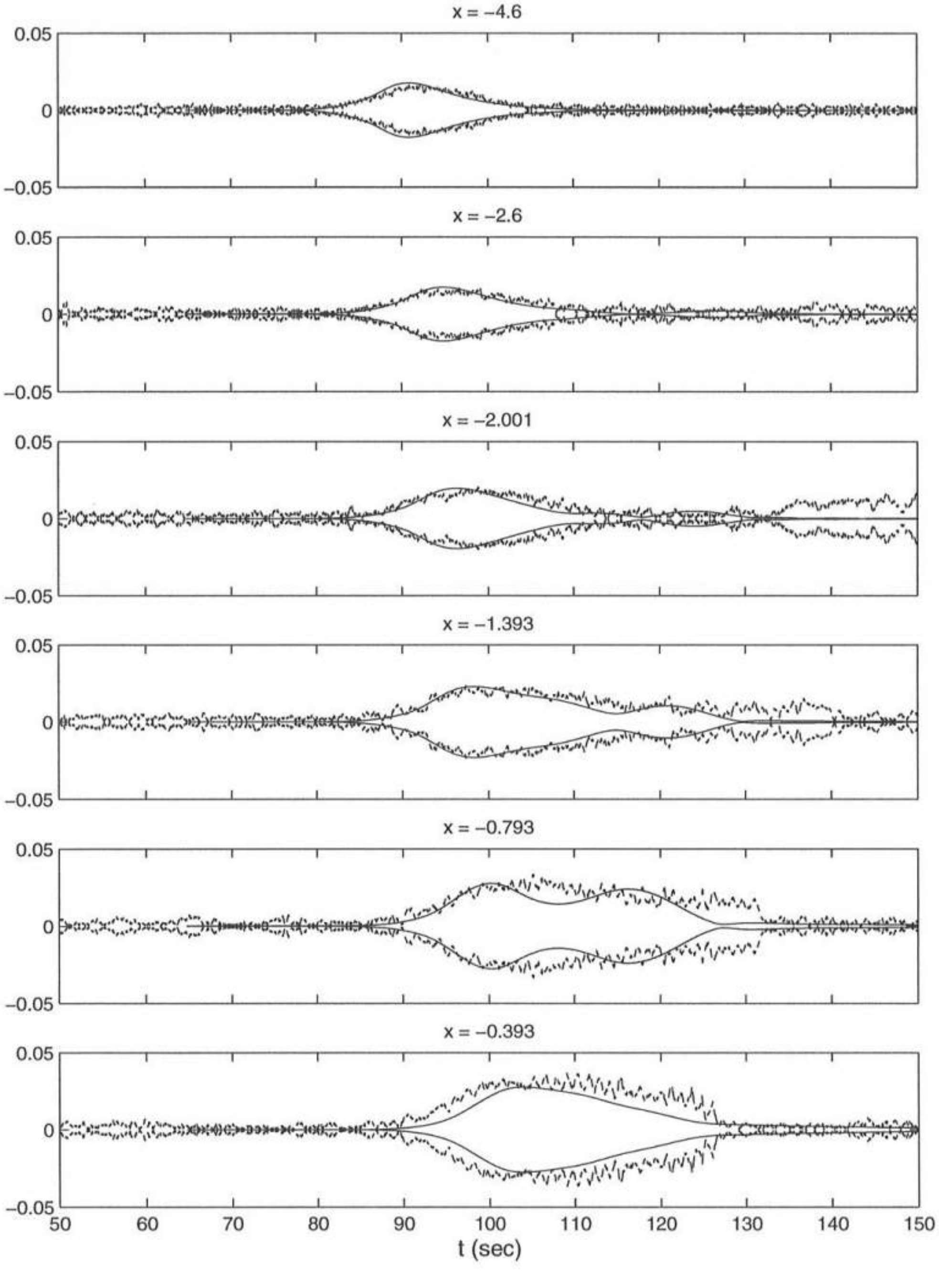

Figure 5.24: Model ('solid line') to data ('dashed line') comparisons of the amplitude envelope corresponding to the surface motion in Figures 5.22 and 4.15

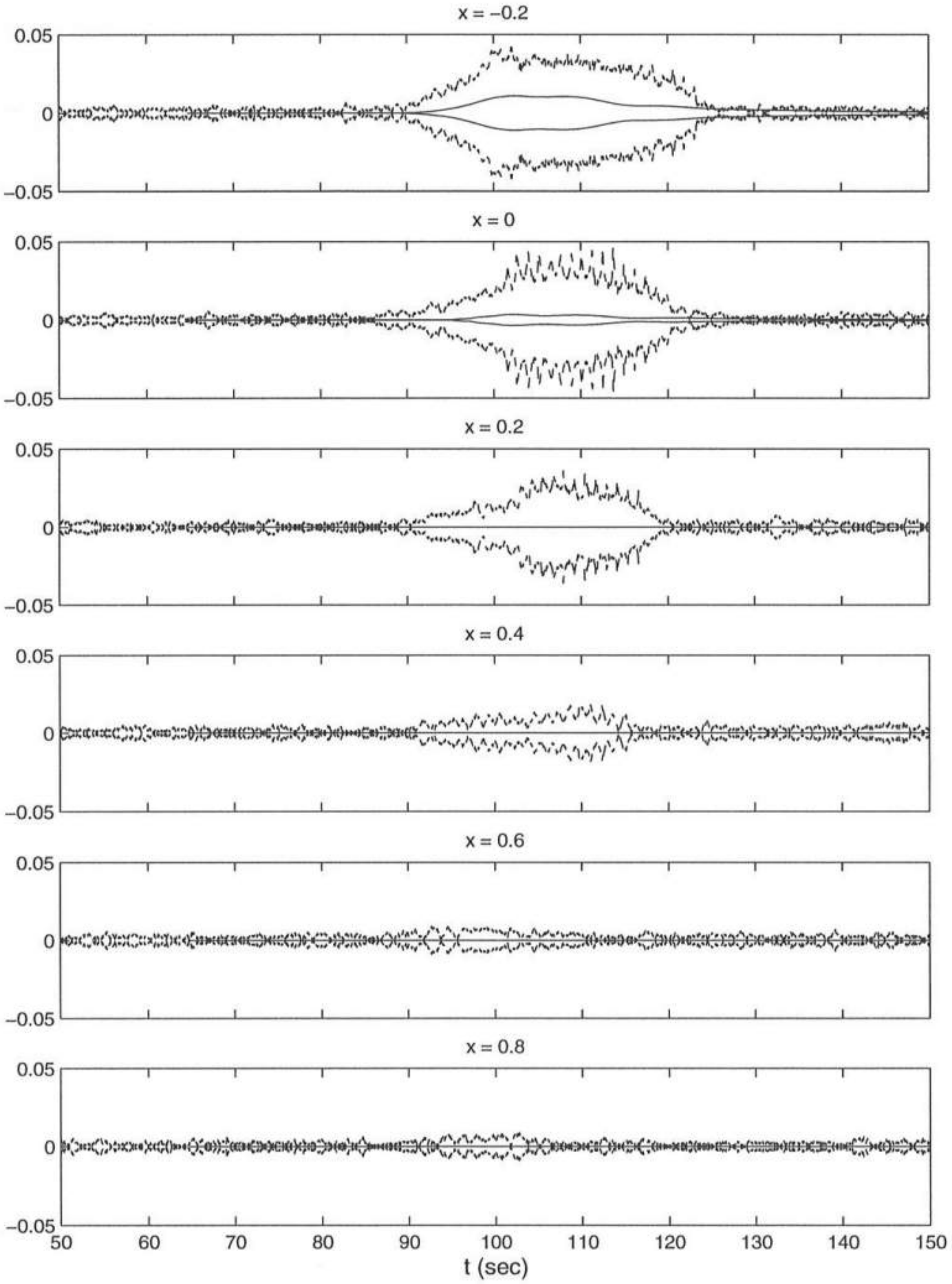

Figure 5.25: Model ('solid line') to data ('dashed line') comparisons of the amplitude envelope corresponding to the surface motion in Figures 5.23 and 4.16

picks up the correct root. However, within a rapid channel transition with increasing opposing current, the model is unstable. The strength of the instability grows with the rate at which the group velocity is decreasing and the disturbance is propagated backwards as the spurious root. To counteract the growth of the unstable mode a 3 point filter is used in the model.

The choice of the correct root to damp out the waves beyond the blocking point is not straightforward. The apparent choice is the wave number with the positive imaginary component, which will lead to decay of the surface wave amplitude for a fixed reference wave amplitude. However, the choice of this root actually causes the complex wave amplitude to increase exponentially with a faster rate than the decay of the carrier wave. Since the increase in the amplitude is greater than the decay due to the phase function, the overall solution will blow up. Therefore, the correct choice to simulate wave blocking is the root with the negative imaginary wave number.

When simulating wave blocking the model has a few major limitations. The first is that the model predicts the blocking point based on the linear dispersion relation and cannot account for non-linear effects. In the experimental results of Chapter 3 we saw that due to the sharp steepening of the waves prior to the blocking point, the non-linear terms in the dispersion relation become important and the linear dispersion relation does a poor job of predicting the position of wave blocking. The second major limitation of the model is that blocking occurs at the blocking point of the carrier wave. However experimental results both in the case of monochromatic waves (breaking wave tests Test 6) and the wave group tests show that this is not the case and that the individual wave components of the spectrum are blocked at their respective blocking points. This inability of the model to block the wave components of the spectrum separately means that the model is unable to simulate the propagation of the lower side bands even when the primary wave component and the upper side bands are blocked (monochromatic breaking wave tests Test 6, Figure 3.8 in Chapter 3).

Chapter 6

EXPERIMENTS ON RANDOM WAVES

6.1 Introduction

The evolution of wave spectra on a varying current was first studied by Huang *et al.* (1972), using the wave action conservation principle together with the doppler shifted dispersion relation. Tayfun *et al.* (1976) extended the analysis to finite depth and a directional wave spectrum. Experimental studies conducted by Hedges *et al.* (1985) showed that the model of Huang *et al.* (1972) overpredicted the spectral values in the high frequency range. Better comparison was obtained when they included an upper limit to which the waves were allowed to grow in any frequency band, using an equilibrium range constraint similar to the one used by Phillips (1977).

Sakai *et al.* (1986) conducted experimental studies on waves breaking in shallow water in the presence of opposing currents. Their studies showed that the opposing currents increased the energy decay due to breaking. The opposing current also led to larger increases in the significant wave period. However, their experimental studies were conducted in shallow water where the breaking process is dominated by depth limited breaking. Ris and Holthuijsen (1996) conducted numerical simulations of random waves being blocked by strong currents in deep water using a third-generation wave model. They tried to quantify the energy decay in due to current limited breaking with the experimental studies of Lai *et al.* (1989), with inconclusive results. Our experimental studies on monochromatic waves outlined in Chapter 3 have shown that under blocking conditions the waves exhibit a heirarchial behavior extending from wave reflection to prevention of blocking due to growth of side bands. In irregular waves all of these different physical processes are occurring together and it is not obvious if a monochromatic energy decay model can be used with irregular waves. Thus, in order to develop an empirical dissipation model for current-limited breaking in irregular waves a detailed experimental study on irregular waves has been conducted and shall be outlined in this present chapter. A version of this presentation also appears in Chawla and Kirby (1999b)

6.2 Experimental tests

The random wave experiments consisted of 20 spectral tests, the details of which are available in Chawla and Kirby (1999a). For each spectral test, gage measurements were done at 36 different locations in the flume. At each location the time series of the water surface was recorded at 50 Hz for 1000 sec. In all of the spectral tests there was wave breaking to some degree or other, thus, results from all of the tests shall be presented here.

The design spectrum for each of the tests was determined from a TMA spectrum. Due to wave blocking of high frequency components, the measured spectrum at the first gage ($x = -4.6$ m) does not correspond in shape to an equilibrium TMA spectrum (see Figures 6.1 and 6.2). The initial conditions are therefore determined from the measurements of the first gage. The spectra have been quantified in terms of the root-mean-square wave height H_{rms} and the average frequency $\bar{\omega}$.

$$\bar{\omega} \equiv 2\pi \frac{\int_0^\infty f S(f) df}{\int_0^\infty S(f) df} \tag{6.1}$$

The parameters for the tests are given in Table 6.1. Larger values of H_{rms} were not used because it led to breaking of the higher waves at the wave paddle itself.

Table 6.1: Parameters for Random wave tests (determined at $x = -4.6$ m).

Test No.	$\bar{\omega}$ sec^{-1}	H_{rms} m
1	5.81	0.026
2	5.68	0.033
3	5.40	0.042
4	5.33	0.045
5	5.35	0.026
6	5.24	0.034
7	5.07	0.047
8	5.03	0.057
9	5.07	0.033
10	4.96	0.046
11	4.85	0.059
12	4.80	0.068
13	4.90	0.033
14	4.76	0.044
15	4.70	0.058
16	4.63	0.070
17	4.60	0.027
18	4.45	0.040
19	4.39	0.052
20	4.28	0.062

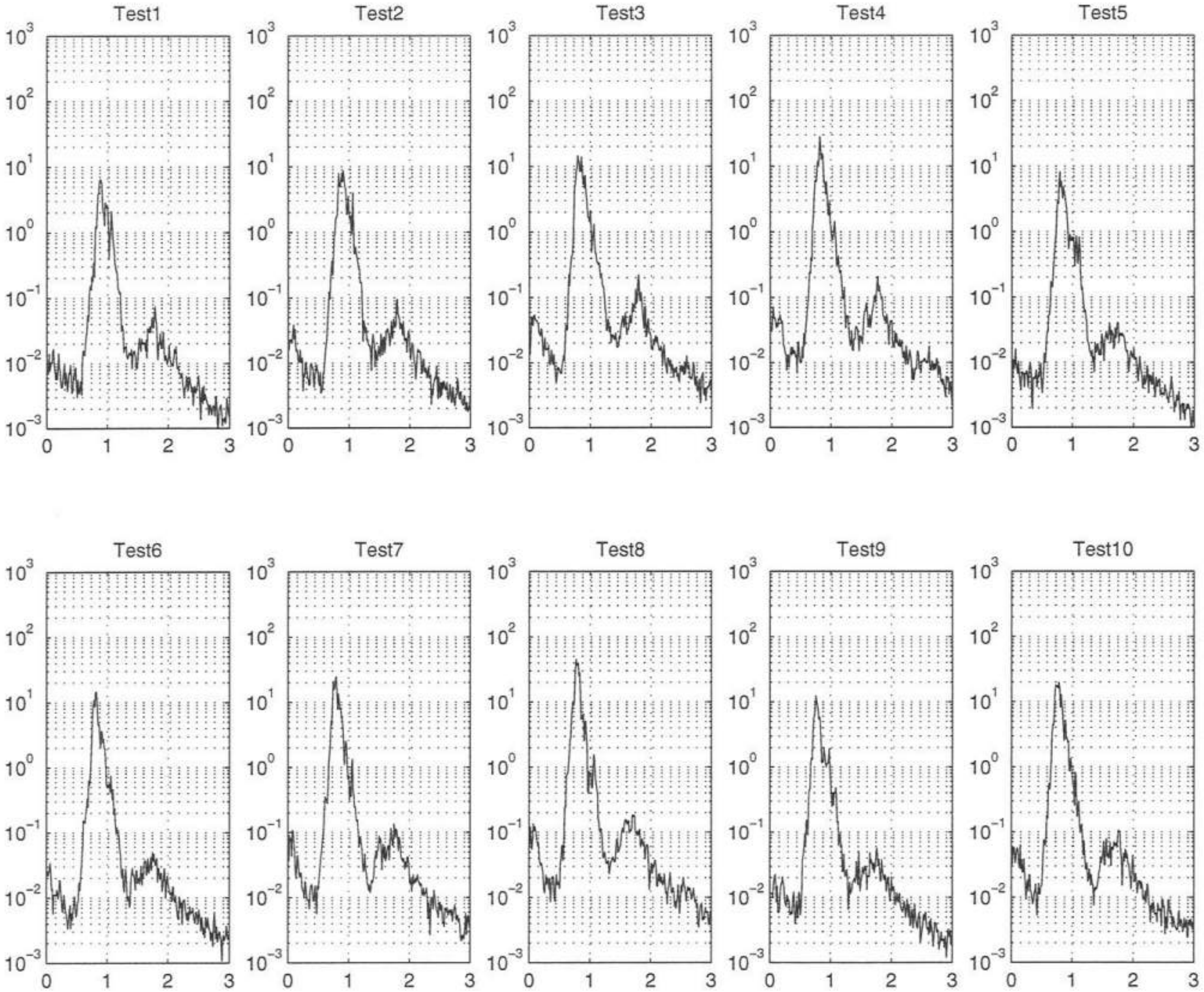

Figure 6.1: Energy spectra at the first gage (Tests $1 - 10$).

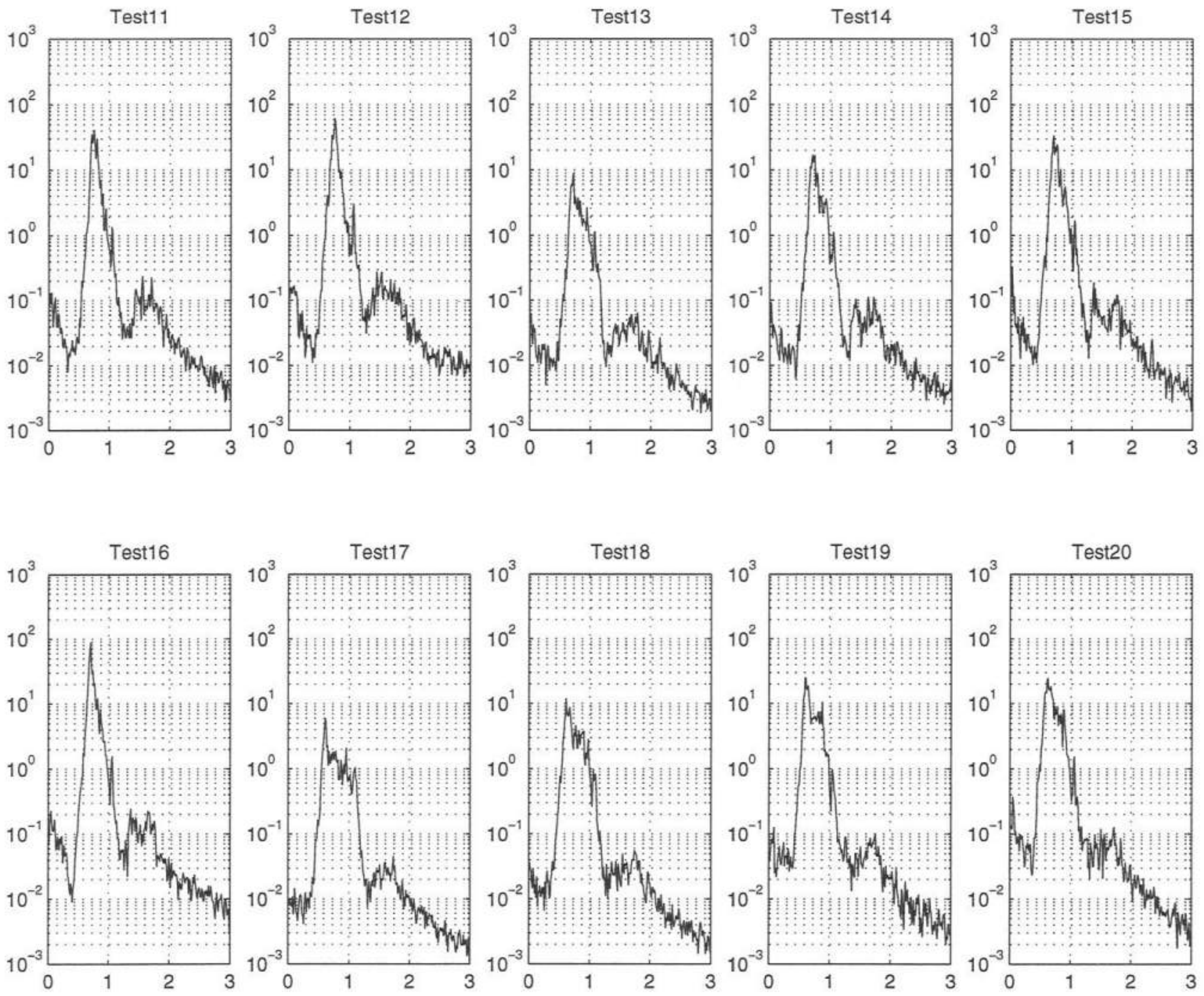

Figure 6.2: Energy spectra at the first gage (Tests $11-20$).

6.3 Bulk dissipation formula

Before developing a numerical model for random waves, we need to determine a bulk dissipation formula for random waves breaking on opposing currents. Similar to the monochromatic wave problem, we shall use a previous method for determining bulk dissipation in depth limited wave breaking as a guideline to solve for a bulk dissipation formula for current limited wave breaking. The approach followed here will be the one outlined in Thornton and Guza (1983).

The basic assumption is that the energy dissipation in any individual breaking wave is given by the bore model (see eqn. (3.8)). The bulk energy dissipation due to all the breaking waves is then given by

$$< D >= \int_0^\infty D(H)P_b(H)dH \tag{6.2}$$

where $P_b(H)$ is the probability distribution of wave height of the broken waves and is unknown. D is the energy dissipation in the breaking wave and is given by

$$D = -\beta_r \frac{\rho}{8\pi}\left(\sqrt{\frac{(g\bar{k})^3}{\tanh \bar{k}h}}\right) H^3 \tag{6.3}$$

Eqn. (6.3) is similar to (3.8), except that we use an average wavenumber $\bar{k}$ corresponding to $\bar{\omega}$ and a different scaling parameter β_r which depends upon the energy dissipation in the waves.

An empirical expression for $P_b(H)$ can be obtained from experimental data. In order to do so, we must first be able to separate the breaking waves from the non-breaking waves in any given time series.

6.3.1 Geometric criterion for broken waves

A geometric criterion is used to separate out the breaking and non-breaking waves in a time series. This criterion was first proposed by Longuet-Higgins and Smith (1983) and later modified by Xu *et al.* (1986).

The method consists of dividing the time series into individual wave components using the zero-upcrossing method. For each wave component we then determine

$$R = |\frac{\partial \eta}{\partial t}| \approx |\frac{\Delta \eta}{\Delta t}| \tag{6.4}$$

Using the non dispersive wave equation

$$\frac{\partial \eta}{\partial t} + c\frac{\partial \eta}{\partial x} = 0$$

we get

$$R \approx |c\frac{\Delta \eta}{\Delta x}|$$

where c is the phase speed of the wave component determined using linear theory. Now

$$\frac{\Delta \eta}{\Delta x} \approx \tan \alpha$$

where $\tan \alpha$ is the wave slope. Longuet-Higgins and Fox (1977) showed that

$$\tan \alpha = 0.586$$

is the limiting slope for waves. Thus, a wave is breaking if

$$R_{max} \geq 0.586c \tag{6.5}$$

where R_{max} is the maximum value of R determined from (6.4). Eqns (6.5) together with (6.4) provide a geometric criterion to determine breaking waves from a time series. The criterion is so called because it is based on the maximum slope of the waves. The biggest disadvantage with using this method is that some of the waves start breaking earlier and continue to break as they pass over the gage, but by then

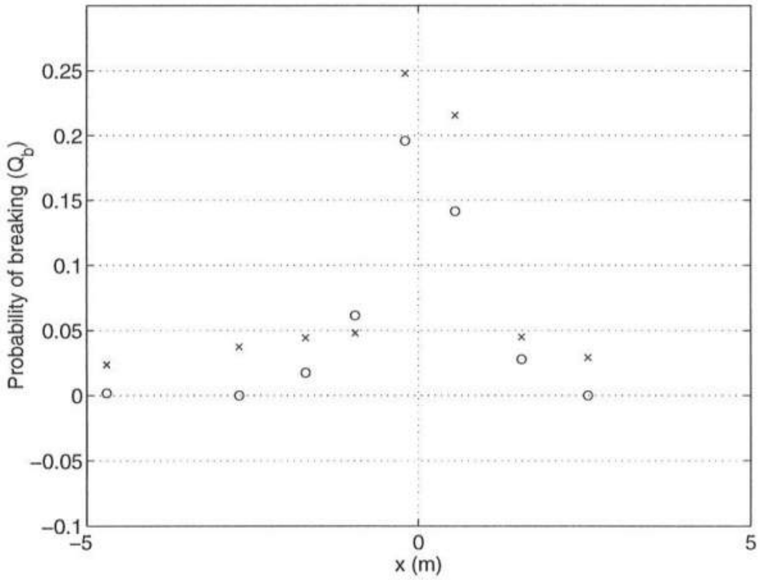

Figure 6.3: Probability of breaking Q_b as a function of x ('∘' geometric method;'×' actual measured)

their slope has reduced considerably. The method cannot distinguish between these breaking waves and unbroken waves with small slopes.

To test the method, an experiment was conducted in which the time series of breaking random waves was recorded at 8 different locations in the tank. Observers were placed in front of each gage with a counter to record the broken waves passing over the gages. The comparison between the probability of breaking (fraction of breaking waves) determined with the help of visual observations and the geometric method is shown in Figure 6.3. The discrepancies occur due to the errors in visual observations and the inability of the method to distinguish between broken and unbroken waves of small slope. Nevertheless, the qualitative pattern of the probability of breaking is reproduced reasonably well by the geometric method, and complete agreement is not so important as the bulk dissipation formula shall be scaled by a non-dimensional parameter. Thus, the method shall be used to develop an empirical formula for the probability of breaking.

6.3.2 Probabilistic distribution function for broken waves

An empirical formulation of the probabilistic wave height distribution of the broken waves is determined with the help of the experimental data. Figure 6.4 shows the pdf of broken and unbroken waves at $x = 0$, for 6 different tests. The solid line is the Rayleigh distribution. From the figure it is clear that the wave height distribution of the broken waves is a subset of the Rayleigh distribution and is skewed towards larger values of the wave heights. Thus, the pdf for broken waves can be given by

$$P_b(H) = W(H)P_r(H) \tag{6.6}$$

where $P_b(H)$ is the pdf of the broken waves, $W(H)$ is a weighting function to be determined, and $P_r(H)$ is the Rayleigh wave height distribution given by

$$P_r(H) = \frac{2H}{H_{rms}^2}\exp\left(-\left(\frac{H}{H_{rms}}\right)^2\right) \tag{6.7}$$

H_{rms} is the root-mean-square wave height.

The weighting function $W(H)$ has to be skewed towards larger values of wave height. Also, the proportion of waves breaking must increase with stronger opposing currents. Since waves tend to steepen on the stronger currents, a wave slope criterion is proposed for the weighting function

$$W(H) = \left[\frac{\bar{k}H_{rms}}{\gamma_r \tanh \bar{k}h}\right]^2 \left\{1 - \exp\left(-\left(\frac{\bar{k}H}{\gamma_r \tanh \bar{k}h}\right)^2\right)\right\} \tag{6.8}$$

where γ_r is a parameter to be determined and $\bar{k}$ is the wave number corresponding to $\bar{\omega}$. The terms in the curly bracket skew the wave height distribution to larger wave heights.

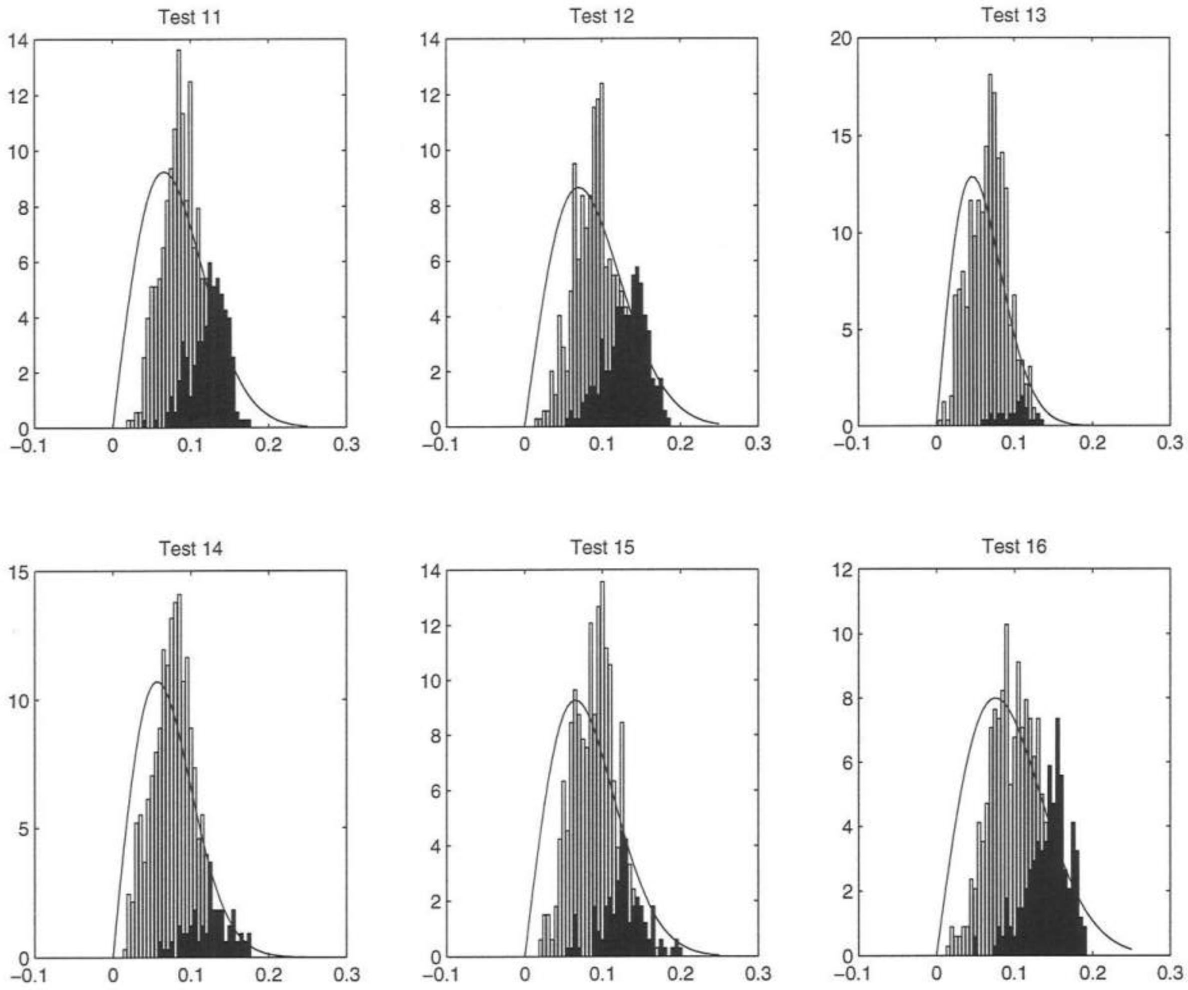

Figure 6.4: Probability distribution of broken (solid bars) and unbroken waves (open bars) for different tests at $x = 0$ ('solid line' Rayleigh distribution).

Substituting (6.8) and (6.7) in (6.6), we get an expression for $P_b(H)$ as

$$
\begin{aligned}
P_b(H) =& 2H\left(\frac{\bar{k}}{\gamma_r \tanh \bar{k}h}\right)^2 \exp\left(-\left(\frac{H}{H_{rms}}\right)^2\right)\Bigg\{1 \\
& - \exp\left(-\left(\frac{H}{H_{rms}}\right)^2\left(\frac{\bar{k}H_{rms}}{\gamma_r \tanh \bar{k}h}\right)^2\right)\Bigg\}
\end{aligned}
\tag{6.9}
$$

Figure 6.5 gives the comparison between the pdf of broken waves and the empirical function given in (6.9). The probability of breaking Q_b can then be given by

$$
Q_b = \int_0^\infty P_b(H)dH \tag{6.10}
$$

The value of γ_r is fixed by comparing the probability of breaking obtained from (6.10) and (6.9) and the probability of wave breaking obtained from the experimental data. These comparisons are shown in Figures 6.6 and 6.7 as a function of x for $\gamma_r = 0.6$.

Substituting (6.9) and (6.3) in (6.2) and solving we get

$$
\begin{aligned}
< D > =& \frac{-3\beta_r \rho}{32\sqrt{\pi}}\sqrt{\frac{(g\bar{k})^3}{\tanh \bar{k}h}}\left(\frac{\bar{k}}{\gamma_r \tanh \bar{k}h}\right)^2 H_{rms}^5 \Bigg[1 \\
& - \left\{1 + \left(\frac{\bar{k}H_{rms}}{\gamma_r \tanh \bar{k}h}\right)^2\right\}^{-5/2}\Bigg]
\end{aligned}
\tag{6.11}
$$

In shallow water, where $\tanh \bar{k}h \rightarrow \bar{k}h$, (6.11) reduces to the expression obtained by Thornton and Guza (1983). It should be mentioned that we could have chosen a different form for $P_b(H)$ to give a better comparison with the distribution of broken waves but the subsequent expression for bulk energy dissipation would have been very complex. We would also lose the added advantage of (6.11) reducing to the depth limited form of Thornton and Guza (1983) in shallow water.

6.4 Numerical Model

Using the wave action conservation principle together with an expression for the bulk energy dissipation, two simple numerical models are used. Since we have

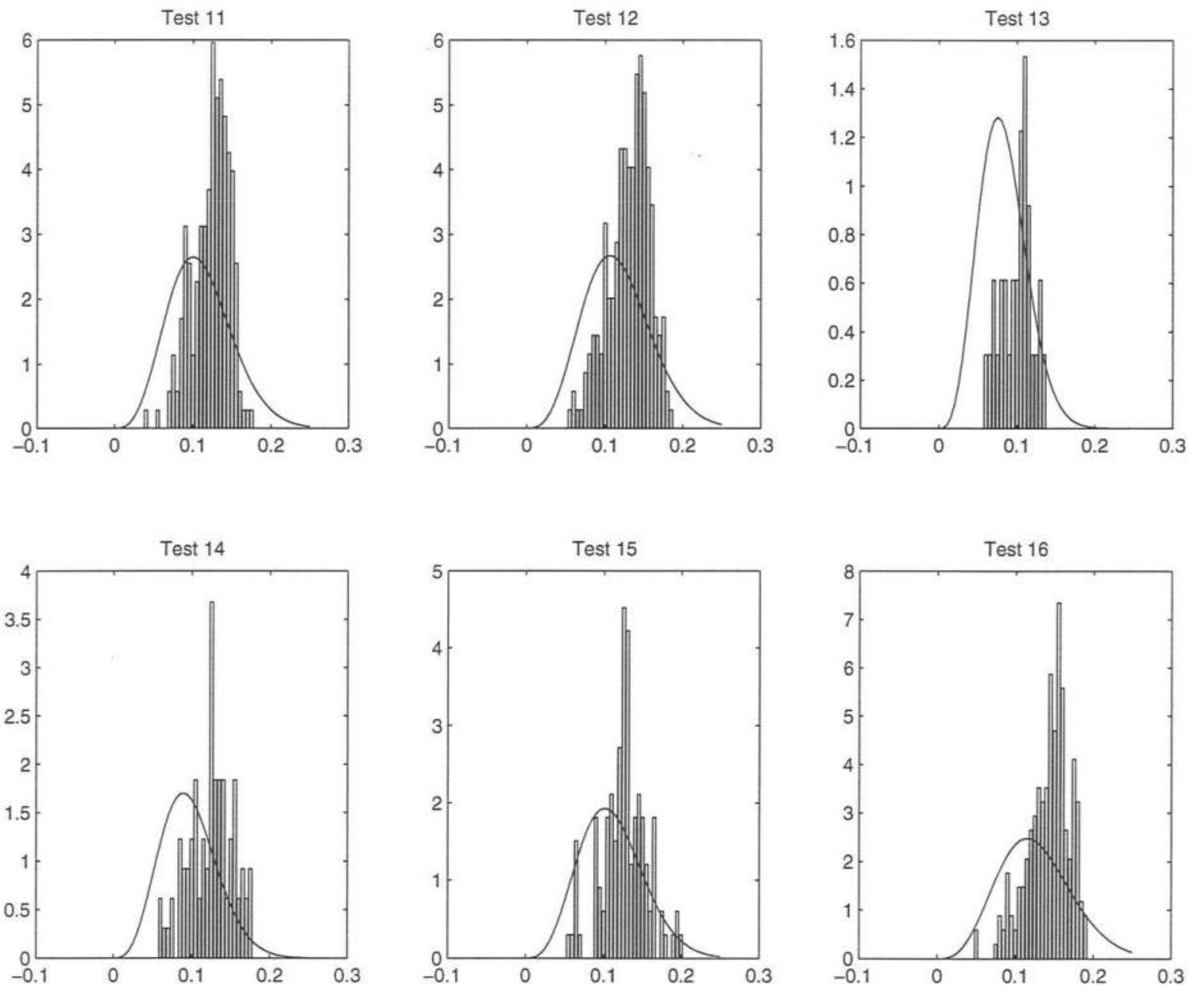

Figure 6.5: Probability distribution of broken waves (open bars) for different tests at $x = 0$. 'solid line' $P_b(H)$ given by (6.9).

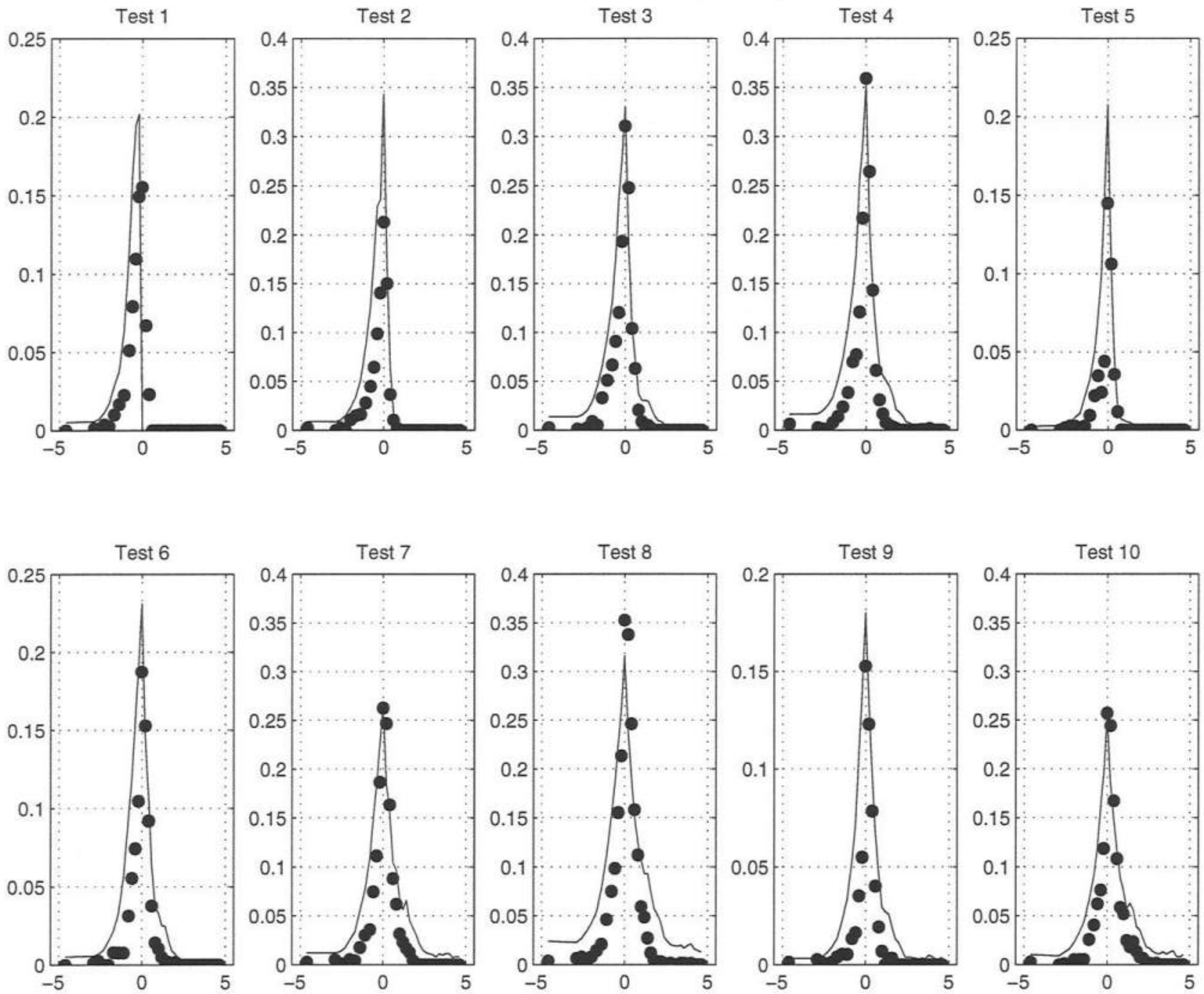

Figure 6.6: $Q_b(x)$ for different tests ('•' Geometric method;'−' Empirical pdf).

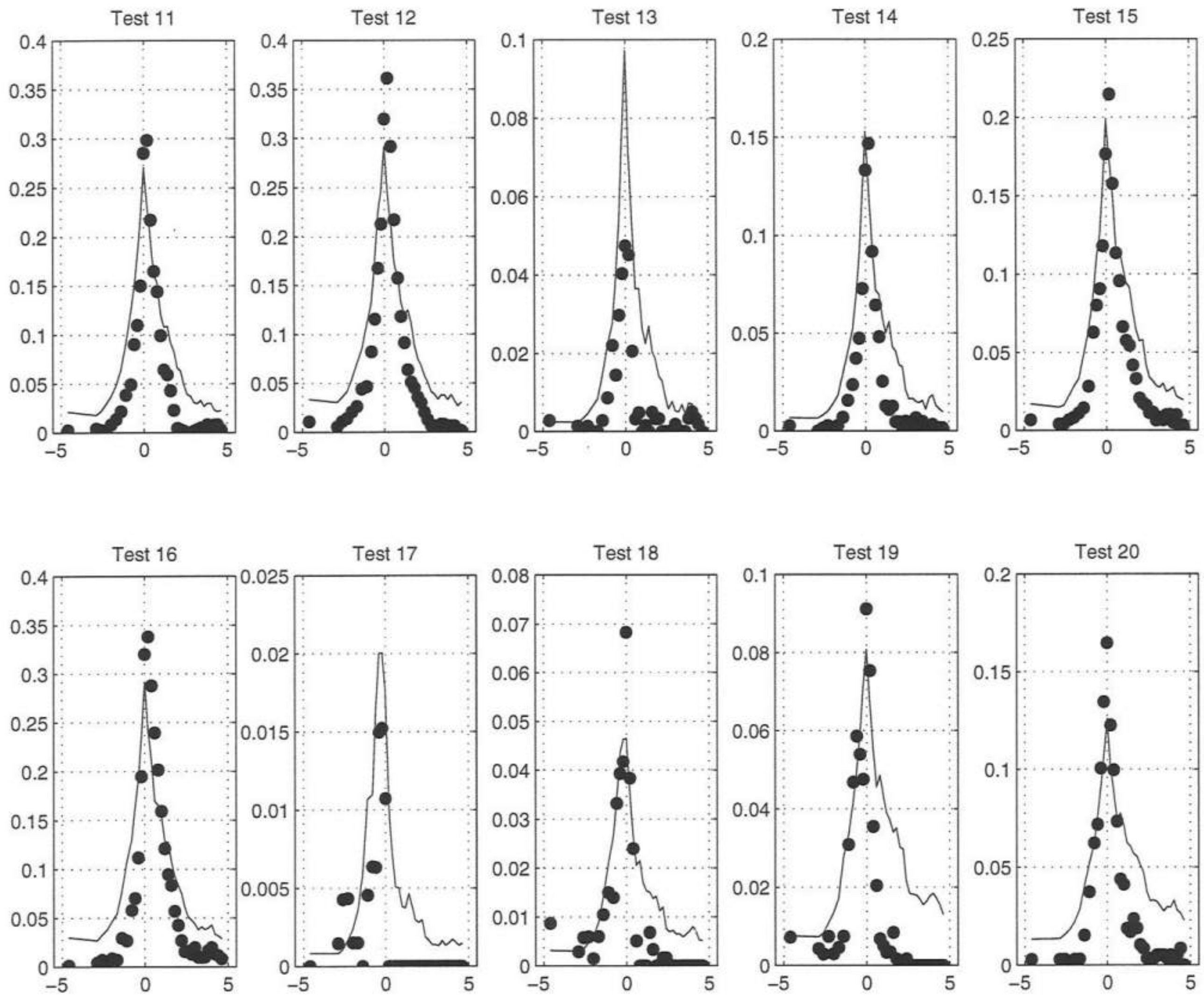

Figure 6.7: $Q_b(x)$ for different tests ('•' Geometric method;'–' Empirical pdf).

already seen from the monochromatic tests that amplitude dispersion effects are important, a non-linear dispersion relation is used in both the models. H_{rms} is used to quantify the amplitude dispersion effects.

6.4.1 Bulk wave action conservation model

In this model the individual spectrum is described by its bulk quantities, and then modeled as a monochromatic wave, but using the bulk dissipation formula for wave breaking. The governing equation is given by

$$\frac{1}{b}\left[\frac{\partial}{\partial x}\left(\frac{bE_{rms}\bar{C}_{ga}}{\bar{\sigma}}\right)\right] = \frac{< D >}{\bar{\sigma}} \tag{6.12}$$

where E_{rms} is the wave energy corresponding to H_{rms}. $\bar{C}_{ga}$ and $\bar{\sigma}$ are the group velocity and intrinsic wave frequency associated with the average frequency $\bar{\omega}$.

The problem with this model is that we specify an $\bar{\omega}$ in the initial conditions which characterizes the spectrum. In the model this $\bar{\omega}$ remains fixed as the random waves progress into stronger currents. But in reality as the spectrum moves into stronger currents, more of the higher frequency components get blocked and subsequently $\bar{\omega}$ shifts down. We thus do not expect the model to perform very well, particularly in regions where a large part of the spectrum is blocked.

6.4.2 Spectral Model

A second model is used to account for the limitations of the first model. In this approach the entire spectrum is modeled and not just its bulk quantities. The model involves dividing the frequency spectrum into N equally spaced bins, and representing the energy in each bin by a monochromatic wave. The governing equation for the i^{th} wave component is then given by

$$\frac{1}{b}\left[\frac{\partial}{\partial x}\left(\frac{bE_i(C_{ga})_i}{\sigma_i}\right)\right] = \frac{\delta_i}{\sigma_i} \tag{6.13}$$

where δ_i represents the energy dissipation in each frequency component due to wave breaking.

The advantage of having spectral information is that we can empirically adjust δ_i so that the higher frequency components have greater energy dissipation. The expression used for δ_i is given by

$$\delta_i = \alpha E_i \left(\frac{\sigma_i}{\bar{\sigma}}\right)^4 \tag{6.14}$$

where α is a coefficient. The terms in the brackets were raised to the 4th power because that gave reasonably good extimates of the spectrum. Since the total energy dissipation from all the wave components is given by $< D >$, we get

$$\alpha = \frac{< D >}{\sum_{i=1}^{N} E_i \left(\frac{\sigma_i}{\bar{\sigma}}\right)^4} \tag{6.15}$$

Eqns. (6.13) together with (6.14), (6.15) and (6.11) make up the spectral model. The advantage of this model as compared to the bulk conservation model is that individual frequency components can be tracked separately, and we can simulate spectral quantities like $\bar{\omega}$ more accurately. The disadvantage is that it is computationally more intensive.

6.5 Comparisons with data

The parametric values of β_r and γ_r in the two models were arbitrarily fixed at 0.4 and 0.6 respectively. In the spectral model 100 energy bins were used. For the spectral comparisons, the energy spectra from the gage measurements was Bartlett averaged with 24 degrees of freedom ($\Delta f = 0.012$). The H_{rms} comparisons are shown in Figures 6.8 and 6.9. The disadvantages of representing an entire spectrum by just one component are seen in Tests $7 - 13$ where only a part of the spectrum is blocked. The energy dissipation in the bulk model also tends to be greater because of the inability to predict the down shift in $\bar{\omega}$ (see Figures 6.10 and 6.11). In the case of Test 17 wave breaking criterion are barely met and the energy dissipation is too subtle to be modeled with any degree of accuracy by the empirical model. Overall the bulk dissipation formula for random waves breaking on a current works reasonably well. There are a few discrepancies between data and spectral model predictions of $\bar{\omega}$ for the higher energy cases. These are probably due to nonlinear effects.

The evolution of the spectrum and the comparison with the spectral model for one of the tests is shown in Figure 6.12. The spectral model simulates the spectrum reasonably well, except in the narrow channel where the high frequency components are underpredicted. Figures 6.13 and 6.14 show the spectral comparisons between model results and data at the last gage ($x = 4.6$ m) for all the tests. The spectrum of the first gage has also been plotted to show the down shift more clearly.

We thus find that a probability of breaking criterion based on the wave slope together with a bore dissipation model works reasonably well in simulating energy dissipation in random waves. Another criterion which was based on wave slope was given by Battjes and Janssen (1978). Though their model was derived for depth limited wave breaking, we should be able to use their model with a few modifications to simulate current limited wave breaking. They state that all the waves breaking at any given point have a wave height H_{max}, which is the maximum wave height. For the current limited breaking cases we shall denote this by

$$H_{max} = \frac{\gamma_r}{\bar{k}} \tanh \bar{k}h \tag{6.16}$$

which is very similar to the breaking criterion used for monochromatic waves (see eqn. (3.9). They then determined an expression for the probability of breaking (Q_b) in terms of a transcendental equation using a Rayleigh distribution.

$$\frac{1 - Q_b}{\ln Q_b} = -\left(\frac{H_{rms}}{H_{max}}\right)^2 \tag{6.17}$$

Using the bore dissipation model the energy dissipation is then given by

$$D_{bj} = -\beta_r Q_b \frac{\rho}{8\pi} \left(\sqrt{\frac{(g\bar{k})^3}{\tanh \bar{k}h}} \right) H_{max}^3 \tag{6.18}$$

Using the same parametric values and the spectral model formulation, the comparison between the present bulk dissipation formula given by (6.11), and the Battjes and Janssen dissipation formula given by (6.18) are shown in figures 6.15 and 6.16. Both the formulae give very similar results.

6.6 Summary

A series of experiments of random waves have been conducted to study energy dissipation due to wave breaking under conditions of strong opposing currents. Comparison with data has shown that just like in the case of monochromatic waves (Chapter 3), a modified bore dissipation model works very well. The modified model uses a wave slope criterion instead of the standard wave height to water depth ratio that is used for shallow water breaking. The Battjes and Janssen (1978) model which also uses a wave slope criterion to determine breaking compares very well with the data also. As random waves propagate into stronger opposing currents, the frequency spectrum down shifts considerably due to the blocking of higher frequency components. This down shift can be accurately modeled with a spectral model.

A puzzling feature of our current-limited breaking models has been that the parametric coefficient β which is used to characterize the energy dissipation has different values for monochromatic and random waves (0.1 and 0.4 respectively). This is unlike the depth-limited breaking models (Thornton and Guza, 1983; Battjes and Janssen, 1978). A probable reason for the disparity could be that in our tests the current is not monotonically increasing and reaches a maximum in the narrow part of the channel. The waves thus do not continue breaking as they propagate into the channel. This effect is accounted for in the random wave model because

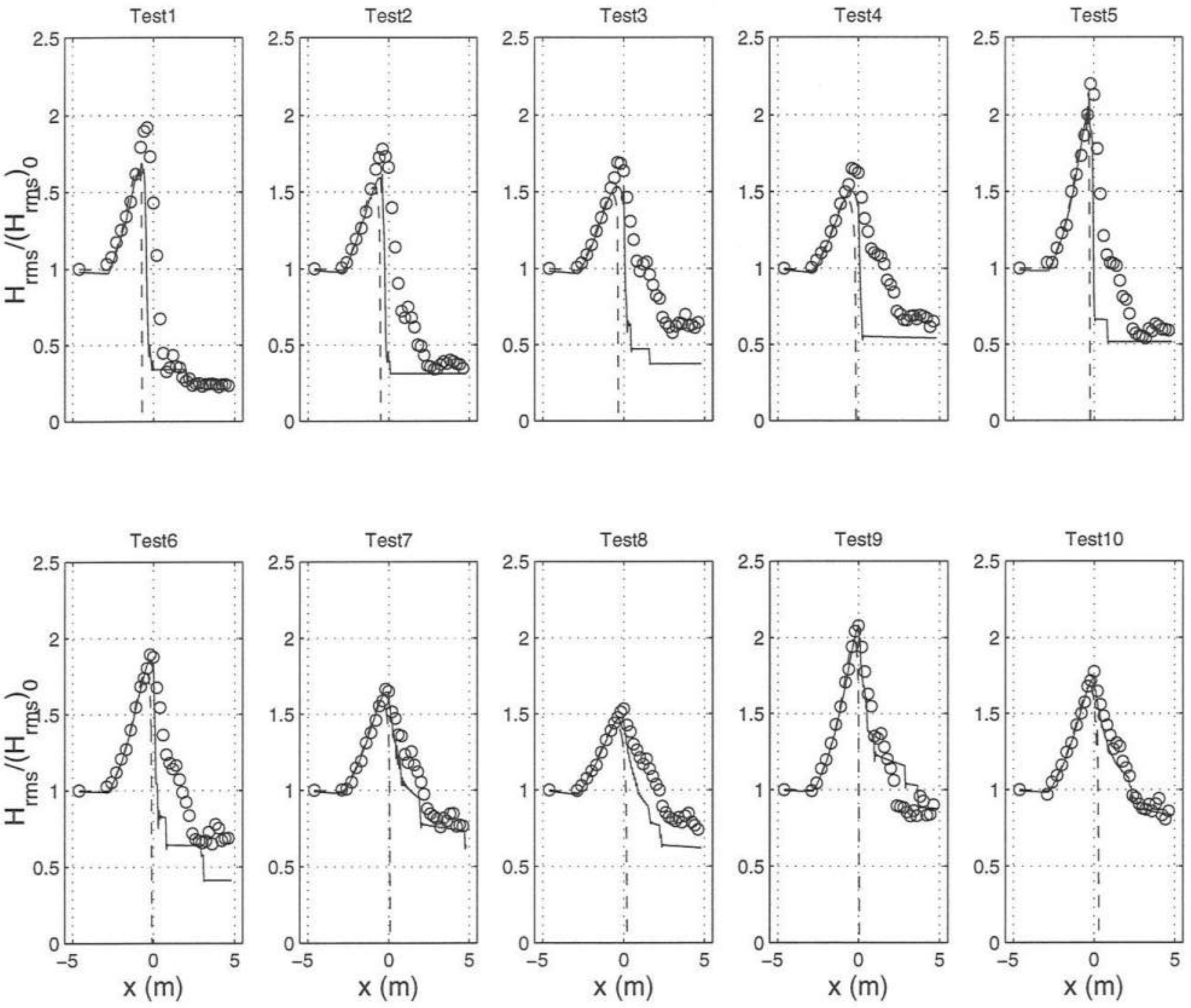

Figure 6.8: Normalized H_{rms} for random wave tests $1-10$ ('solid line' spectral model; 'dashed line' bulk model; 'o' data).

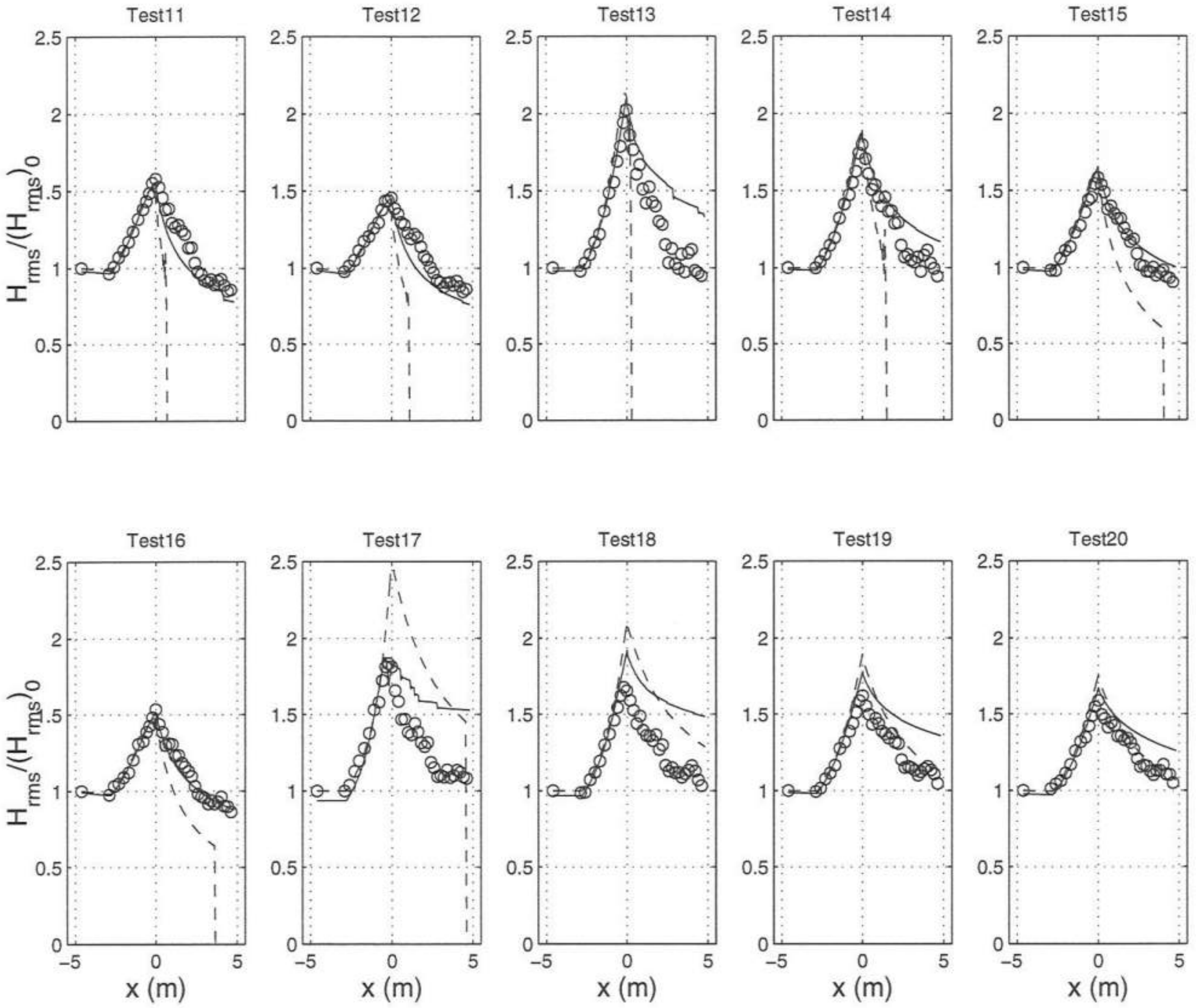

Figure 6.9: Normalized H_{rms} for random wave tests $11-20$ ('solid line' spectral model; 'dashed line' bulk model; '○' data).

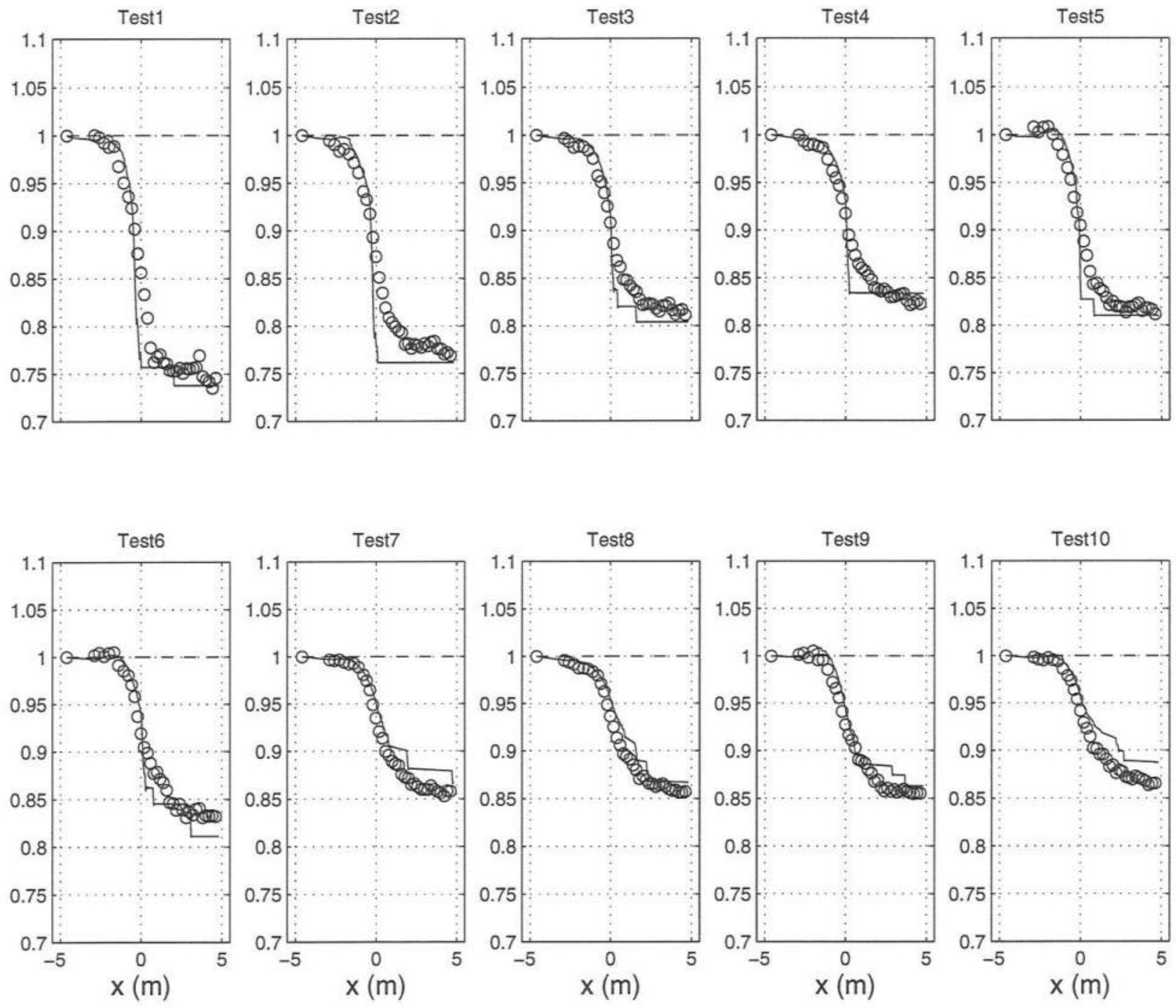

Figure 6.10: Normalized $\bar{\omega}$ for random wave tests $1-10$ ('solid line' spectral model; 'dashed line' bulk model; '$\circ$' data).

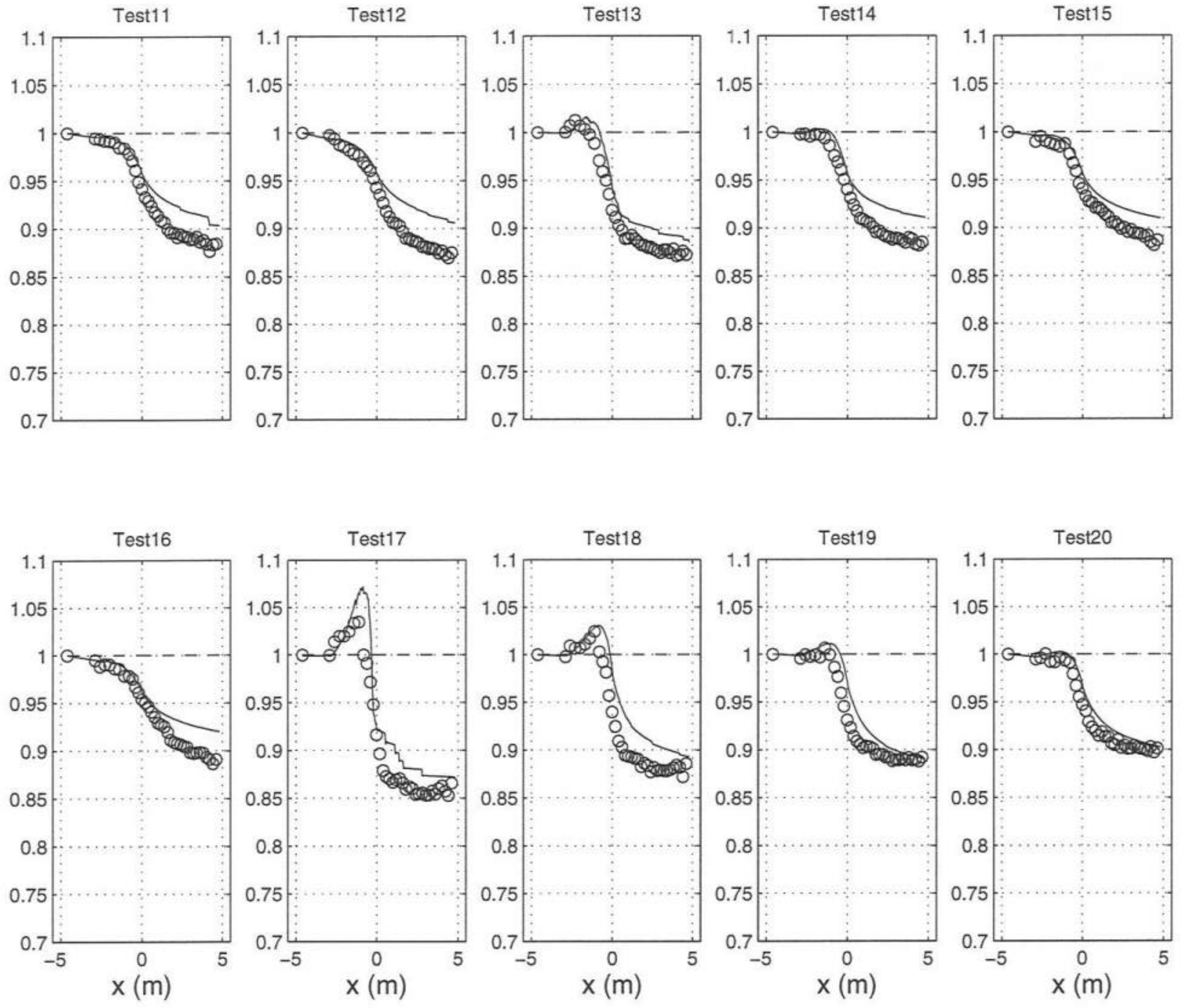

Figure 6.11: Normalized $\bar{\omega}$ for random wave tests $11-20$ ('solid line' spectral model; 'dashed line' bulk model; 'o' data).

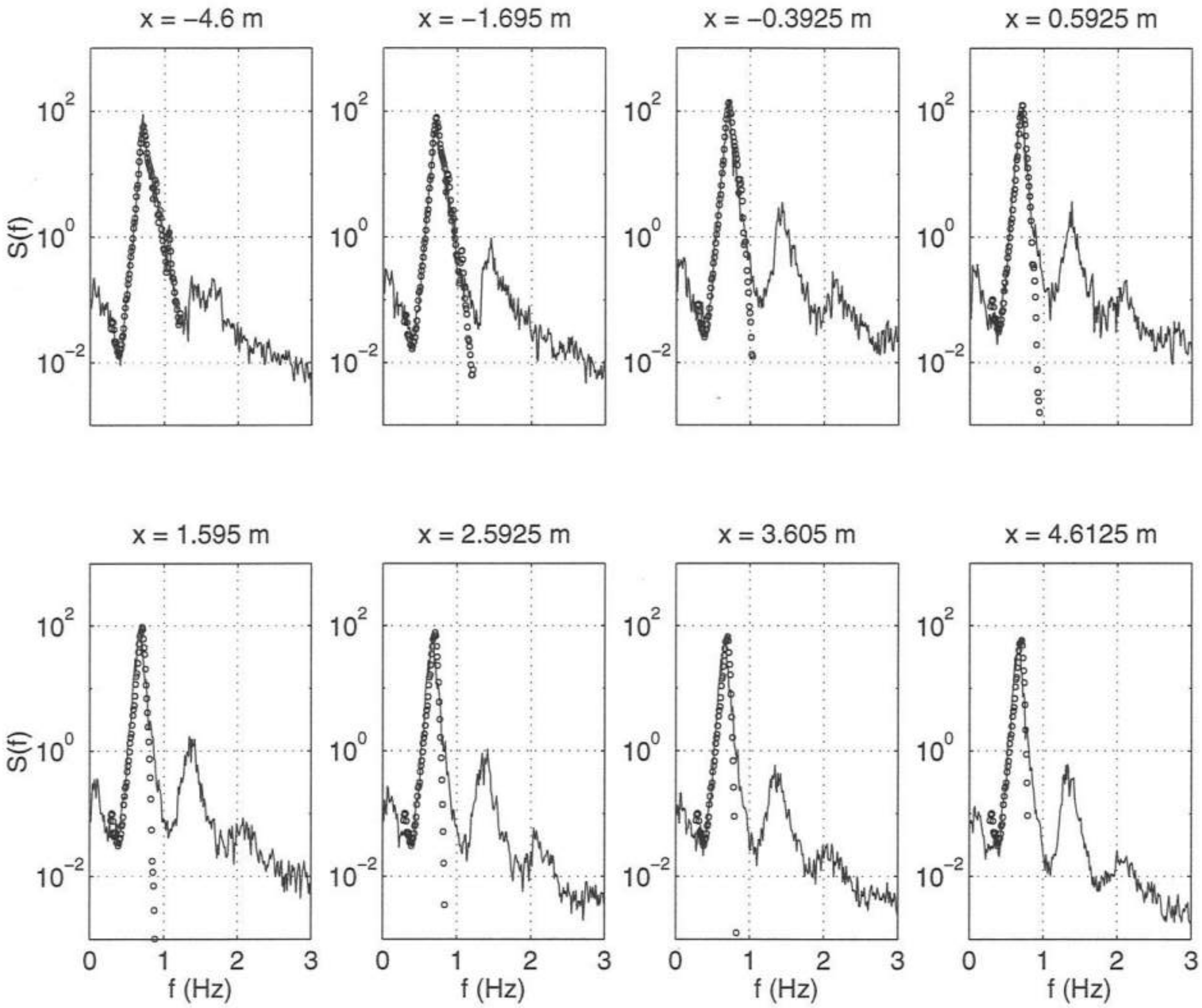

Figure 6.12: Energy spectra for Test 16 ('∘' spectral model; 'solid line' data).

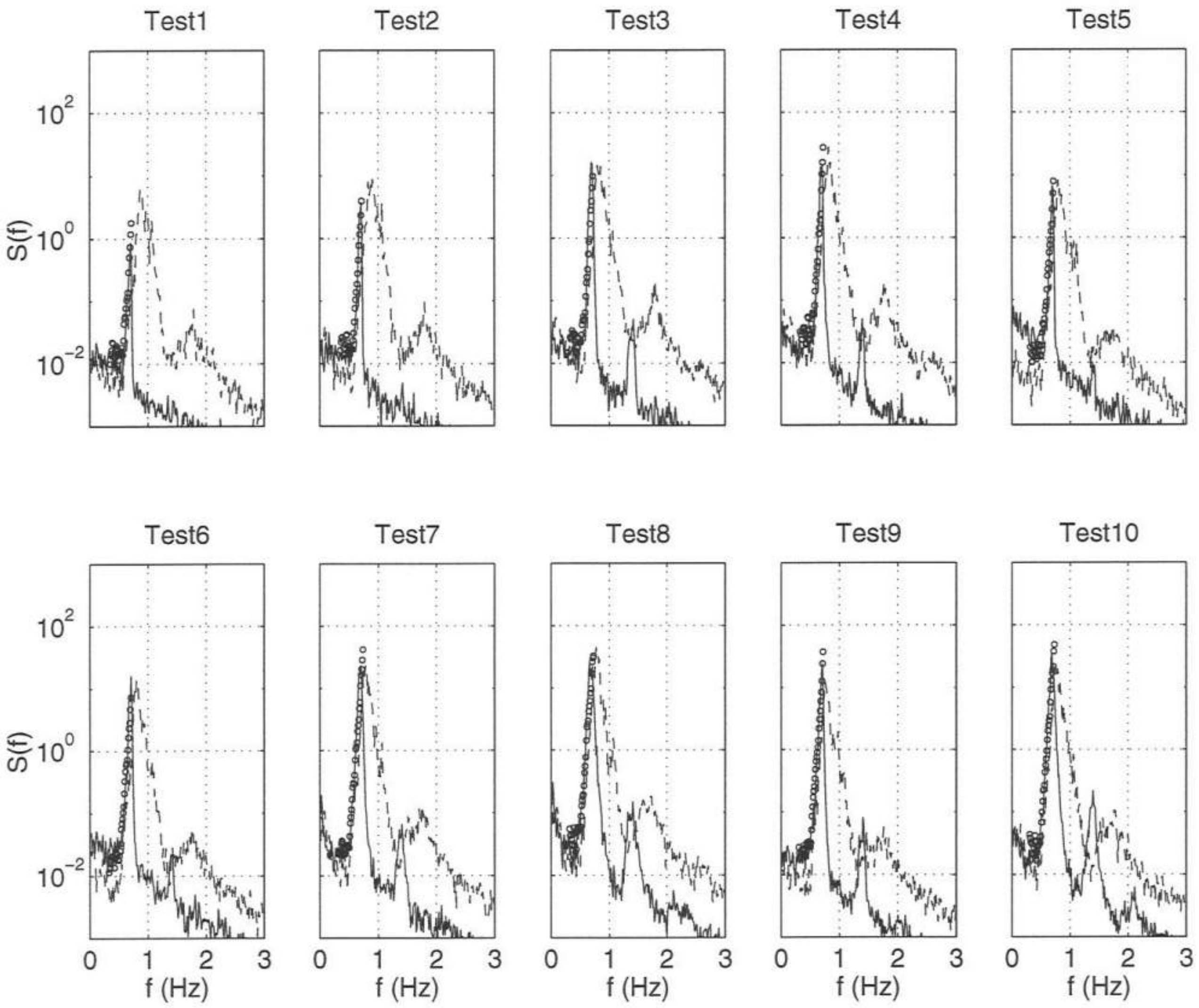

Figure 6.13: Energy spectra comparisons for Tests $1-10$ ('dashed line' data at $x = -4.6$ m; 'solid line' data at $x = 4.6$ m; '∘' spectral model at at $x = 4.6$ m).

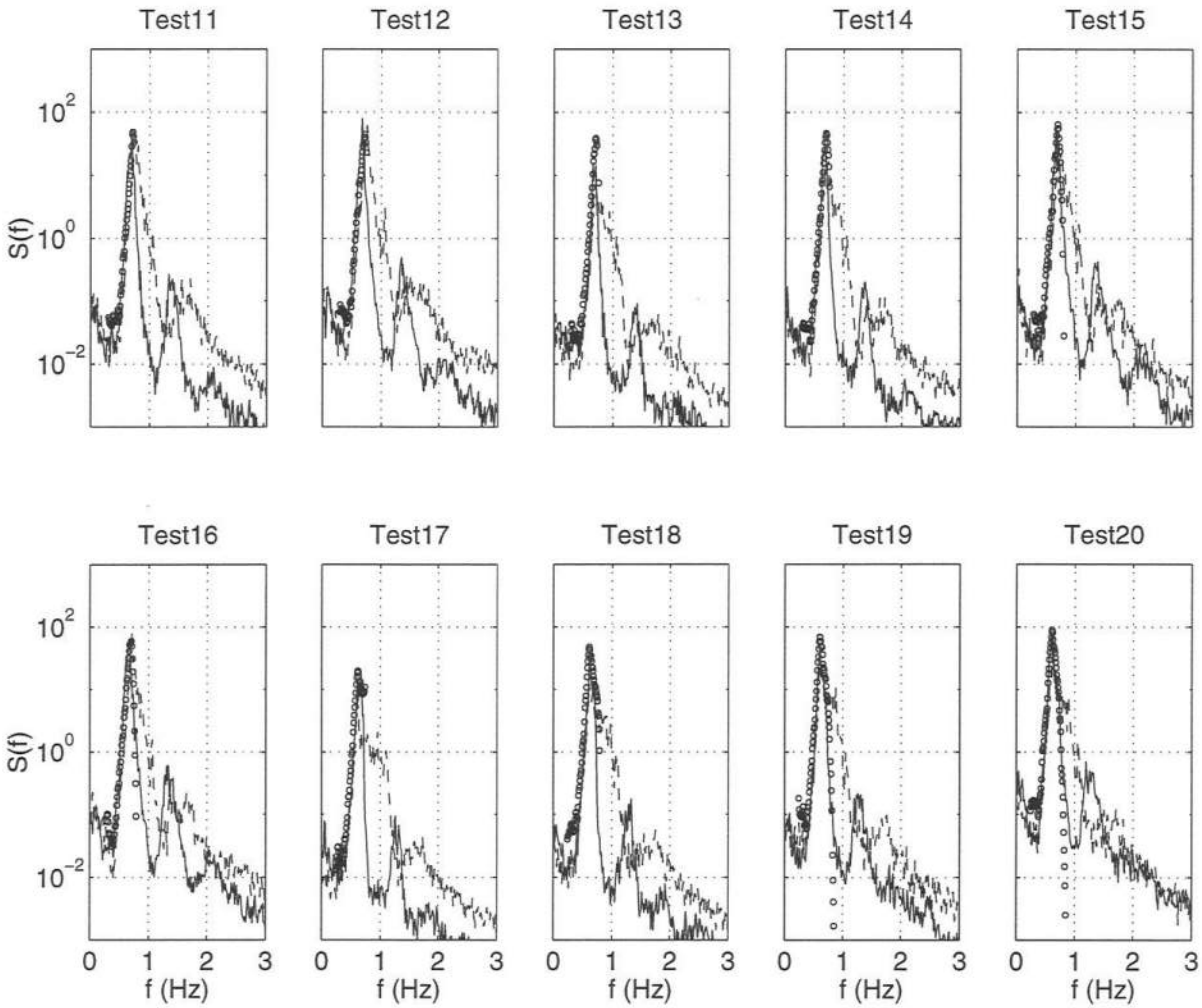

Figure 6.14: Energy spectra comparisons for Tests 11 – 20 ('dashed line' data at $x = -4.6$ m; 'solid line' data at $x = 4.6$ m; 'o' spectral model at at $x = 4.6$ m).

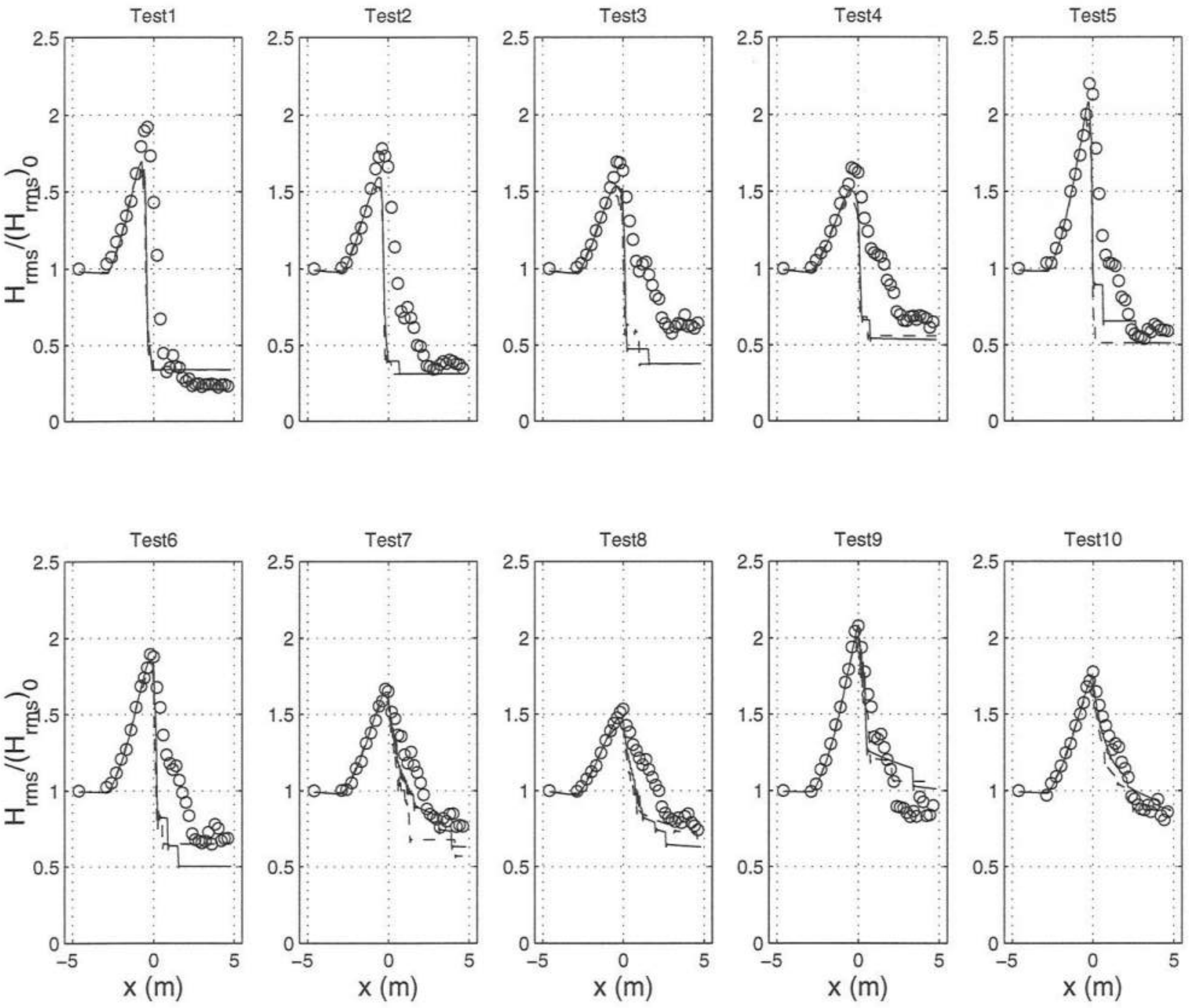

Figure 6.15: Normalized H_{rms} for random wave tests $1-10$ ('solid line' present dissipation model; 'dashed line' Battjes and Janssen dissipation model; 'o' data).

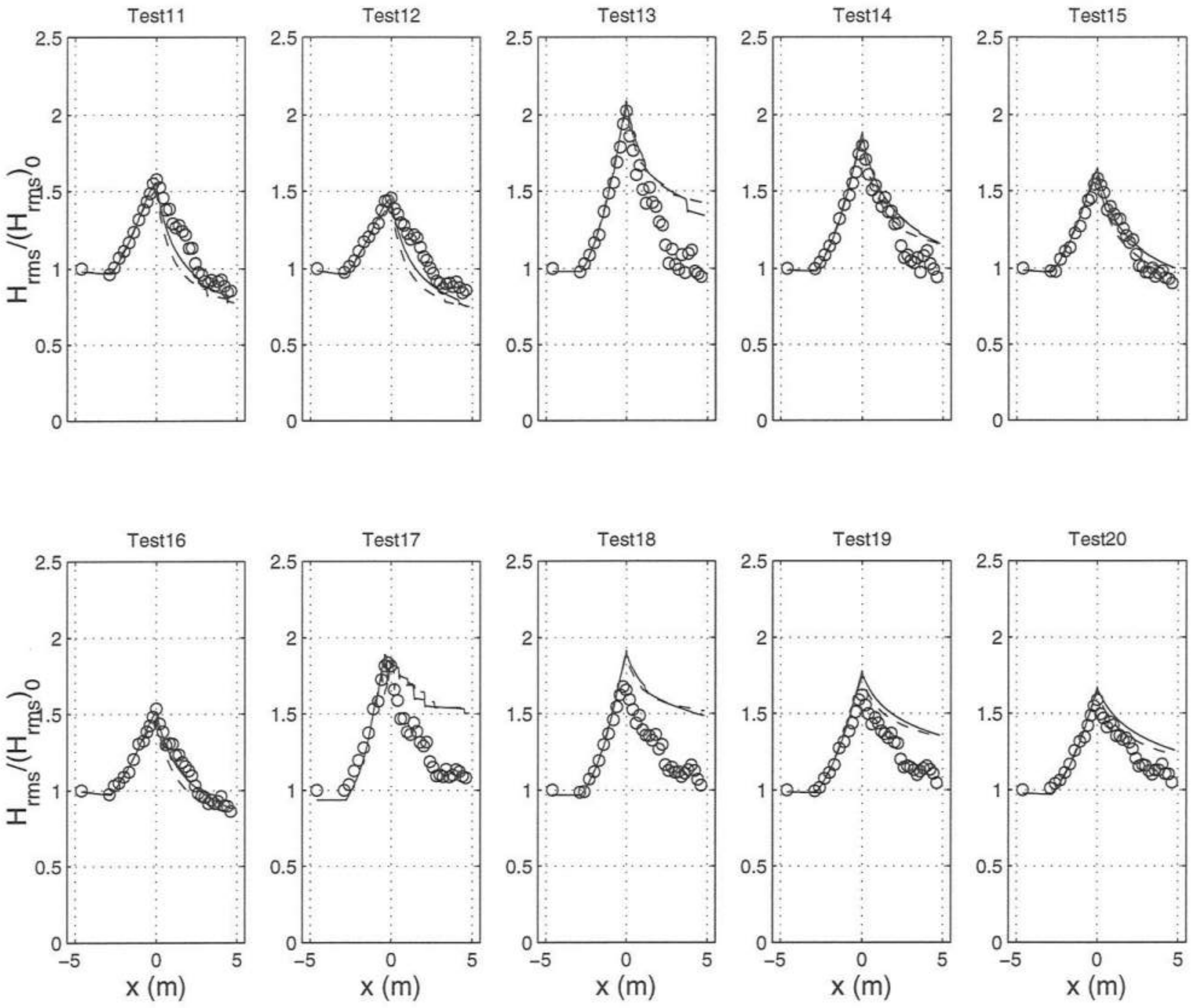

Figure 6.16: Normalized H_{rms} for random wave tests 11 − 20 ('solid line' present dissipation model; 'dashed line' Battjes and Janssen dissipation model; '○' data).

the probability of breaking reduces in the narrow part of the channel, leading to a reduction in the energy dissipation. The monochromatic model on the other hand has been designed for a monotonically increasing current, and does not account for waves not continuing to break. Shallow water breaking models of Thornton and Guza (1983) and Battjes and Janssen (1978) have been calibrated on monotonic beaches.

Chapter 7

CONCLUSIONS

A detailed study has been conducted on the dynamics of wave blocking and current limited wave breaking under different wave conditions with the help of experiments and numerical modeling. The aim has been to quantify the physical processes involved and attempt to reproduce the experimental results with the help of a numerical model.

An existing 30 m long flume was modified to conduct experimental studies on wave blocking. A recirculating system was built in the flume so that currents could be generated by drawing out the water from behind the wavemaker and putting it back into the flume at the far end. The wavemaker consisted of a piston-type flat paddle, and the solid plate was replaced by a perforated plate so as to allow the currents to go through but still be able to generate waves. The experimental setup could only generate currents opposing the waves. An inlet was created in the middle of the flume by narrowing the flume width with the help of false walls. The maximum currents were generated in the inlet and the experiments were designed such that wave blocking occurred inside the inlet. The inlet was designed such that there is no flow separation and jet like formations in the flow field as the current left the inlet. Velocity measurements of the current were made using SONTEK ADV probes, while the water surface was measured with the help of capacitance wave gages.

The experimental studies on monochromatic waves were divided into the small amplitude wave tests and the large amplitude wave tests. In the small amplitude wave tests the initial wave steepness was kept small enough so that waves did not break even at the blocking point causing them to get reflected. A detailed measurement of the wave envelope was made for different conditions. For the smallest wave heights the measured envelope through the blocking region was an Airy function and confirmed the linear theory predictions. With increasing amplitude, the envelope deviated from the Airy function theory, and there was a transition region between the waves being completely reflected with no breaking to completely breaking with no reflection. Partial wave blocking was also observed. The large amplitude tests were conducted to study the effects of non-linearity on wave blocking and to develop an empirical function for energy dissipation due to wave breaking. A simple wave action conservation model was used to compare with data. The energy decay was found to be simulated reasonably well with a modified bore model that asymptotes to the form of the depth limited breaking model in shallow water. The parameter quantifying energy decay was found to have a much smaller value than that used for depth-limited breaking. Due to the significant increase in wave steepness prior to blocking, amplitude dispersion became important and a third order Stokes dispersion relation did a much better job than the linear dispersion relation in predicting the blocking point. In some of the largest amplitude tests waves were not blocked due to side band instabilities. The growth of side bands were enhanced considerably due to both the increased wave steepness and the longer temporal scales at which the energy propagated. The upper side band and the primary wave component were then blocked and the lower side band propagated through because its blocking point was never reached. Numerical models that are unable to simulate this complex phenomenon will yield highly erroneous results.

A series of narrow-banded spectral tests were conducted. The modulating wave trains created a moving blocking point and the aim was to see if this could act as a forcing mechanism for the generation of long waves analogous to the moving breaking point in shallow water. Experiments were conducted both on bichromatic wave groups and wave packets, but no long waves were observed. In the wave group tests the individual wave components were blocked at their respective blocking points with little or no interaction. Reflection of the wave packet from the blocking point was also observed.

A weakly non-linear numerical model was developed for narrow-banded wave spectra propagating in a varying channel. The model simulated wave blocking by accounting for complex values in the phase function beyond the blocking point. Under no blocking conditions and in regions of constant width our model can be reduced to the envelope model of Turpin *et al.* (1983). The model is unstable in regions where the channel width and/or depth is changing rapidly and a 3 point filter had to be used to suppress these instabilities. Though we have developed a global model which simulates wave blocking without having to use any asymptotic expansions, the model still has two major limitations. Firstly, it uses the linear dispersion relation to determine the blocking point which we have already seen from our experiments, does a rather poor job in predicting the blocking point. And secondly, the model blocks the waves at the carrier frequency of the modulating wave train. Our observations both in the blocking of monochromatic wave trains with side bands and in the blocking of wave groups show that in reality narrow-banded spectral waves are not blocked at their carrier frequency, but, instead the individual components of the spectrum are blocked at their respective blocking points. To counteract this limitation, a spectral numerical model would have to be developed along the lines of the non-linear integro-differential model of Zakharov (1968), which treats the dynamics of each frequency component separately.

To complement the experimental studies on current-limited wave breaking in monochromatic waves, a series of experiments was also conducted on random waves. The aim was to develop an empirical bulk dissipation formula for current-limited wave breaking similar to the one developed by Thornton and Guza (1983) for depth-limited wave breaking. An empirical formula based on the modified bore dissipation formula for monochromatic waves and an empirical probabilistic distribution of breaking waves was developed and calibrated with the data. The formula was tested using both a bulk wave action model and a spectral model. Since the spectral model resolved the details of the spectrum it compared much better with the data.

A puzzling feature of the bulk dissipation formula is that the parametric coefficients have different values for random and monochromatic waves. This is unlike the dissipation formulae for depth limited breaking. A probable reason for the disparity could be that our experiments were conducted in a current which is not monotonically increasing (the current reaches a maximum in the narrow channel), while the experiments on depth-limited breaking were conducted on monotonic beaches. The dissipation formula for random waves can account for the current not being monotonic because the probability of breaking reduces when the current stops increasing. The dissipation formula for monochromatic waves on the other hand, assumes a monotonic current and continues to dissipate energy even when the current becomes constant.

The advantage of using the bulk dissipation formula is that in the shallow water limit it asymptotes to the depth-limited breaking formula of Thornton and Guza (1983). It should be kept in mind that though both the depth-limited and the current-limited formulae have very similar forms the parametric values identifying the energy decay in the two processes are very different. A detailed experimental study in different conditions are required to obtain a range of parametric values spanning both the current dominated and depth dominated wave breaking.

Bibliography

Badulin, S. I., Pokazeyev, K. V., and Rosenberg, A. D. (1983). A laboratory study of the transformation of regular gravity-capillary waves in inhomogenous flows. *Izv. Atmos. Ocean. Phys.*, **19**, 782–787.

Battjes, J. A. and Janssen, J. P. F. M. (1978). Energy loss and set-up due to breaking of random waves. In *Proc.* 16th *Int. Conf. Coastal Engineering*, 569−587, Hamburg. ASCE.

Benjamin, T. B. and Feir, J. E. (1967). The disintegration of water waves on deep water part 1. theory. *J. Fluid Mech.*, **27**, 417–430.

Bowden, K. F. (1948). Some observations of waves and other fluctuations in a tidal current. *Proc. Roy. Soc. London*, **192**, 403–425.

Bretherton, F. P. and Garrett, C. J. R. (1969). Wavetrains in inhomogenous moving media. *Proc. Roy. Soc. London A.*, **302**, 529–554.

Chawla, A. and Kirby, J. T. (1998). Experimental study of wave breaking and blocking on opposing currents. In *Proc.* 26th *Int. Conf. Coastal Engineering*, 759−772, Copenhagen. ASCE.

Chawla, A. and Kirby, J. T. (1999a). Waves on opposing currents: Data report. Technical Report CACR-99-03, Center for Applied Coastal Research, University of Delaware.

Chawla, A. and Kirby, J. T. (1999b). Current limited wave breaking at or before the blocking point in monochromatic and random waves. Submitted to *J. Geophys. Res.*

Chawla, A. and Kirby, J. T. (1999c). A perforated wavemaker theory. manuscript in preparation.

Chen, Q., Madsen, P. A., Schäffer, H. A., and Basco, D. R. (1998). Wave-current interaction based on an enhanced Boussinesq approach. *Coastal Eng.*, **33**, 11–39.

Chu, V. H. and Mei, C. C. (1970). On slowly varying Stokes waves. *J. Fluid Mech.*, **41**, 873–887.

Chu, V. H. and Mei, C. C. (1971). The non-linear evolution of Stokes waves in deep water. *J. Fluid Mech.*, **47**, 337–351.

Davey, A. (1972). The propagation of a weak non-linear wave. *J. Fluid Mech.*, **53**, 769–781.

Evans, J. T. (1955). Pneumatic and similar breakwaters. *Proc. Roy. Soc.*, **231 (A)**, 457–466.

Gardner, C. S., Greene, J. M., Kruskal, M. D., and Miura, R. M. (1967). Method for solving the Korteweg-de Vries equation. *Phy. Rev. Lett.*, **19**, 1095–1097.

Gerber, M. (1987). The Benjamin-Feir instability of a deep water Stokes wave packet in the presence of a non-uniform medium. *J. Fluid Mech.*, **176**, 311–332.

Hasimoto, H. and Ono, H. (1972). Non-linear modulation of gravity waves. *J. Phys. Soc. Jpn.*, **33**, 805–811.

Hasselmann, K. (1974). On the spectral dissipation of ocean waves due to white-capping. *Boundary-Layer Meteorology*, **6**, 107–127.

Hedges, T. S., Anastasiou, K., and Gabriel, D. (1985). Interaction of random waves and currents. *J. Waterways, Port, Coast. and Ocean Engng.*, **111**, 275–288.

Huang, N. E., Chen, D. T., Tung, C. C., and Smith, J. R. (1972). Interactions between steady non-uniform currents and gravity waves with application for current measurements. *J. Phys. Oceanography*, **2**, 420–431.

Jonsson, I. G. (1990). Wave-current interactions. In *The Sea*, volume 9, pages 65–120. Wiley Interscience, New York.

Jonsson, I. G., Skougaard, C., and Wang, J. D. (1970). Interaction between waves and currents. In *Proc.*12th *Int. Conf. Coastal Engineering*, 489−508.

Lai, R. J., Long, S. R., and Huang, N. E. (1989). Laboratory studies of wave-current interaction:kinematics of the strong interaction. *J. Geophys. Res.*, **94**, 16201–16214.

Lake, B. M., Yuen, H. C., Rungaldier, H., and Ferguson, W. E. J. (1977). Non-linear deep water waves: Theory and experiment. part 2: Evolution of a continous wave train. *J. Fluid Mech.*, **83**, 49–74.

LeMéhauté, B. (1962). On non-saturated breakers and the wave run-up. In *Proc.*8th *Int. Conf. Coastal Engineering*, 77−92, Mexico. ASCE.

Lo, E. and Mei, C. C. (1985). A numerical study of water-wave modulation based on a higher-order non-linear Schrödinger equation. *J. Fluid Mech.*, **150**, 395–416.

Longuet-Higgins, M. S. and Fox, M. H. (1977). Theory of the almost-highest wave: The inner solution. *J. Fluid Mech.*, **80**, 721–741.

Longuet-Higgins, M. S. and Smith, N. D. (1983). Measurement of breaking waves by a surface jump meter. *J. Geophys. Res.*, **88**, 9823–9831.

Longuet-Higgins, M. S. and Stewart, R. W. (1960). Changes in the form of short gravity waves on long waves and tidal currents. *J. Fluid Mech.*, **8**, 565–583.

Longuet-Higgins, M. S. and Stewart, R. W. (1961). The change in the amplitude of short gravity waves on steady non-uniform currents. *J. Fluid Mech.*, **10**, 529–549.

Ludwig, D. (1966). Uniform asymptotic expansions at a caustic. *Comm. Pure App. Math.*, **19**, 215–250.

Mallory, J. K. (1974). Abnormal waves on the south east coast of south africa. *Int. Hydrogr. Rev.*, **51**, 99–129.

Melville, W. K. (1983). Wave modulation and breakdown. *J. Fluid Mech.*, **128**, 489–506.

Peregrine, D. H. (1976). Interaction of water waves and currents. *Advances in Applied Mechanics*, **16**, 9–117.

Phillips, O. M. (1966). *The dynamics of the upper ocean.* Cambridge Univ. Press, London and New York.

Phillips, O. M. (1977). *The dynamics of the upper ocean.* Cambridge University Press, Cambridge, England, second edition.

Ris, R. C. and Holthuijsen, L. H. (1996). Spectral modelling of current induced wave-blocking. In *Proc.*25th *Int. Conf. Coastal Engineering*, 1246–1254, Orlando. ASCE.

Sakai, S. and Saeki, H. (1984). Effects of opposing current on wave transformation. In *Proc.*19th *Int. Conf. Coastal Engineering*, 1132–1148,Houston. ASCE.

Sakai, S., Hiyamizu, K., and Saeki, H. (1986). Irregular wave transformation affected by opposing currents. In *Proc.*20^{th} *Int. Conf. Coastal Engineering*, 697−710,Taipei. ASCE.

Shapiro, R. (1970). Smoothing, filtering and boundary effects. *Rev. Geophys. and Space Phys.*, **8**, 359–387.

Shyu, J. H. and Phillips, O. M. (1990). The blockage of gravity and capillary waves by longer waves and currents. *J. Fluid Mech.*, **217**, 115–141.

Smith, R. (1975). Reflection of short gravity waves on a non-uniform current. *Math. Proc. Camb. Phil. Soc.*, **78**, 517–525.

Stiassnie, M. and Dagan, G. (1979). Partial reflexion of water waves by non-uniform adverse currents. *J. Fluid Mech.*, **92**, 119–129.

Tayfun, M. A., Dalrymple, R. A., and Yang, C. Y. (1976). Random wave-current interactions in water of varying depth. *Ocean Engng.*, **3**, 403–420.

Thomas, G. P. and Klopman, G. (1997). Wave-current interactions in the nearshore region. In J. N. Hunt, editor, *Gravity waves in water of finite depth*. 255−319. Computational Mechanics Publications, Boston.

Thornton, E. B. and Guza, R. T. (1983). Transformation of wave height distribution. *J. Geophys. Res.*, **88**, 5925–5938.

Trulsen, K. and Dsythe, K. B. (1990). Frequency down-shift through self modulation and breaking. In A. Törum and O. T. Gudmestad, editors, *Water wave kinematics*, pages 561–572. Kluwer Academic Publishers.

Trulsen, K. and Mei, C. C. (1993). Double reflection of capillary/gravity waves by a non-uniform current: a boundary-layer theory. *J. Fluid Mech.*, **251**, 239–271.

Turpin, F. M., Benmoussa, C., and Mei, C. C. (1983). Effects of slowly varying depth and current on the evolution of a Stokes wavepacket. *J. Fluid Mech.*, **132**, 1–23.

Whitham, G. B. (1965). A general approach to linear and non-linear dispersive waves using a Lagrangian. *J. Fluid Mech.*, **22**, 273–283.

Xu, D., Hwang, P. A., and Wu, J. (1986). Breaking of wind-generated waves. *J. Phys. Ocean.*, **16**, 2172–2178.

Yuen, H. C. and Ferguson, W. E. J. (1978). Relationship between Benjamin-Feir instability and recurrence in the non-linear Schrödinger equation. *Phys. Fluids*, **21**, 1275–1278.

Yuen, H. C. and Lake, B. M. (1975). Nonlinear deep water waves: Theory and experiment. *Physics of Fluids*, **18**, 956–960.

Yuen, H. C. and Lake, B. M. (1980). Instabilities of waves on deep water. *Ann. Rev. Fluid Mech.*, **12**, 303–334.

Zakharov, V. E. (1968). Stability of periodic waves of finite amplitude on the surface of a deep fluid. *J. Applied Mech. Phys.*, **9**, 190–194.

Zakharov, V. E. and Shabat, A. B. (1972). Exact theory of two-dimensional self-focusing and one-dimensional self-modulating waves in non-linear media. *Sov. Phys. – JETP*, **34**, 62–69.